ABSTRACT

ABDO, MOHAMMAD GAMAL MOHAMMAD MOSTAFA. Multi-Level Reduced Order Modeling Equipped with Probabilistic Error Bounds. (Under the direction of Hany S. Abdel-Khalik, Dmitriy Y. Anistratov, Ilse C. F. Ipsen and Ralph C. Smith).

Over the past few decades, engineering analysts have increased their reliance on high fidelity modeling to better emulate, i.e., simulate, the behavior of complex engineering systems, such as nuclear reactors. While this approach has a tremendous benefit in terms of developing a better understanding of system behavior under the broad range of conditions expected during normal and off-normal conditions, it comes at a significant computational cost that may not be feasible for day-to-day engineering calculations. This follows because high fidelity simulation is typically based on extremely detailed models with tightly coupled physics which require substantial computing resources as compared to phenomenological models that are more suited for routine engineering analyses. In order to reap the benefits of high fidelity simulation, significant improvements in the computational efficiency are warranted to allow execution of computationally taxing engineering analyses such as uncertainty quantification, sensitivity analysis, and design optimization.

This thesis develops robust reduced order modeling (ROM) techniques to achieve the needed efficiency to render feasible the use of high fidelity tools for routine engineering analyses. Markedly different from the state-of-the-art ROM techniques, our work focuses only on techniques which can quantify the credibility of the reduction which can be measured with the reduction errors upper-bounded for the envisaged range of ROM model application. Our objective is two-fold. First, further developments of ROM techniques are proposed when conventional ROM techniques are too taxing to be computationally practical. This is achieved via a multi-level ROM methodology designed to take advantage of the multi-scale modeling

www.manaraa.com

strategy typically employed for computationally taxing models such as those associated with the modeling of nuclear reactor behavior. Second, the discrepancies between the original model and ROM model predictions over the full range of model application conditions are upper-bounded in a probabilistic sense with high probability.

ROM techniques may be classified into two broad categories: surrogate construction techniques and dimensionality reduction techniques, with the latter being the primary focus of this work. We focus on dimensionality reduction, because it offers a rigorous approach by which reduction errors can be quantified via upper-bounds that are met in a probabilistic sense. Surrogate techniques typically rely on fitting a parametric model form to the original model at a number of training points, with the residual of the fit taken as a measure of the prediction accuracy of the surrogate. This approach, however, does not generally guarantee that the surrogate model predictions at points not included in the training process will be bound by the error estimated from the fitting residual.

Dimensionality reduction techniques however employ a different philosophy to render the reduction, wherein randomized snapshots of the model variables, such as the model parameters, responses, or state variables, are projected onto lower dimensional subspaces, referred to as the “active subspaces”, which are selected to capture a user-defined portion of the snapshots variations. Once determined, the ROM model application involves constraining the variables to the active subspaces. In doing so, the contribution from the variables discarded components can be estimated using a fundamental theorem from random matrix theory which has its roots in Dixon’s theory, developed in 1983. This theory was initially presented for linear matrix operators. The thesis extends this theorem’s results to allow reduction of general smooth nonlinear operators. The result is an approach by which the adequacy of a given active subspace

www.manaraa.com

determined using a given set of snapshots, generated either using the full high fidelity model, or other models with lower fidelity, can be assessed, which provides insight to the analyst on the type of snapshots required to reach a reduction that can satisfy user-defined preset tolerance limits on the reduction errors.

Reactor physics calculations are employed as a test bed for the proposed developments. The focus will be on reducing the effective dimensionality of the various data streams such as the cross-section data and the neutron flux. The developed methods will be applied to representative assembly level calculations, where the size of the cross-section and flux spaces are typically large, as required by downstream core calculations, in order to capture the broad range of conditions expected during reactor operation.

www.manaraa.com

© Copyright 2016 by Mohammad Gamal Mohammad Mostafa Abdo

All Rights Reserved

www.manaraa.com

Multi-Level Reduced Order Modeling Equipped with Probabilistic Error Bounds

by
Mohammad Gamal Mohammad Mostafa Abdo

A dissertation submitted to the Graduate Faculty of
North Carolina State University
in partial fulfillment of the
requirements for the degree of
Doctor of Philosophy

Nuclear Engineering

Raleigh, North Carolina

2016

APPROVED BY:

Dr. Hany S. Abdel-Khalik Committee Co-Chair	Dr. Dmitriy Y. Anistratov Committee Co-Chair
Dr. Ilse C. F. Ipsen Committee Member	Dr. Ralph C. Smith Committee Member

www.manaraa.com

DEDICATION

"Read in the Name of your Lord Who created;

Created man, out of a clot;

Read, and your Lord is the Most Generous;

Who taught by the Pen;

Taught man that which he knew not."

(*Holly Quraan, Chapter 96, Verses 1-5.*)

This work is dedicated to my devoted mother Aleya, inspiring father Gamal, precious sister Shaimaa, lovely wife Haydaa and adorable sons: Ewan and Rayan. Throughout my journey they never stopped believing in me, supporting me, and lightening my road.

المنارة للاستشارات
www.manaraa.com

BIOGRAPHY

Mohammad Abdo was born in Alexandria, Egypt on May 8th, 1977 to Gamal M. Abdo (a lawyer) and Aleya M. Abderabbo (a homemaker). He has a younger sister Shaimaa G. Abdo. He was married to Haydaa Zayed A. Selmy (a school teacher) on July 9th, 2003. He was blessed with his first son Ewan M. G. Abdo on December 5th, 2004 and his second son Rayan M. G. Abdo on August 5th, 2010.

Mohammad received his Bachelor of Science from the Department of Mechanical Engineering at Alexandria University on July 2000. He spent more than ten years working in the Mechanical Engineering field of infrastructural designs such as HVAC, Plumbing, Fire Fighting and Oil Networks under the supervision of Dr. Medhat A. Shawky, Former Faculty of Engineering Dean at Pharos University in Alexandria. He worked as a part-time Teaching Assistant/ Demonstrator in Alexandria University as well as a full-time at Pharos University. In the summer of 2011, Mohammad joined the Ph.D. graduate program at the Nuclear Engineering Department of NC State University to work as a research assistant/teaching assistant under the supervision of Prof. Hany S. Abdel-Khalik.

www.manaraa.com

ACKNOWLEDGMENTS

Words cannot express the level of gratitude and appreciation I have for my advisor Dr. Hany S. Abdel-Khalik for his consistent support, patience, guidance and valuable scientific perspectives throughout my graduate studies. I am grateful for my committee members: Dr. Anistratov, Dr. Ipsen and Dr. Smith for their valuable, insightful comments and discussions. My gratitude goes next to Dr. Ivanov, Dr. Bourham, and Dr. Azmy who have provided continuous support to me as well as other graduate students to pursue our degrees. Thanks also go to the entire administrative staff who worked behind the scenes to make this work see the light. I would also love to express my sincere gratitude to a long list of wonderful people that enriched my life starting with my loving parents for their unconditional and limitless love and support; their inexorable efforts to provide me with all essences of happiness along with my adorable sister and her unconditional altruism and care. I cannot thank enough my beloved wife and children who have endured every hardship along the path of my graduate studies. As for my professional life, I have fortunately crossed paths with great people who literally changed my life with their limitless wisdom such as my professors: Dr. Medhat Shawky, the former dean of the faculty of Engineering at PUA, Dr. Taher Awad and Dr. Alaa Hamdy the heads of the mechanical department, Dr. Magued N. Abdelmalek and Ahmed Abdel Mutaal the heads of the department of basic science, Dr. Saad el-Safy, Dr. Ihab G. Adam and Dr. Mohammad Abdelrahman my professors that I assisted teaching various courses which significantly enriched my knowledge, and my friend and collegue engineer Sherif Omar, as they all supported me and spared no effort to encourage me to pursue my Ph.D. studies.

www.manaraa.com

TABLE OF CONTENTS

www.manaraa.com

www.manaraa.com

www.manaraa.com

www.manaraa.com

LIST OF TABLES

www.manaraa.com

LIST OF FIGURES

www.manaraa.com

www.manaraa.com

www.manaraa.com

www.manaraa.com

www.manaraa.com

CHAPTER 1

INTRODUCTION

To understand the behavior of real-world complex systems, one must be able to model in detail the various phenomena affecting the system's macroscopic behavior. For systems that are sufficiently complex like nuclear reactors, the associated models can be extremely expensive which may render their use computationally impractical for routine engineering calculations. To overcome this challenge, some level of reduction is typically required to allow repeated execution for routine engineering calculations and engineering-oriented studies such as design optimization, sensitivity analysis, and uncertainty quantification. The computational framework employed to introduce the reduction is typically referred to as reduced order modeling (ROM). ROM entails any process by which the complexity of the calculations can be reduced. The complexity can be measured in terms of the computational cost required to execute the model, the dimensionality of the state variables, and the input and output data interfaces.

1.1 Overview

In the next few subsections, we provide a short overview of different ROM methods. Our goal is to highlight the salient features of each method and its associated challenges. This is to motivate the two primary objectives of this thesis, outlined below and will be referenced later in the discussion.

- Development of accurate and realistic error bounds on the reduced models to allow for reliable extrapolation to the entire range of the validity of the original model, i.e., prior to its reduction.

www.manaraa.com

- Further development of existing ROM methods to allow for a more efficient rendition of the reduced model when the original model is too expensive to execute as required by existing ROM methods.

1.2 Literature Review

ROM methods may be classified into two categories: Surrogate Construction methods (SC) (also referred as function approximation) and Dimensionality Reduction methods (DR), as highlighted in Fig. 1-1.

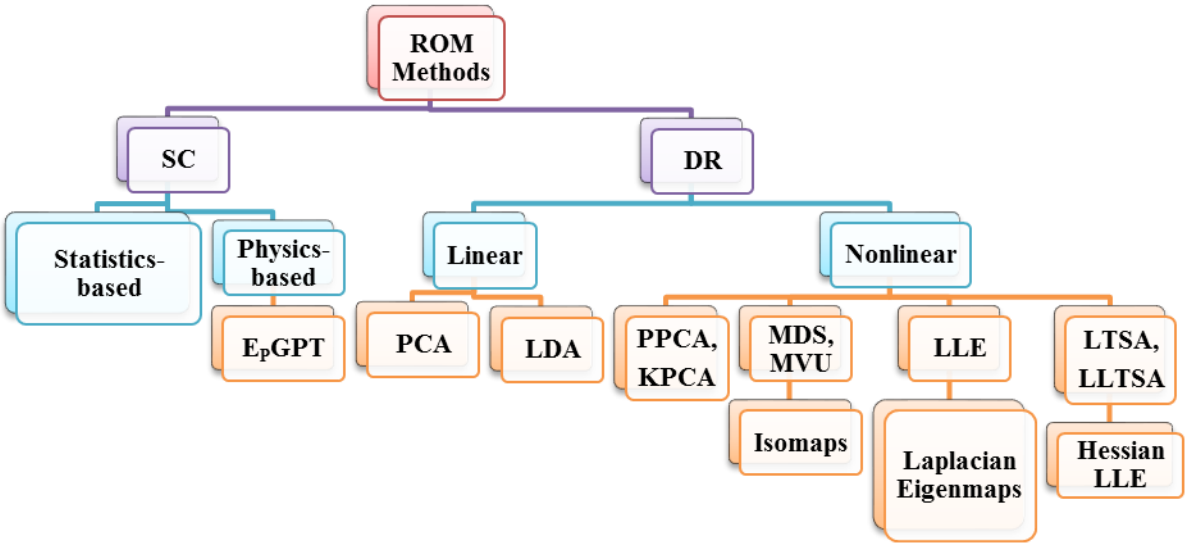

Fig. 1-1. ROM Methods

To help motivate the pros and cons of ROM methods, we employ a generic model to describe the original model for which a reduction is sought. Consider a model with y responses, and *x* input parameters, where *f* is a general smooth nonlinear function, i.e., $y = f(x)$.

www.manaraa.com

1.2.1 Surrogate Model Construction (SC)

Surrogate construction (SC) or function approximation methods aim to use an approximate representation $\tilde{f}$ (also known as *meta-model*) as a substitute for the original function f to approximate the relationship between the input data (parameters) and the responses of interest via analytic functions with undetermined coefficients or features. This can be mathematically described as:

$$f(x) \approx \tilde{f}\left(\mathcal{M}(x)\right) \tag{1.1}$$

where $x \in \mathbb{R}^n$ is the original feature, while $\mathcal{M}(x)$ is a linear or a nonlinear map that maps x to a different n-dimensional space via transformations that preserve either local or global properties depending on the algorithm used, but gets rid of the correlation between the original variables. These algorithms aim to reduce dimensionality, reduce complexity and try to reveal the so-called latent variables necessary to describe the system after de-correlating the original n variables. In nuclear applications x can be the cross sections which are known to have noticeably high degree of correlation resulting from constraints dictated by either the physics or the designer herself.

These coefficients/features are usually determined via fitting or optimization with the discrepancy between the original and the surrogate model predictions driving a cost function for an optimization search. Depending on the type of analytic function employed, SC methods are categorized into two categories, *statistics (or data)* and *physics (or model)-based* methods.

www.manaraa.com

1.2.1.1 Statistics-based Surrogate Construction

In this category, the surrogate functional form is heuristically selected, relying either on the modeler's experience gleaned from a large number of model executions conducted over a wide range of operational conditions or dictated by techniques such as Guassian Processes. Analysis of these executions provides observable trends that enable the modeler to identify a palette of mathematical functions that she believes are representative of the model behavior over the range of conditions of interest to the application.

A wide variety of methods falls under this category such as linear regression, polynomial chaos expansion, stochastic collocation, Lagrange polynomial expansion, polynomial response surface (PRS), radial basis function (RBF), radial basis neural network (RBNN), kriging (KRG), support vector machines (SVMs), etc.[1, 2].

SC methods have been widely used and developed independently in many scientific fields for model approximation, validation studies, and design optimization, etc. For example, in 1998 Isukapalli [3] employed stochastic response surface methods (SRSMs) to propagate uncertainties in environmental and biological systems such as estimating doses of toxic chemicals in human body to get around the prohibitive number of simulations dictated by the standard Monte Carlo and Latin Hypercube Sampling and hence lends feasibility to comprehensive uncertainty characterization of real-world complex applications. Few years later (2001), (Kennedy and O'Hagan) [4] used Kriging (Gaussian Process) to build surrogates for black-boxed computationally expensive models. One year later Doebling et al. [5, 6] proposed a metamodel response surface of the LANL threaded assembly that enables a better validation framework for structural dynamics. Giunta et al. (2004) [7] used different sampling methods to

www.manaraa.com

build a response surface of a Rosenbrock function. Chen et al. (2006) [8] developed a surrogate using tensor product basis functions to perform sensitivity analysis and uncertainty quantification to optimize the design of an engine piston. Liem (2007) [9] developed a multi-agent collective method on an aviation system for environmental impact by estimating aircraft emissions. Bliznyuk et al. (2008) [10] hybridized RBF and Gaussian Processes interpolants with Markov Chain Monte Carlo. Of course the RBF and the GPs interpolants aimed to reduce the computational cost and hence lend feasibility to the MCMC integrals.

Surrogate models have been widely employed in the nuclear engineering community, starting from Hevesi et al. (1992) [11] who employed co-Kriging to infer precipitation values of a nuclear waste site using sparse measurements, then Roston et al. (1996) [12] who focused on modeling excessive vibration of control rods by hybridizing physical models with neural networks. This was synchronized with the book [13] published by Uhrig & Tsoukalas, which synergistically combined fuzzy and neural networks to gain feature extraction and modeling capabilities of both approaches. Next Hines & Uhrig (2005) managed to address issues facing the operation of nuclear power plants with computational intelligence such as noise analysis, regularization of ill-posed problems, on-line monitoring and sensor validation [14]. Few years later Fouet and Probst (2009) used Surrogates to perform sensitivity analysis during Large Break LOCA on ZION nuclear power plant [15]. Khalafi et al. (2011) then developed an artificial neural network to predict neutronics and thermo-hydraulics parameters in a large VVER nuclear reactors [16]. In 2004 Krivtchik et al. managed to build a surrogate model for a depletion code for uncertainty propagation [17]. Lockwood & Anitescu (2011) developed a gradient-enhanced universal Kriging model for uncertainty propagation in nuclear engineering applications [18].

www.manaraa.com

Finally, Yankov (2015) presented a full analysis of reactor simulations using non-intrusive techniques to build the surrogate models such as kriging and anchored-ANOVA decomposition [19] coupled with collocation techniques.

Polynomial Chaos techniques were born from the stochastic finite elements and had been conducted in nuclear applications, aiming to expand variables from the governing partial differential equations in terms of orthogonal polynomials usually followed by some sort of orthogonal projection such as Galerkin projections. Nuclear engineers often look at this from the same perspective as expanding scattering cross sections in terms of Legendre polynomials. Similar to other spectral methods, this enables the collocation of Uncertainty Quantification (UQ) under the generality of stochastic sampling but still inherit the accelerated convergence of the deterministic methods. In (2007) Williams [20] used polynomial chaos to trace how random material properties can affect radiation transport through a slab. In (2011) Fichtl and Prinja [21] employed polynomial chaos-collocation to draw a picture of how the uncertainties in total cross sections reflect in the scalar flux probability density function in both absorbing and diffusive media. Nonlinear polynomial chaos was conducted by Ayres and Williams (2013) [22] to relate uncertainties in cross sections to uncertainties in eigenvalue, they leveraged the use of linear methods against the non-linear conventional polynomial chaos by performing some sort of simultaneous diagonalization of matrices which yielded accurate results yet faster than the nonlinear PC with a factor that sometimes reaches more than 100.

SC methods have received large popularity because they can be applied in a non-intrusive manner, meaning that no code modifications nor direct knowledge of the model details are required. Nevertheless, it is challenging to quantify the errors resulting from the surrogate approximations in a manner that allows for a credible extrapolation of surrogate predictions to a

www.manaraa.com

wider range of operational conditions. This is because many of these surrogate model forms are selected statistically, i.e., not informed by the physics of the simulation. This limits the use of surrogate models constructed in this fashion to be used for interpolation purposes only, typically done at points in the parameter space which are close to the training points used to determine the unknown coefficients/features of the surrogate model. The second challenge facing SC methods is that the number of model executions required for training can be overwhelmingly high for complex models such as those encountered in reactor analysis problems. This is because the number of required model executions is a function of the number of parameters as well as the order of the nonlinearity of the model, that is to say, if the modeler is building a linear surrogate for a model with n parameters then, at a minimum n executions of the original model are required. This could be prohibitive in reactor physics where the number of parameters could be in the order of 10^6. For higher order models, e.g., 2^{nd} order, the number of model executions typically grow exponentially, which is often referred to as the curse of dimensionality.

1.2.1.2 Physics-based Surrogate Construction

Physics-based SC methods derive the functional form of the surrogate using the physics equations governing the behavior of the original model. This approach precludes the need for selection of functions, fitting, and training. Most importantly, one can establish robust error bounds on the surrogate model predictions which can be defended mathematically, thereby allowing the surrogate model to be extrapolated over the entire range of applicability of the original model. The primary challenge is that one must have an intimate knowledge of the inner anatomy of the model, implying knowledge of governing equations, types of solvers and sometimes the availability of an adjoint solver is required. One example of such approach is the exact-to-precision generalized perturbation theory (E_PGPT) surrogate model developed by Wang

www.manaraa.com

et. al., 2013 [23], where he combined reduced basis methods, range finding algorithms with generalized perturbation theory to construct a unified framework that enables the reduction of high overhead computations involved in reactor calculations with errors that are within the machine precision and hence came the terminology Exact-to-precision generalized perturbation theorem (E_PGPT). Another example would be the work of Mickus et al. (2014) [24] work which proposed an approach to physics-based surrogate for application with Integrated Deterministic Probabilistic Safety Assessment. In this method, the authors chose not to use the well-known Neural Networks methods since there is no actual physics modeling rendered, in addition to the huge number of data points required for the fitting process. This leads to some lack of reliability and robustness of the surrogate model outside the experimental domain given that any extrapolation will acquire no physics reasoning. Instead, the authors selected the most important physical phenomena to be resolved by the surrogate model and then calibrated the model to capture parameters that were not directly modeled in the surrogate and hence arrived at an intermediate stage between pure neural networks and analytical solutions.

1.2.2 Dimensionality Reduction (DR)

Instead of finding an approximate function to replace the original function *f*, DR techniques attempt to reduce the intrinsic dimensionality of the model variables, such as the input parameters and/or the output responses, which are related by the function *f* which remains unchanged. This is accomplished by searching for correlations between the variables which, if present, the implication is that the intrinsic dimensionality of the variables may be much less than the nominal dimensionality. In such case, one can identify a small number of reduced variables which can be used to describe the dominant features of the model variations over the expected range of operational conditions. This can be mathematically expressed as:

www.manaraa.com

$$f(x) \approx f(\mathcal{M}(x)) \tag{1.2}$$

where $x \in \mathbb{R}^n$ is the original *n*-dimensional feature and $\mathcal{M}(x)$ is again either a linear (LDR) or a nonlinear map (NDR) that maps the original feature to a world of non-correlated variables.

If the relationship between the reduced variables and original variables is linear, the reduced variables are described by subspaces, denoted hereinafter by "active subspaces", and the reduction methods are referred to as linear DR or LDR for short. The use of subspaces provides two advantages, a geometric advantage which allows one to provide an intuitive understanding of the mechanics of reduction, and a mathematical advantage wherein linear algebra and matrix theory methods may be leveraged to describe the reduction [25-28].

In LDR, all variables variations that are orthogonal to the active subspaces are considered to have a negligible impact on the model behavior as measured in terms of its key responses of interest. This implies that the physics model as applied to the engineering application of interest constraints the variables variations to the active subspace, and/or that variables variations that are orthogonal to the active subspace have very low sensitivities for the responses of interest.

The implication of LDR is that one can recast many engineering analyses whose cost directly depends on the number of input parameters and/or output responses into a reduced form that is described by the reduced variables.

Examples include Uncertainty Quantification (UQ), Sensitivity Analysis (SA), and Data Assimilation (DA), whose cost is known to be very sensitive to the number of model variables. Earlier work has shown that for typical reactor analysis models, the number of variables could be

www.manaraa.com

in the order of 10^4-10^9 whereas the number of reduced variables is in the order of 10^2 variables only. This dramatic reduction can enable these analyses to be computationally tractable.

For LDR methods to be reliable, one must be able to characterize the errors resulting from constraining the variables variations to the active subspaces only. This represents one of the objectives of this thesis where the aim is to develop upper-bounds on the LDR errors when the reduction is rendered at some or all of the models interfaces, including the parameters and the responses for single and multi-physics models.

It is important here to note that LDR methods have been researched for over a century by many scientists from different backgrounds with the same idea forming the basis for many methods. The first LDR method can be traced back to the work by Karl Pearson [29] in 1901 on Principal Component Analysis (PCA). The PCA method searches a number of multi-dimensional snapshots for the most informative directions that can be used to describe the data variations to a user-defined tolerance. About 30 years later, the same idea was further developed by Hotelling (1933) [30] which remained popular in the multivariate quality control community under the name of Hotelling Transformation. The basic idea of LDR found its way in the works of many scientists in a wide number of scientific disciplines. For instance, the Karhunen-Loeve Transformation (KLT) commonly employed in the signal processing community, the Proper Orthogonal Decomposition (POD) in the mechanical engineering community, the Singular Value Decomposition (SVD) in the linear algebra community, the Eckart-Young theorem (Harman, 1960) or Schmidt-Mirsky theorem in psychometrics, the Empirical Orthogonal Function (EOF) in the meteorological science, and spectral decomposition in vibration community, all represents examples of methods with roots in linear dimensionality reduction.

www.manaraa.com

Another important extension of the basic LDR idea is the work by Fisher on Linear Discriminant Analysis (LDA) in 1936 for classification [31]. LDA expands the dependent variables as a linear combination of measured features by searching for a linear map to maximize some measure of separability between data points to allow for credible classification.

Before ending this section, we note that DR may be rendered in a nonlinear manner as well, meaning that the relationship between the original and reduced variables may be selected to be nonlinear, implying nonlinear dimensionality reduction or NDR for short. NDR methods are categorized into three families depending on what the method preserves while searching for the required map (i.e., the linear or nonlinear transformation of the original and the reduced variables): methods that preserve local properties such as Local Linear Embedding (LLE) [32], Laplacian Eigen Maps [33], and Hessian Local Linear Embedding (HLLE) [34], methods that preserve global properties such as Multidimensional Scaling (MDS) [35], Isomaps [36], Kernel PCA [37], diffusion maps [38], Generalized Discriminant analysis (GDA) [39, 40], Multilayer Autoencoder [41], Stochastic Neighbor Embedding (SNE) [42]. Or methods that perform global alignment of local properties like Locally Linear Coordination (LLC) [43].

NDR methods will not be discussed here, and the interested reader may consult [25, 44-47] for more details and comparisons between them. NDR methods are out of our scope for several reasons: First, the payoff of LDR methods for reactor physics applications is sufficiently large and the methods have not yet been fully explored in the nuclear engineering community. Therefore, it is reasonable to leverage LDR methods first before considering more sophisticated NDR strategies. Second, the computational cost of reactor physics methods is extremely taxing which renders NDR methods less attractive since their associated computational cost is typically much higher than LDR methods.

www.manaraa.com

And finally, because NDR usually succeeds on tailored highly nonlinear problems such as the well-known Swiss roll dataset, while the real applications success for NDR is scarce, especially that a vast number of NDR techniques flourish with complex topologies, high curvatures, clustered, noisy, or sparse data, which is not the case in nuclear applications [48].

1.2.2.1 Mathematical Representation of LDR Methods

A nonlinear function f with n input parameters and m output responses is said to be reducible and of parameters intrinsic dimension $r_x (0 < r_x \le n)$ and response intrinsic dimension $r_y (0 < r_y \le m)$ if there exists an $n \times n$ operator $\mathbf{P}_x$ with a rank of r_x and an $m \times m$ operator $\mathbf{P}_y$ with a rank of r_y such that r_x and r_y are the smallest integers satisfying:

$$\left\| \frac{f(x) - \mathbf{P}_y f(\mathbf{P}_x x)}{f(x)} \right\| \le \varepsilon \quad \forall x \in S.$$

where $\|*\|$ used throughout this thesis is the Euclidean norm and ε is a user-defined tolerance, and S is the domain over which the original model is considered to provide an acceptable representation of real behavior, typically referred to as the domain of validity of the original model. Notice that we are not concerned here with the question of whether the original model is valid or not. Instead, we are only interested in building a reduced model that approximates the original model for all conditions of interest. These conditions are typically determined when the domain of validity of the original model is known, which is assumed to be a pre-requisite for the reduction process.

www.manaraa.com

In our context, $\mathbf{P}_x$ and $\mathbf{P}_y$ are projector operators onto the parameter space and response space respectively, such that $\mathbf{P}_x = \mathbf{U}_x \mathbf{U}_x^T$ and $\mathbf{P}_y = \mathbf{U}_y \mathbf{U}_y^T$ where $\mathbf{U}_x \in \mathbb{R}^{n \times r_x}$ and $\mathbf{U}_y \in \mathbb{R}^{m \times r_y}$ are matrices containing the orthonormal columns spanning the active parameter and response subspaces respectively. The intrinsic dimensionalities of these operators, i.e. $\dim\left(\mathrm{R}\left(\mathbf{P}_z\right)\right) = r_z;\ z = x, y$ - with R being the range of the operator $\mathbf{P}_z$ - are typically much smaller than the original dimensions of the parameters and responses spaces, i.e. $\max(r_x, r_y) \ll \min(m, n)$. The algorithms to construct these matrices are discussed in details in Chapter 3. Further, we show that this inequality condition may be satisfied in a probabilistic sense with a high probability of $1\text{-}10^{-s}$, where s is a small integer representing an additional number of model executions, referred to as over-samples, more details about this will be presented in Chapter 4.

We make several remarks about this LDR definition. First, note that the definition makes no assumptions about the properties of the function f, implying that while the relationship between the reduced and original variables is linear, as given by the above equation, the function f being reduced can, in general, be nonlinear.

Second, ensuring that the above inequality condition is satisfied with an upper-bound ε that is not too conservative employing a reduced dimension r that is not too large represents the primary challenge of LDR techniques. Satisfying this condition with a conservative bound is not practical as the bound is often too large to render valuable the predictions of the reduced model variables for subsequent engineering analyses. Satisfying the condition with a high r value is also not practical as it defeats the whole purpose of reduction, that's to reduce the dimensions significantly to render subsequent engineering analysis computationally tractable. In many vital

www.manaraa.com

models, the original model dimensions are in the order of millions, whereas the reduced model dimension is sought to be in the order of few hundred variables only. With limited model evaluations of the order of the reduced dimension *r*,

Third, if the inequality condition can indeed be satisfied with small *r* and acceptable tolerance ε, the implication is that a limited number of degrees of freedom *r* in the active space is sufficient to characterize to a high level of accuracy all possible response variations, whose original dimensionalities are often much larger than *r*. Mathematically, this means that parameter perturbations belonging to the active parameter subspace are the ones responsible for the observed model response variations, whereas all parameter perturbations that are orthogonal to the active subspace induce negligible variations in the responses, which can be bounded by the tolerance ε.

Finally, to gain computational efficiency in subsequent engineering analyses requiring multiple model executions, ROM confines all parameter perturbations to the active subspace, since its dimensionality is much smaller than the original parameter space. For example, one can recast all engineering analyses, such as UQ and SA, in terms of the reduced variables $x^{(r)} = \mathbf{U}_x^T x \in \mathbb{R}^{r_x}$, premised on the assumption that they describe all important parameters variations.

In this thesis, the focus will be on reducing the effective dimensionality of the various data streams associated with neutronic calculations. This includes reducing the dimensionality of the cross-section space and the flux space. The developed methods will be applied to representative assembly level calculations, where the size of the cross-section and flux spaces are typically large. Assembly level calculations are carried out to characterize the few-group cross-

www.manaraa.com

sections used in downstream core calculations as functions of a wide range of conditions, such as the assembly type, fuel burnup, fuel and coolant temperature, poison content, etc. This requires several thousands of flux evaluations which could be rendered more efficiently using ROM methods.

In our development, we rely on two basic ROM methods, gradient-free and gradient-based reduction. The gradient-free reduction is designed to render reduction at the output interface for the associated model using forward model executions only. Gradient-based reduction employs derivative information, often obtained using adjoint methods, to render reduction at the input interface. Earlier work has demonstrated the theoretical and implementation details of these two methods. Experience with these methods has shown that although significant reduction can be rendered, the number of model executions could still be computationally expensive. Further, the quantification of the reduction error could be problematic especially when multiple reductions are rendered at model-to-model interfaces. These two challenges are addressed in this thesis.

www.manaraa.com

CHAPTER TWO

NUCLEAR REACTOR CALCULATIONS

2.1 Design Calculations

Nuclear reactor physics calculations, representing the focus of our work, are overviewed in this chapter. Reactor physics calculations model the transport of neutrons inside the reactor core and the change in fuel isotopics and other core materials due to radioactive transmutation over the expected range of reactor operational conditions. The fundamental equations employed are the Boltzmann equation which describes the transport of neutrons and the Bateman equation which describes the transmutation of fuel and other core materials isotopics. The salient features of these equations are described here to set the stage for the discussion of ROM methods.

The primary source of heat in fission reactors is due to the scission of heavy nuclei by slow (i.e., thermal) or energetic (i.e., fast) neutrons. Shortly after the scission of a nucleus, two lighter nuclei, called fission fragments, few neutrons, called prompt neutrons, and few gamma rays, called prompt gamma, are released. The majority of the mass defect, the difference between the mass of the original heavy nucleus and the combined mass of lighter fission fragments and prompt neutrons, is released in the form of kinetic energy imparted to the fission fragments and prompt neutrons. One typical fission reaction is described by the following equation:

$$n + {}^{235}_{92}U \rightarrow {}^{140}_{54}Xe + {}^{94}_{38}Sr + 2n + 200MeV$$

As the fission products collide with surrounding atoms, they slow down converting the kinetic energy into heat. The heat generation is sustained via additional fission events induced

www.manaraa.com

primarily by the newly born neutrons. The goal of reactor core design is to ensure that the number of neutrons born in a given generation is equal to the number born in the previous generation to ensure the reaction is sustainable and controllable. When this balance is established, the reactor is said to be critical, with the criticality described using the multiplication factor *k* which measures the ratio of neutrons production to neutron loss by parasitic absorption and leakage. Parasitic absorption implies a neutron capture event that does not lead to fission, e.g., the capture of neutron under the low-lying resonances of U-238, captured by special materials, called neutron absorbers, deliberately introduced into the reactor to control criticality. The goal is to keep *k* at a value of 1.0 throughout operation by continually balancing neutron loss and production terms. When $k < 1.0$ or $k > 1.0$, the number of neutrons will decrease or increase forming subcritical or supercritical reactors, respectively. When the reactor power is to be increased, *k* is increased for a short period of time by reducing neutron loss until the desired power level is reached, then *k* is returned back to a value of 1.0.

To compute and control *k*, one needs to model in detail the transport and transmutation of neutrons inside the core along with the various physics phenomena leading to the production and loss of neutrons. Although the physics of transport and transmutations are well-understood, the associated computational cost to describe the neutron population in the entire reactor core is still considered computationally overwhelming even for supercomputers. To combat this situation, reactor physicists have devised complex schemes to reduce the computational cost to render practical the prediction of reactor states under the wide range of conditions expected during normal and off-normal operation. The idea is highlighted in the figure 2-1, where the calculations are split over multiple levels to capture the various physics affecting the macroscopic core behavior.

www.manaraa.com

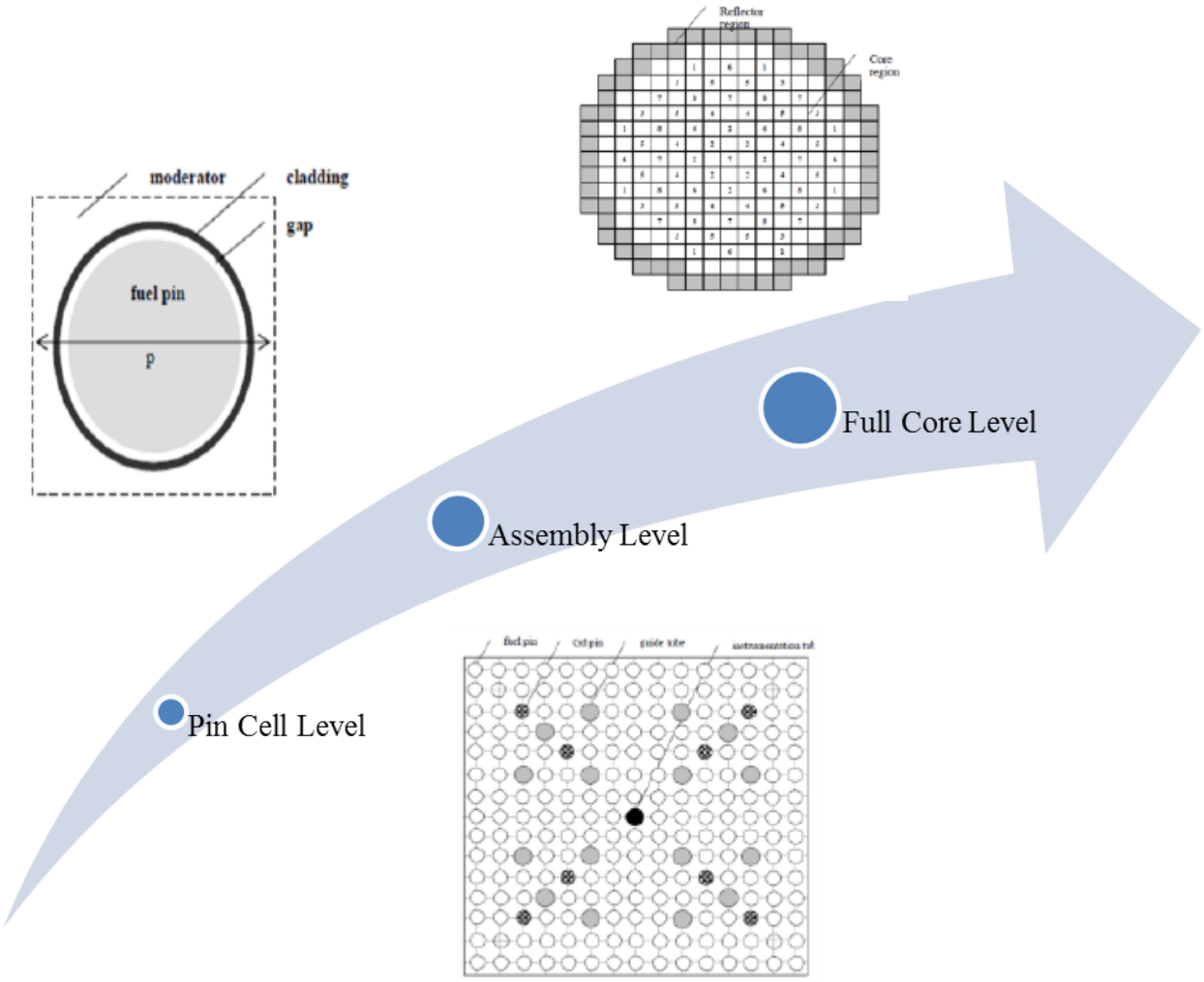

Fig. 2-1. Core Calculation Levels.

The smallest level represents the unit cell comprising a single fuel pin. The second level is the fuel lattice, representing a 2D slide of a fuel assembly. The third level is a 3D model of the whole core. These three levels are designed to decouple the dominant dependencies of the nuclear cross-sections (i.e., space, energy, angle, and time).

www.manaraa.com

Cross-sections are the basic nuclear parameters that characterize the probability of interaction between neutrons and various core materials. Given the complicated dependence of cross-sections and the heterogeneous core design, the neutron flux becomes a complicated function of space, energy, angle, and time. The first two level focus in detail on the energy, and angle dependence of the neutron flux, whereas the third level describes in details the spatial and temporal dependence. This separation of dependencies has proven to be an effective approach for reactor physics calculations. Before explaining these levels, we introduce the neutron transport equation to highlight some of the challenges associated with its solution for reactor problems. Figure. 2-2 depicts the flow diagram for the calculation procedure.

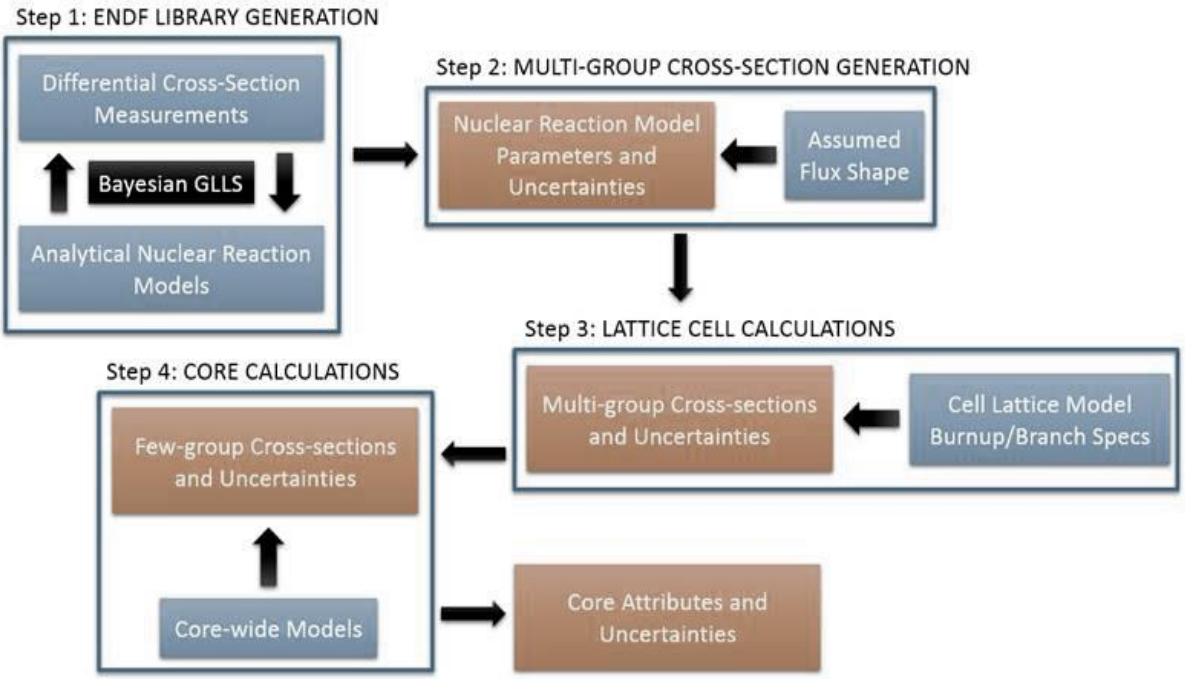

Fig. 2-2. Computational Sequence.

For a fast overview about the nuclear reactor calculation reader can consult the summarized chapter written by Keisuke Okumura, Yoshiaki Oka, and Yuki Ishiwatari.

www.manaraa.com

2.1.1 Neutron Transport Equation (Boltzmann Transport Equation)

The equation governing the neutrons distribution in a reactor core is referred as the Neutron Transport Equation (also known as the Boltzmann Equation) can be written in various forms due to the assumptions and simplifications that can be carried out to render the equation suitable for the required application and analytically solvable if possible. In most forms the dependent variable is the angular neutron flux in [#/cm^2 /sterad/ MeV/sec]

$$\underbrace{\frac{1}{v}\frac{\partial}{\partial t}\psi\left(\bar{r},\hat{\Omega},E,t\right)}_{\text{rate of change}}+\underbrace{\hat{\Omega}\bullet\bar{\nabla}\psi\left(\bar{r},\hat{\Omega},E,t\right)}_{\text{Leakage rate density}}+\underbrace{\Sigma_t\left(\bar{r},\hat{\Omega},E,t\right)\psi\left(\bar{r},\hat{\Omega},E,t\right)}_{\text{Total Collision rate}}=\underbrace{S_{ext}\left(\bar{r},\hat{\Omega},E,t\right)}_{\text{External source generation rate}}$$

$$+\underbrace{\int_0^\infty dE'\int_{4\pi}\Sigma_s\left(\bar{r},\hat{\Omega}'\to\hat{\Omega},E'\to E,t\right)\psi\left(\bar{r},\hat{\Omega}',E',t\right)d\hat{\Omega}'}_{\text{scattering Rate}} \qquad (2.1)$$

$$+\underbrace{\frac{\chi(E)}{4\pi}\int_0^\infty dE'\int_{4\pi}\nu\Sigma_f\left(\bar{r},E',t\right)\psi\left(\bar{r},\hat{\Omega}',E',t\right)d\hat{\Omega}'}_{\text{Fission rate}}$$

where ψ is the angular neutron flux [neutrons cm^{-2} sec^{-1} $sterad^{-1}$ MeV^{-1}], and Σ_f are the macroscopic total and fission cross sections, respectively in [cm^{-1}]; v is the average neutrons speed in [cm sec^{-1}]; ν is the average number of neutrons produced per fission reaction. The angular variable $\hat{\Omega}=\frac{\bar{v}}{\|\bar{v}\|}$ is a unit vector in the direction of the neutron travel and $\bar{r}$ is the position vector of the neutron. χ is the fission spectrum and finally Σ_s is the double differential macroscopic scattering cross section in energy and direction.

It is noteworthy that eq. (2.1) can only be analytically solved for a small number of idealistic scenarios which are considerably different from real reactor problems. The Boltzmann equation if a nonlinear integro-differential equation which must be solved in tandem with

www.manaraa.com

another equation, that describes the change in various materials concentrations, assumed to be input to the Boltzmann equation. For example, the macroscopic cross sections depend on the number densities, i.e., isotopic concentrations. Number densities are calculated using the Bateman equation which is a system of ordinary differential equations that are used to update the nuclei concentrations based on their respective production and loss terms. The production and loss terms depend on the neutron flux which is calculated by the Boltzmann equation. To decouple the Boltzmann and Bateman equation, the quasi-static assumption is typically used, where the reactor core is assumed to operate at steady state for a short period of time during which the number densities are assumed constant to solve for the flux; then the flux is used to calculate the production and loss rates for the various nuclei which are used to update the nuclei via the Bateman equation.

Given the steady-state assumption, the Boltzmann equation is assumed to have a solution, which is only possible if the reactor is critical. To overcome this, the k-eigenvalue is introduced as a knob that determines the deviation from criticality. The designers can change the various model features to ensure k is as close to 1.0 as possible throughout the core life. Eq. (2.1) can then be written as:

$$\hat{\Omega} \bullet \bar{\nabla}\psi\left(\bar{r},\hat{\Omega},E\right)+\Sigma_t\left(\bar{r},\hat{\Omega},E\right)\psi\left(\bar{r},\hat{\Omega},E\right)=\int_0^\infty dE'\int_{4\pi}\Sigma_s\left(\bar{r},\hat{\Omega}'\to\hat{\Omega},E'\to E\right)\psi\left(\bar{r},\hat{\Omega}',E'\right)d\hat{\Omega}' + \frac{1}{k}\frac{\chi(E)}{4\pi}\int_0^\infty dE'\int_{4\pi}\nu\Sigma_f\left(\bar{r},E'\right)\psi\left(\bar{r},\hat{\Omega}',E'\right)d\hat{\Omega}' \tag{2.2}$$

here the *k*-eigenvalue is the multiplication factor.

The next obstacle facing practitioners is the energy dependency of each term in the equation; cross sections trends show a rather complicated dependence on neutron energy. To

www.manaraa.com

render numerical solutions, the energy range is split over multiple ranges, where the cross-section is assumed constant over each range. These ranges are called neutron groups, and the corresponding constant values are referred to as group cross-sections. In the group representation, the Boltzmann equation may be re-written as:

$$\hat{\Omega} \bullet \bar{\nabla} \psi_g \left(\bar{r},\hat{\Omega}\right) + \Sigma_{t,g} \left(\bar{r},\hat{\Omega}\right) \psi_g \left(\bar{r},\hat{\Omega}\right) = \sum_{g'=1}^{Ng} \int_{4\pi} \Sigma_{s,g' \to g} \left(\bar{r},\hat{\Omega}' \to \hat{\Omega}\right) \psi_g \left(\bar{r},\hat{\Omega}'\right) d\hat{\Omega}' + \frac{1}{k} \frac{\chi_g}{4\pi} \int_0^{\infty} dE' \int_{4\pi} \nu_{g'} \Sigma_{f,g'} \left(\bar{r}\right) \psi_{g'} \left(\bar{r},\hat{\Omega}'\right) d\hat{\Omega}' \tag{2.3}$$

This equation is achieved by integrating eq. (2.2) w.r.t to energy over the g^{th} energy group (i.e., $\int_{E_g}^{E_{g-1}} \bullet dE$) where Ng is the total number of groups in the selected energy structure which is dictated by the required accuracy. The figure below shows the continuous cross-section and the group cross-sections which are piecewise constants. The primary challenge of reactor physics calculations is the ability to calculate the group cross-sections in a manner that preserves the reaction rates and the multiplication factor.

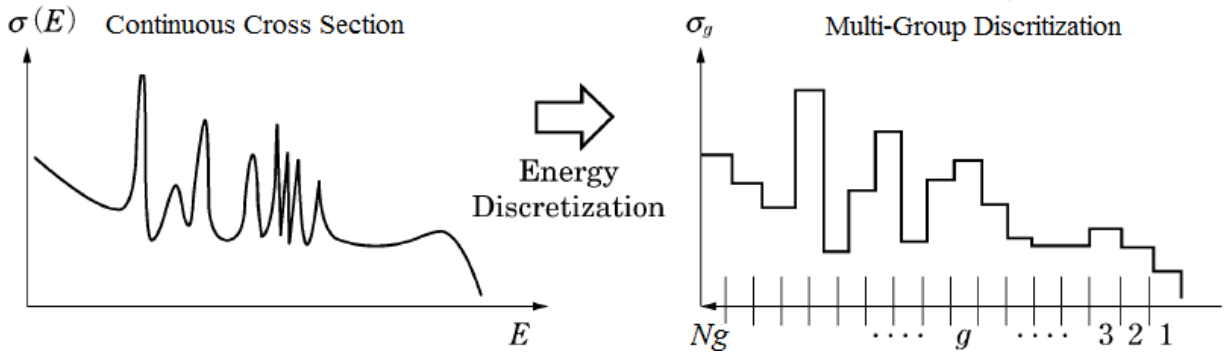

Fig. 2-3. Cross section discretization over energy. (Yoshiaki Oka et. al.)

www.manaraa.com

2.1.2 Multi-group Cross-section Generation

In this step, the pointwise cross-sections are collapsed into a multi-group structure using assumed flux shapes. This structure is decided based on an educated trial and error relying on expert judgment attempting to resolve all aspects of the flux spectrum, expected to affect the integral quantities of interest such as eigenvalue, reaction rates, etc.

The uncertainties of the multi-group cross-sections can be estimated by propagating the uncertainties of the nuclear reaction model parameters using the standard sandwich relationship. The multi-group cross-sections contain essentially two different sources of uncertainties, one originating from the nuclear reaction parameters used to construct the continuous cross-sections, and the other from the assumed flux shape. Most tools account only for the first source of uncertainty (assuming linearity). Whereas the flux shape uncertainty is difficult to estimate because the real flux shape is unknown a priori. Therefore, assumed flux shape uncertainty must be treated as a source of modeling uncertainty. To estimate this source, one must be able to compare the predictions against a high fidelity model that directly uses the continuous cross-sections, i.e., without any collapsing. The discrepancies between the predictions of the low and high fidelity models can be used estimate the modeling bias, which has to be repeated to take into account its dependence on other modeling conditions, such as composition, temperature, etc., i.e., control parameters. The group averaged cross sections are computed as follows:

$$\phi(E) = \int_{4\pi} \psi\left(\bar{r}, E, \hat{\Omega}\right) d\hat{\Omega} \tag{2.4}$$

$$\phi_g(\bar{r}) \equiv \int_{E_g}^{E_{g-1}} \phi(E, \bar{r})\, dE \tag{2.5}$$

www.manaraa.com

$$\int_{E_g}^{E_{g-1}} \Sigma_x(E,\bar{r})\phi(E,\bar{r})dE = \bar{\Sigma}_{x,g}(\bar{r})\phi_g(\bar{r}) \tag{2.6}$$

$$\bar{\Sigma}_{x,g} \equiv \frac{\int_{E_g}^{E_{g-1}} \Sigma_x(E)\phi(E,\bar{r})dE}{\int_{E_g}^{E_{g-1}} \phi(E,\bar{r})dE} \tag{2.7}$$

where *x* can be total, fission or absorption reaction.

$$\nu_g \equiv \frac{\int_{E_g}^{E_{g-1}} \nu(E)\Sigma_f(\bar{r},E)\phi(\bar{r},E)dE}{\int_{E_g}^{E_{g-1}} \Sigma_f(\bar{r},E)\phi(\bar{r},E)dE} \tag{2.8}$$

$$\frac{1}{\nu^g} \equiv \frac{\int_{E_g}^{E_{g-1}} \frac{1}{\nu(E)}\phi(\bar{r},E)dE}{\int_{E_g}^{E_{g-1}} \phi(\bar{r},E)dE} \tag{2.9}$$

$$\Sigma_{s,g'\to g} = \frac{\int_{E_{g'}}^{E_{g'-1}} dE' \int_{E_g}^{E_{g-1}} dE\Sigma_s(\bar{r},E'\to E)\phi(\bar{r},E')}{\int_{E_g}^{E_{g'-1}} \phi(\bar{r},E')dE'} \tag{2.10}$$

2.1.3 Lattice Cell Calculation

A lattice is a 2D slice of a fuel assembly, where the Boltzmann equation is solved using a large number of energy groups. The solution obtained for the flux is used to reduce the dimensionality of the cross-sections from many groups down to few groups, and averaged over

www.manaraa.com

the entire lattice. The few-group cross-sections are subsequently used in core-wide calculations which are 3D models of the entire reactor core. The goal here is to model each assembly as a group of axial nodes, where each node is represented in core-wide calculations as a uniform region with few-group cross-sections. This requires the ability to smear all the energy and spatial dependence of the cross-sections at the lattice level prior to entering core-wide calculations. This smearing process is referred to as homogenization and is carried out as follows.

In this step, one calculates the few-group cross-sections for the cell lattices. These calculations must be repeated every time a new cell lattice design is introduced. Cell lattice calculations start with the multi-group cross-sections and calculate the few-group cross-sections for a wide range of core conditions.

To provide an idea of the size of the data streams flowing through cell lattice calculations, consider a typical transport code that is used to calculate the few-group cross-sections. The code is to be executed a number of times equal to N_B x N_C x N_L times, where N_B refers to the number of burnup steps, and N_C is the number of branch cases required to functionalize cross-section dependence on core conditions such as fuel and coolant temperature, coolant voiding, boron content, etc., and N_L is the number of cell lattice types in the core. To propagate uncertainties, one would need to repeat these model executions N times, which is in the order of few to several hundred. This results in in the order of 10^5 model executions which is prohibitive in practical applications.

Further, if one is interested in identifying the dominant contributors to the propagated uncertainties via an SA, one needs to execute the solver a number of times that is proportional to the number of model parameters. In this case, the parameters represent the multi-group cross-

www.manaraa.com

sections. This increases the number of required code runs to be in the order of 10^6 to 10^9 executions, which is overwhelmingly high despite the expected increase in computer power.

In this step, two sources of uncertainties are introduced, one from the multi-group cross-sections propagated from the previous step, and the other resulting from the modeling assumptions, such as the use of reflective boundary conditions, the use of a deterministic transport solver, and the use of multi-group instead of continuous cross-sections. The first source is again straightforward to account for. The computational cost becomes impractical when sensitivity information is required, i.e., to understand the contribution of the individual multi-group cross-sections on the propagated few-group uncertainties.

The second source depends on the modeling decisions taken and therefore must be treated as a source of modeling errors. First, regarding the use of deterministic transport solver and multi-group cross-sections, this source could be identified by comparing model predictions against a high fidelity continuous cross-section Monte Carlo model. The second source is more difficult to account for because it depends on the type of neighboring bundles in the reactor core.

Finally, similar to the previous step, the correlations between the multi-group uncertainties and the modeling uncertainties (resulting from the transport model, multi-group cross-sections, and neighbors' approximations) are to be investigated.

This step can be accomplished through two sub-steps: Homogenization and Few-group Cross-section generation.

2.1.3.1 Homogenization. In this step, microscopic cross sections and number densities are averaged such that different mixtures of different materials are assumed to be a single homogenized mixture occupying the whole volume. This can be mathematically expressed as follows:

www.manaraa.com

$$\phi_g^h \equiv \frac{\sum_j \phi_{g,j} V_j}{\sum_j V_j} = \frac{\sum_j \phi_{g,j} V_j}{V^h} \tag{2.11}$$

Then cross sections can be computed such that:

$$\sum_j \Sigma_{x,g,j} \phi_{g,j} V_j = \Sigma_{x,g}^h \phi^h{}_g V^h$$

And hence:

$$\Sigma_{x,g}^h \equiv \frac{\sum_j \Sigma_{x,g,j} \phi_{g,j} V_j}{\phi_g^h V^h} = \frac{\sum_j \Sigma_{x,g,j} \phi_{g,j} V_j}{\sum_j \phi_{g,j} V_j} \tag{2.12}$$

Similar trend can be applied to the number densities:

$$N_i^h \equiv \frac{\sum_j N_j^i V_j}{V^h}; j = 1,2,\cdots N_{nuclides} \tag{2.13}$$

2.1.3.2 Few-Group Cross-section Generation. The homogenized values can then be used to prepare for the core calculations by collapsing the energies into a coarser structure. This will render the core calculations feasible with an acceptable error. This can be achieved using a similar procedure based on the conservation of reaction rates as follows:

$$\phi_{G_i}^h \equiv \sum_{g \in G_i} \phi_g^h; i = 1,2,\cdots NG \tag{2.14}$$

$$\Sigma_{x,G_i}^h \equiv \frac{\sum_{g \in G_i} \Sigma_{x,g}^h \phi_g^h}{\sum_{g \in G_i} \phi_g^h} \tag{2.15}$$

www.manaraa.com

where $NG<<Ng$. This can be used in core calculation to speed it out in addition to some acceleration algorithms such as the coarse mesh finite difference acceleration (CMFD) that will not be in the scope of this report.

2.1.4 Downstream Core-wide Calculations

The last stage involves the calculation of core-wide power distribution during steady state and transient conditions starting with the few-group cross-section data. The number of few-group cross-sections is equal to N_{FG} x N_B x N_C x N_L where N_{FG} is the number of few-group cross-sections generated per a single transport model execution, which is in the order of 10, representing the thermal and fast absorption cross-sections, transport cross-section, fission cross-sections, prompt neutron yield, and energy release, and Xe and Sm fast and thermal absorption cross-sections. If macroscopic depletion model for core calculations is used, the total number of few-group cross-sections is in the order of 10^4. If microscopic depletion models are used, this number is scaled by the number of nuclides tracked at the core level to account for the individual nuclides' cross-sections.

The sources of uncertainties in core-wide calculations include, uncertainties from the few-group cross-sections; uncertainties from the radiation transport model employed (e.g., nodal diffusion theory assumptions, and two energy-group cross-section representation); and uncertainties from non-neutronic models, e.g., thermal-hydraulics models, and their associated correlations used to describe the transfer of the heat from the fuel to the coolant, and the corresponding feedback into neutronics calculations, e.g., fuel temperature feedback, coolant and moderator temperature and density feedbacks; and finally any uncertainties from the control

www.manaraa.com

parameters such as the lattice dimensions, fuel composition, flow rates, inlet coolant temperatures, etc.

The first source, i.e., few-group cross-section uncertainties, can be treated using a standard UQ. The second source, i.e., the radiation transport model, can be estimated using the UQ methodology via core-wide Monte Carlo models.

This concludes the main flow of many neutronics codes, for more details reader can consult one of the codes manuals such as SCALE, POSEIDON, and CRANE [49-51].

www.manaraa.com

CHAPTER THREE

REDUCED ORDER MODELING

3.1 Introduction

Reduced Order Modeling (ROM) is sought to render computationally intensive tasks such as design optimization, UQ [3, 8, 53-55], SA [58-64] and DA [65-70] practically feasible for real-world engineering models. ROM leverages an interesting property of most complex models that is their associated input parameters and/or responses of interest live in low-dimensional manifolds. This occurs because although the physics models may be general enough, the engineering application introduces many constraints which result in introducing many correlations which reduce the effective dimensionality of the system. The reduction can, therefore, be introduced at the various model interfaces. For example, one can reduce the dimensionality of the parameter space which allows one reduce the computational cost associated with investigative studies that attempt to identify the key parameters. The reduction can also be introduced at the state space, which could be leveraged to reduce the computational cost required to obtain numerical solutions for the state. The reduction can also be applied to the responses of interest, especially when the responses represent distributions over the entire phase space. Depending on where the reduction is applied, different methods have been developed which are discussed in this chapter. Moreover, depending on how much reduction is introduced, the associated reduction errors are calculated and upper-bounded using rigorous methods. In the next section, a quick literature review is deducted then the algorithms used are shown.

www.manaraa.com

3.2 Literature Review

As discussed in the introductory chapter, linear dimensionality reduction techniques have been employed by analysts to reduce the dimensionality of multi-dimensional data for over a century. In the past 15 years, interest in these techniques has been revived to support the surge witnessed in the area of predictive modeling, where high fidelity models utilizing the cheap and abundant computer power are sought to provide a better understanding of complex systems behavior such as nuclear reactors. In 2004, Abdel-Khalik [52] presented the idea of LDR under the name of efficient subspace methods (ESM), where the subspaces represent lower dimensional manifolds onto which the model variables are projected. Later, the terminology of 'active subspaces' was adopted by other researchers such as Russi in 2010 [54], Constantine in 2012 [56], and Webster in 2012 [57], and Abdel-Khalik in 2010 [58, 59], emulating the language of active constraints from optimization theory. The notion of active implies that variables variations along the subspaces impact the model behavior, whereas variations over the orthogonal complements, i.e., the "inactive", as called by Abdel-Khalik in 2010, or "passive", as called by Webster in 2012, subspaces, have negligible impact on the model behavior as measured in terms of a number of user-selected quantities of interest.

Since then a lot of work on LDR has appeared under the name of subspace methods or active subspace methods. One can also trace the use of this terminology to the work by Erkki Oja in 1983 on pattern recognition [72] who started at the Institute of Physiology at the University of Finland exploring how the brain works, studying the neurons was the natural entrance for the machine learning and artificial intelligence world. In 1982 he managed to simplify the neuron model as a principal component analyzer, a year later he collected his linear methods in a book

www.manaraa.com

called ‘subspace methods of pattern recognition’ where he included rigorous mathematics along with interesting engineering applications for subspace methods.

Notice that in principle one can find an infinite number of active subspaces that meet a user-defined present tolerance, which bounds the discrepancies between the original functions predictions and the reduced function predictions. The goal is to find a subspace that is not necessarily unique, with a very small size r_x to capture the dominant parameter variations. In our work, we show that one can find an active subspace with slightly larger size in a computationally efficient manner that outperforms existing algorithms attempting to find the smallest possible active subspace. This is possible using our proposed multi-level ROM strategy which employs approximate models, i.e., models of lower fidelity, or models constrained to sub-domains of the overall problem domain, to obtain an approximation for the active subspace.

The remaining sections discuss how the active subspaces are extracted. Although a great number of algorithms have been proposed by various researchers, one could argue that all methods rely on one of two essential ideas. The first idea employs randomized snapshots of the forward model simulations to identify an active subspace for the model output responses or state variables. In the second idea, snapshots of the gradient of the model responses with respect to its input parameters are used to identify an active subspace for the model parameters. Hybridization of these two techniques allows one to reduce the dimensionality of multi-physics models, wherein the input to one physics model is produced as an output by a pre-processor physics model [71].

www.manaraa.com

3.3 Reduction Algorithms

This section is dedicated to providing a comprehensive overview of the theories and algorithms that form the basis for our rendition of reduced order modeling to general nonlinear models. In particular, the next 3 subsections will cover the following three subjects: identifying the active input subspace for a scalar valued function, identifying the active input subspace for a vector-valued function, and finally identifying the active response subspace algorithm [73].

3.3.1 Active Input Subspace Identification Algorithm (AISIA) for a scalar-valued function:

Let $f:\mathbb{R}^n \to \mathbb{R}$ be a scalar-valued nonlinear function that maps an *n*-dimensional input vector of model parameters such as cross section into a single response such as the effective multiplication factor k_{eff}. The goal is to determine the important directions in the parameter space, i.e., directions along which a perturbation in the model parameters will cause a noticeable impact on the response of interest. Notice that if the model is linear, there is only one such direction, that's the gradient of *f* with respect to the model parameters. For general nonlinear models, however, there could be as many as n directions that affect the response. The goal of the reduction is to identify r_x directions that capture the response variations to a given preset tolerance □. Ideally, r_x should be much less than *n*, the nominal dimension of the input parameter space. The subspace forming the span of the r_x directions is referred to as the active subspace $\mathcal{X}_{act} := span\left\{u_{x,i}\right\}_{i=1}^{r_x}; u_{x,i} \in \mathbb{R}^n$, meaning that the original feature *x* can be written as the sum of an active variable and a non-active one as follows:

www.manaraa.com

$$x = \mathbf{U}_x \mathbf{U}_x{}^T x = \begin{bmatrix} \mathbf{U}_x^{(r)} & \mathbf{U}_x^{(n-r)} \end{bmatrix} \begin{bmatrix} \mathbf{U}_x^{(r)T} \\ \mathbf{U}_x^{(n-r)T} \end{bmatrix} x = \mathbf{U}_x^{(r)} \underbrace{\mathbf{U}_x{}^{(r)T} x}_{\textit{active}\text{ variable}} + \mathbf{U}_x^{(n-r)} \underbrace{\mathbf{U}_x{}^{(n-r)T} x}_{\textit{inactive}\text{ variable}}$$

where $\mathbf{U}_x^{(r)} \in \mathbb{R}^{n \times r_x}$ is the matrix whose orthonormal columns span the active subspace, or in other words: The active subspace is the range of $\mathbf{U}_x^{(r)}$, $\mathcal{X}_{act} \equiv \mathcal{R}\left(\mathbf{U}_x^{(r)}\right)$. The superscript indicates that the new attribute $x^{(r)} = \mathbf{U}_x^{(r)} x$ is a reduced input vector due to a linear projection of the original feature *x* onto the active subspace. The matrix $\mathbf{U}_x^{(r)}$ contains r_x columns which span the active input subspace.

One may visualize this considering a two-dimensional function *f* that is intrinsically one-dimensional (i.e., i1D) [74] such that:

$$f(x) = f\left(\begin{bmatrix} x_1 & x_2 \end{bmatrix}^T\right) = g\left(u_1^T x\right);$$

Then the Fourier transform of such a function will be:

$$F(w) = G\left(u_1^T w\right) \delta\left(\left(\mathbf{I}_2 - u_1 u_1^T\right) w\right)$$

where *F, G* are the Fourier transforms of *f* and *g* respectively. As follows:

$$\mathcal{F}\{f(x_1, x_2)\} = F(w) = \int_{\mathbb{R}^2} e^{-i2\pi\left(w^T x\right)} f(x)\, dx = \int_{-\infty}^{\infty} \int_{-\infty}^{\infty} e^{-i2\pi\left(w_1 x_1 + w_2 x_2\right)} f(x_1, x_2)\, dx_1 dx_2$$

$$\mathcal{F}\{g(\tilde{x})\} = G(\tilde{w}) = \int_{-\infty}^{\infty} e^{-i2\pi\left(\tilde{w}\tilde{x}\right)} g(\tilde{x})\, d\tilde{x};$$

www.manaraa.com

and $\tilde{x} = u_1^T x$, $\tilde{w} = u_1^T w$ are the reduced variables in both the original and the frequency domains. With δ being the Dirac-delta function, the Fourier transform for f states that the function vanishes in the directions normal to u_1 and changes governed by the function G in the directions parallel to u_1. This can be generalized to the case where the nominal dimension is *n* and the intrinsic dimensionality is r_x and $f(x) = g\left(\mathbf{U}_x^{(r)T} x\right)$. In this case, the variation of the function in the directions parallel to the subspace spanned by the r_x orthonormal columns of $\mathbf{U}_x^{(r)}$ significant when compared to the negligible impact on f caused by an input vector that is perpendicular to that subspace. The identification of such active subspaces is accomplished using a gradient-based algorithm that constructs an active subspace in the input parameter space employing the adjoint model to calculate the first order derivatives of a general pseudo response with respect to input parameters. The pseudo-response is not a physical quantity but a mathematical abstraction representing a random linear combination of all model responses. For a justification of the use of pseudo-responses, the reader may consult section 3.3.2.1. The algorithm may be described by the following steps:

Inputs: $x_{ref} \in \mathbb{R}^n$ is the reference input vector (i.e., cross sections).

δx is the relative perturbation from the reference value.

$f : \mathbb{R}^n \to \mathbb{R}$ is the forward model of interest.

$f^{adj} : \mathbb{R}^n \to \mathbb{R}$ is the adjoint model (needed to compute the sensitivities).

1. Set $\mathcal{X} = \left\{ x : x \in \mathbb{R}^n ; x_{ref}\left(1-\delta x\right) \le x \le x_{ref}\left(1+\delta x\right) \right\}$ is an *n*-dimensional hyperrectangle.

www.manaraa.com

2. Generate k random realization $\{x_i\}_{i=1}^{k}; x_i \in \mathcal{X} \sim [x_{ref,i} - \delta x, x_{ref,i} + \delta x]^n$.

3. Initialize: $\mathbf{J} = []$.

4. *for* i = 1 to k

5. $y_i \leftarrow f(x_i)$

6. $j(x_i) \leftarrow (\nabla y_i)^T$

7. $\mathbf{J} \leftarrow [\mathbf{J}, j(x_i)]$.

8. $[\mathbf{U}_x, \Sigma_x, \mathbf{V}_x] \leftarrow svd(\mathbf{J})$.

9. $$\mathbf{E} = \left\| \frac{f(\mathbf{X}_{test}) - f(\mathbf{U}_x(:,1:i)\mathbf{U}_x^T(:,1:i)\mathbf{X}_{test})}{f(\mathbf{X}_{test})} \right\|.$$

10. $\varepsilon_b \leftarrow$ Construct an error bound as shown in section (4.3.4).

11. *If* $\varepsilon_b \leq \varepsilon_{user}$

12. $r_x \leftarrow i$.

13. $\mathbf{U}_x^{(r)} = \mathbf{U}_x(:,1:i)$.

14. Return

15. end if

16. end for

17. $r_x = k, \mathbf{U}_x^{(r)} = \mathbf{U}_x$ (no reduction occurred).

www.manaraa.com

3.3.2 Active Input Subspace Identification Algorithm (AISIA) for Vecor-valued functions:.

For $f:\mathbb{R}^n \to \mathbb{R}^m$, the above algorithm can be intuitively repeated for each component in the response vector and hence find an individual active subspace for each of the *m*-components as presented by Russi (2010). This renders the process impractical for large number of responses and hence motivates for the pseudo-response trick.

3.3.2.1 The Pseudo-response Trick:

Earlier work [73] has shown that vector-valued functions can be tackled using the pseudo response which is a non-physical quantity and hence find an individual active subspace for each of the *m*-components. This starts to be impractical right after *m* exceeds 10. In a typical reactor physics application, *m* might be in the order (10^4-10^6) which motivates the need for a way to get around this obstacle and render the algorithm feasible even for huge response vectors.

Mathematically, the pseudo response is just a random linear combination of the response components $R_i^{pseudo} = w^T y(x_i)$ where *w* is the weighting vector. This can be analogous to what is done in the input perturbation process since a random input perturbation reflects a movement in random directions in the input space, in the adjoint world a similar trend is to randomly perturb the response vector which can be accomplished via a random linear combination of the response vector.

In [73] the authors showed that one can extract the active subspace using the sensitivity profile of the pseudo response w.r.t. the input parameters. The procedure goes as follows:

Inputs: $x_{ref} \in \mathbb{R}^n$ is the reference input vector (i.e., cross sections).

δx is the relative perturbation from the reference value.

www.manaraa.com

$f:\mathbb{R}^n \to \mathbb{R}^m$ is the forward model of interest.

$f^{adj}:\mathbb{R}^n \to \mathbb{R}^m$ is the adjoint model (needed to compute the sensitivities).

1. Set $\mathcal{X}=\left\{x: x\in\mathbb{R}^n; x_{ref}\left(1-\delta x\right)\le x\le x_{ref}\left(1+\delta x\right)\right\}$ is an *n*-dimensional hyperrectangle.
2. Generate k random realization $\{x_i\}_{i=1}^{k}; x_i\in\mathcal{X}\sim[x_{ref,j}-\delta x, x_{ref,j}+\delta x]^n$.
3. Initialize: $\mathbf{J}=[]$.
4. *for* i = 1 to k
5. $y_i \leftarrow f\left(x_i\right)$
6. $R_i^{pseudo}\leftarrow w^T y_i$, where *w* are some random weights.
7. $j\left(x_i\right)\leftarrow\left(\nabla R_i^{pseudo}\right)^T$ [using the adjoint model].
8. $\mathbf{J}\leftarrow[\mathbf{J}, j\left(x_i\right)]$.
9. $\left[\mathbf{U}_x,\sum_x,\mathbf{V}_x\right]\leftarrow svd\left(\mathbf{J}\right)$.
10. $\mathbf{E}=\left\|\dfrac{f\left(\mathbf{X}_{test}\right)-f\left(\mathbf{U}_x\left(:,1:i\right)\mathbf{U}_x^T\left(:,1:i\right)\mathbf{X}_{test}\right)}{f\left(\mathbf{X}_{test}\right)}\right\|$.
11. $\varepsilon_b\leftarrow$ Construct an error bound as shown in section (4.3.4).
12. *If* $\varepsilon_b\le\varepsilon_{user}$
13. $r_x\leftarrow i$.
14. $\mathbf{U}_x^{(r)}=\mathbf{U}_x\left(:,1:i\right)$.
15. Return

www.manaraa.com

16. end if

17. end for

18. $r_x = k, \mathbf{U}_x^{(r)} = \mathbf{U}_x$ (no reduction occurred).

If no reduction occurred within the first k runs, k is gradually increased until either the error criterion is satisfied or k reaches n which states that the model is non-reducable. Fig. 3-1. illustrates the procedure of active parameter subspace identification.

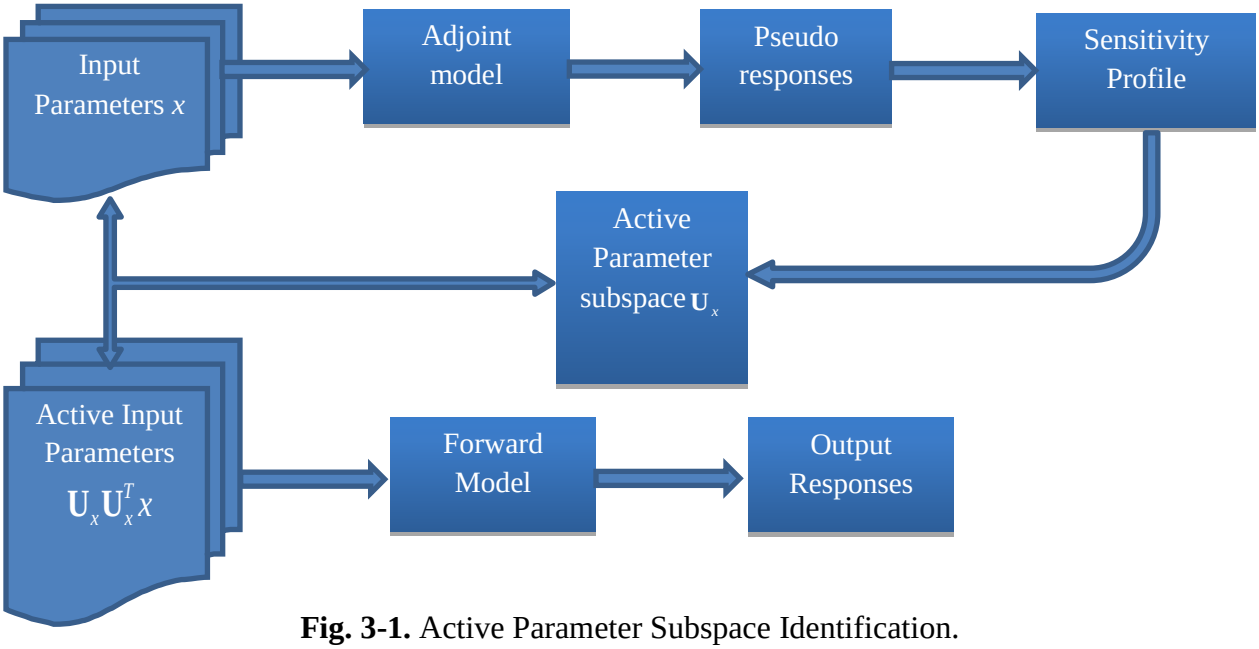

Fig. 3-1. Active Parameter Subspace Identification.

Notice that discarding components in the parameter space will give rise to errors in the response space even if no reduction in the response space is rendered. Estimating the total response error resulting from reduction at each or both parameter and response levels will be discussed in the next chapter.

www.manaraa.com

The proposed error bound is based on a theorem developed in the statistical and applied mathematical communities [75, 76]; they are introduced below for the sake of a complete discussion. The interested readers may consult the cited references for more details.

3.3.3 Active Response Subspace Identification Algorithm (ARSIA):

Unlike the algorithm in the previous subsection this algorithm extracts the active subspace of the response of interest and reduces the dimensionality using forward model snapshots without the need to calculate derivatives (gradient-free). Consider the reducible model under inspection to be described by the model $y = f(x)$; the algorithm proceeds as follows:

Inputs: $x_{ref} \in \mathbb{R}^n$ is the reference input vector (i.e., cross sections).

δx is the relative perturbation from the reference value.

$f : \mathbb{R}^n \to \mathbb{R}^m$ is the forward model of interest

1. Set $\mathcal{X} = \{x : x \in \mathbb{R}^n; x_{ref}(1-\delta x) \le x \le x_{ref}(1+\delta x)\}$ is an n-dimensional hyperrectangle.
2. Set $\mathcal{Y} = \{y : y = f(x) \in \mathbb{R}^m; y_l \le y \le y_u\}$ is an m-dimensional hyperrectangle.
3. Generate k random realization $\{x_i\}_{i=1}^k; x_i \in \mathcal{X} \sim [x_{ref,j} - \delta x, x_{ref,j} + \delta x]^n$.
4. Initialize: $\mathbf{Y} = []$.
5. *for* j = 1 to k
6. $y_j \leftarrow f(x_j)$
7. $\mathbf{Y} \leftarrow [\mathbf{Y}, f(x_j)]$.

www.manaraa.com

8. $\left[\mathbf{U}_y, \Sigma_y, \mathbf{V}_y\right] \leftarrow svd\left(\mathbf{Y}\right)$.

9. $\mathbf{E} = \mathbf{Y} - \mathbf{U}_y\left(:,1:j\right)\mathbf{U}_y^T\left(:,1:j\right)\mathbf{Y}$.

10. $err_i = \left\| \frac{\mathbf{Y}\left(i,:\right) - \mathbf{U}_y^{(r)}\left(i,1:j\right)\mathbf{U}_y^{(r)T}\left(i,1:j\right)\mathbf{Y}\left(i,:\right)}{\mathbf{Y}\left(i,:\right)} \right\|; i = 1,\cdots m$

11. $\varepsilon_b^y \leftarrow$ Construct an error bound as will be shown in chapter 4.

12. *If* $\varepsilon_b^y \le \varepsilon_{user}$

13. $r_y \leftarrow j$.

14. $\mathbf{U}_y^{(r)} = \mathbf{U}_y\left(:,1:j\right)$.

15. Return

16. end if

17. end for

18. $r_y = k, \mathbf{U}_y^{(r)} = \mathbf{U}_y$ (no reduction occurred).

Note that selecting the dimensionality of the reduced space for the responses to be r_y, such that $r_y \le \min\left(m,k\right)$ implies that the active subspace is identified as the range of the first r_y columns of the matrix $\mathbf{U}_y$, denoted by $\mathbf{U}_y^{(r)}$ .The figure below shows a schematic layout of the Gradient-free algorithm.

www.manaraa.com

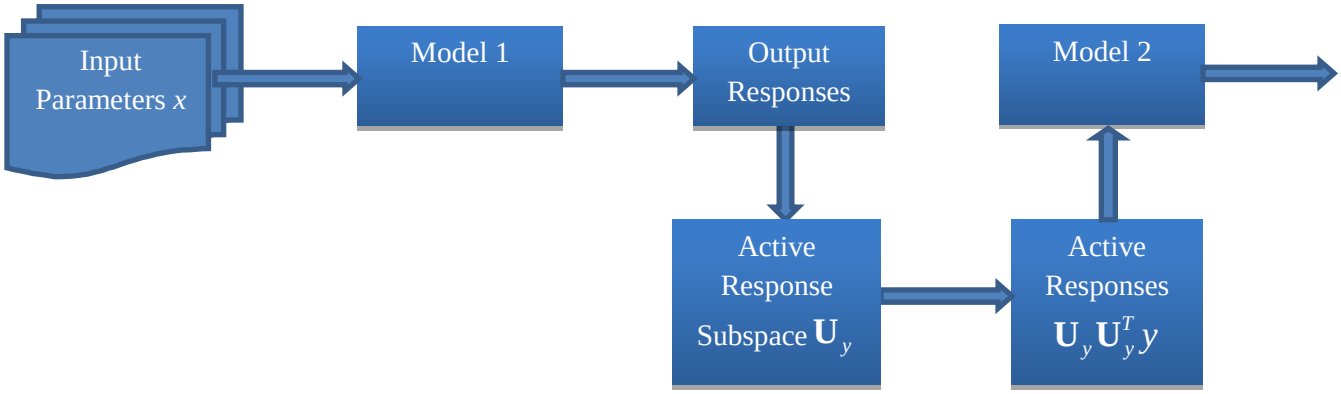

Fig. 3-2. Active Response Subspace Identification

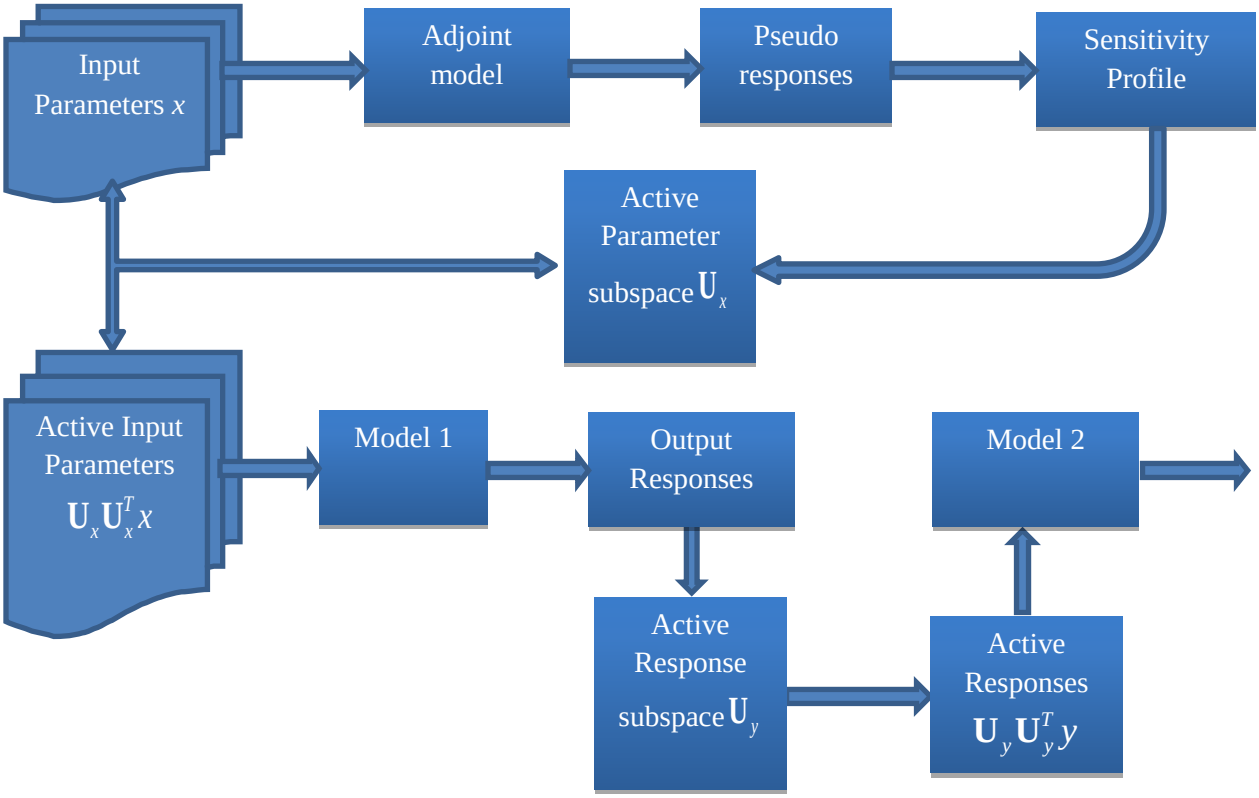

Fig. 3-3. Active Parameter and response Subspaces Identification.

www.manaraa.com

CHAPTER FOUR

PROBABILISTIC ERROR BOUNDS

4.1 Introduction

It is mandatory to equip ROM techniques with an error analysis tool to credibly defend the predictions of the reduced model. This tool enables the user to decide if she needs to increase the size of the active subspace to suit the application of the reduced model over the range of operational conditions of interest. Our goal is to derive a general error analysis for a general multi-physics model. To this end, we first develop the error analysis for a single physics model due to a single reduction at a single interface, e.g., parameter space, response space, etc., followed by an error analysis for a single physics model at two interfaces, e.g., reduction in both parameter and response spaces. Finally, we extend the analysis to cover multiple interfaces for various physics models.

The backbone of the error analysis is Dixon's theory [1983] which will be explained in details in the next section just after discussing the literature review of related work. The direct application of this theory typically results in a very conservative error bound; methods to relax this level of conservatism is discussed in the following subsection. The third subsection describes the quantification of reduction errors at multiple interfaces under a single and multi-physics settings.

www.manaraa.com

4.2 Literature Review

Although a great deal of research has been invested in the development of error bounds, for realistic models, these bounds tend to be extremely conservative which diminishes the utility of the reduced model, and makes its construction computationally taxing. This section provides a short overview of the state-of-the-art methods used to quantify reduction errors and highlight some of their challenges.

The most notable work on error quantification resulting from reduction has been done in the POD community. Scientists have invested in different POD error estimation techniques, few of them have even performed nonlinear enhancements by hybridizing with the Discrete Empirical Interpolation Method (DEIM). A quick overview about the POD error estimation will be conducted followed by introducing the Small-Sample Statistical Estimation method which will be compared against the proposed binomial estimator. Rathinam and Petzold provided a priori error bound for POD reduced-order model and studied the effect of small perturbations on the active subspaces. Petzold, Homescu, and Serban combined error estimation using adjoint methods with small sample statistical condition estimation to construct error bounds for POD. Kunisch and Volkwein (2001) developed priori error estimates for Galerkin POD for parabolic PDE's. Haasdonk and Ohlberger (2005) developed a posteriori error estimate for the state, and response variables, More publications on POD and POD error estimates can be found in [77-88].

Next the most intuitive error analysis tool is that for the POD methods, since an analytically proved expression is provided. Next, a quick overview of the POD method and the corresponding error analysis is provided, followed by the difference between this approach and the probabilistic error bound presented in this work.

www.manaraa.com

Consider a physics model: $y = f(x); x \in \mathbb{R}^n, y \in \mathbb{R}^m$ and assume that the active parameter subspace $\mathcal{X} = span\left\{ \left.\frac{\partial R^{pseudo}}{\partial x}\right|_{x_1}, \cdots, \left.\frac{\partial R^{pseudo}}{\partial x}\right|_{x_{r_x}} \right\}$ with $\dim \mathcal{X} = r_x \le n$, and the active response subspace $\mathcal{Y} = span\{y_1, \ldots, y_{r_y}\} \subset \mathbb{R}^m$ with $\dim \mathcal{Y} = r_y \le m$, $\mathbf{P}_x = \mathbf{U}_x^{(r)}\mathbf{U}_x^{(r)T}, \mathbf{P}_y = \mathbf{U}_y^{(r)}\mathbf{U}_y^{(r)T}$ are projector operators onto the active parameter and response subspaces respectively, and $\mathbf{U}_x^{(r)} \in \mathbb{R}^{n \times r_x}, \mathbf{U}_y^{(r)} \in \mathbb{R}^{m \times r_y}$ are the matrices containing the orthonormal columns of each subspace. Then the error in parameters due to parameter reduction and the error in response due to response reduction can be computed respectively as follows in 4.1 and 4.2:

$$e_x = \sum_{i=1}^{k} \left\| x_i - \sum_{j=1}^{r_x} \left(x_i^T u_{x,j} \right) u_{x,j} \right\|^2 = \sum_{i=r_x+1}^{k} \lambda_{x,i} \tag{4.1}$$

Where $u_{x,j}$ is the j^{th} column of $\mathbf{U}_x^{(r)}$ (i.e., the j^{th} basis of the spanning set of the parameter active subspace) and $\lambda_{x,i} = \sigma_{x,i}^2$ is the i^{th} POD eigenvalue (the square of the i^{th} singular value of the sensitivity matrix **G**). Similarly, the error in response will have the form:

$$e_y = \sum_{i=1}^{k} \left\| y_i - \sum_{j=1}^{r_x} \left(y_i^T u_{y,j} \right) u_{y,j} \right\|^2 = \sum_{i=r_y+1}^{k} \lambda_{y,i} \tag{4.2}$$

Again, $u_{y,j}$ is the j^{th} column of $\mathbf{U}_y^{(r)}$ (i.e., the j^{th} basis of the spanning set of the parameter active subspace) and $\lambda_{y,i} = \sigma_{y,i}^2$ is the i^{th} POD eigenvalue (the square of the i^{th} singular value of the aggregated responses matrix **Y**).

www.manaraa.com

The previous error metrics enable the analyst to compute the errors at an interface due to a reduction at that same interface (i.e., error in *x* due to a reduction in *x* or error in *y* due to reduction in *y*), but what if she needed to compute the error in response due to a reduction in parameters?

Furthermore, the previous metrics do not say anything about future runs, and hence, if the input parameters are perturbed, then the error must be recomputed. We need to find an error bound that guarantees that if *x* is perturbed within the same density function, the error due to the projection will not exceed the predicted bound. This motivates the probabilistic framework discussed in section 4.2.3.

The previous two questions prompted the construction of error metrics and bounds which will be discussing in the following subsection.

4.2.1 Subspace Containment:

One intuitive metric for error estimation is the subspace containment measure which was introduced by Sastry and Varaiya in 1981, analyzed in [94], then used later by Russi 2010 [54] on interesting engineering examples. Suppose $\mathcal{X}_{\mathcal{A}}$ is the subspace spanning parameter space $\mathbb{R}^n$, where $\mathcal{X}_{\mathcal{A}}^{(r)}$ is the reduced subspace capturing all influential directions in the sense that variations in these directions will lead to a significant impact on responses of interest. The measure of containment is then defined as:

$$m\left(\mathcal{X}_{\mathcal{A}}^{(r)}, \mathcal{X}_{\mathcal{A}}\right) := \left\| \left(\mathbf{I} - \mathbf{U}_x \mathbf{U}_x^T\right) \mathbf{U}_x^{(r)} \right\| \tag{4.3}$$

www.manaraa.com

where $\mathbf{U}_x$ contains the orthonormal columns spanning $\mathcal{X}_{\mathcal{A}}$, while $\mathbf{U}_x^{(r)}$ aggregates the orthonormal columns forming the basis for the reduced active subspace $\mathcal{X}_{\mathcal{A}}^{(r)}$. This measure is bounded below by 0 revealing that the whole $\mathcal{X}_{\mathcal{A}}^{(r)} \subset \mathcal{X}_{\mathcal{A}}$ and bounded above by 1 reflecting that $\mathbf{U}_x^{(r)}$ contains vectors that are perpendicular to $\mathcal{X}_{\mathcal{A}}$.

The former metric gains its usefulness from its ability to compare subspaces and to reflect how much information in the first subspace is not contained in the second one.

4.2.2 Angle between Subspaces:

Another natural metric is to compute the angle between subspaces which can easily be computed from:

$$\sin\theta_{\mathcal{X}_{\mathcal{A}},\mathcal{X}_{\mathcal{A}}^{(r)}} = \left\| \mathbf{U}_x \mathbf{U}_x^T - \mathbf{U}_x^{(r)} \mathbf{U}_x^{(r)T} \right\| \tag{4.4}$$

This is upper bounded by Holodnak, Ipsen and Smith in 2015 with a high probability as follows:

$$\mathbb{P}\left\{ \sin\theta_{\mathcal{X}_{\mathcal{A}},\mathcal{X}_{\mathcal{A}}^{(r)}} = \left\| \mathbf{U}_x \mathbf{U}_x^T - \mathbf{U}_x^{(r)} \mathbf{U}_x^{(r)T} \right\| \le \frac{4}{\delta} \frac{\lambda_1 \varepsilon}{\lambda_{r_x} - \lambda_{r_x+1}} \right\} \ge 1 - p_f \tag{4.5}$$

where $\lambda_1 \cdots \lambda_{r_x+1}$ are the first r_x+1 singular values of exact covariance matrix $\mathbf{C}$: $\mathbf{C} = \int_{\mathbb{R}^n} \nabla f(x) \left(\nabla f(x)\right)^T \rho(x)\, dx = \mathbf{U}_x \Sigma_x \mathbf{U}_x^T$ with $\rho(x)$ being the probability distribution function of x, and assuming a big gap ε occurring at the cutoff location (intrinsic dimensionality r_x) such that $0 < \varepsilon = \frac{\lambda_{r_x} - \lambda_{r_x+1}}{4\lambda_1} \le 1$ and δ is a user-defined failure probability, provided that enough

www.manaraa.com

samples are drawn to reach that probability. For more details about the sufficient number of samples, proof, and algorithm, the reader may consult [95].

The former two metrics gain their usefulness from the providing a methodology to distinguish between different subspaces and pick the most informative subspace in the sense that they share most important directions. This angle between subspaces will serve as a basis to justify picking some low-fidelity models and use them to extract subspaces spanning parameter spaces of another high fidelity model, this method, known as M_LROM will be discussed in chapter 5.

While mathematically sound, these metrics suffer from three challenges. First, they require knowledge of the exact subspace, to be further reduced by ROM techniques, which is not always possible, especially when the exact subspace requires many code executions involving high fidelity computationally taxing models. Second, errors, as measured in terms of projection operators or angles between subspaces, do not directly correlate with responses of interest which represent the object of the reduction. Third, these metrics do not provide prior error bounds, meaning that they do not guarantee the reduction error for other model executions that were not used to render the reduction. For these reasons, other methods that provide probabilistic error bounds are discussed next.

4.2.3 Small-Sample Statistical Estimation [1994]:

The idea of Small-Sample norm estimation presented by Kenny and Laub aimed to accurately gauge general functions sensitivities by computing the effect of random perturbations at the points of function evaluations. The fact that it is a transpose-free method motivated its use in various problems in contrast to the commonly used yet limited power method since the latter

www.manaraa.com

requires the access to the implicit Fréchet derivatives. This flexibility enabled the Small-Sample Statistical condition Estimation to be used with mappings between different dimensions providing the ability to construct component-wise estimates as well. Several estimators were presented, and the probability that these estimators would lie within a factor $\eta > 1$ from the actual norm was analytically computed with deep roots in Dixon's theory that will be discussed in the next section. In this section two of these estimators are illustrated, the averaged statistical estimator and the subspace statistical estimator as well as the associated probabilities which will be compared to the proposed probabilistic bound.

Let $x \in \mathbb{R}^n$ be the input parameter for a nonlinear vector valued function $f : \mathbb{R}^n \mapsto \mathbb{R}^m$ and let $\mathbf{E} \in \mathbb{R}^{m \times N}$ be the error matrix due to active subspace reduction such that each row of $\mathbf{E}$ demonstrates the error in a single response of the m responses where each column represents a single run from the N random runs such that: $\mathbf{E} = \left\| \dfrac{f(\mathbf{X}) - \mathbf{U}_y^{(r)} \mathbf{U}_y^{(r)T} f\left(\mathbf{U}_x^{(r)} \mathbf{U}_x^{(r)T} \mathbf{X}\right)}{f(\mathbf{X})} \right\|$ and $\mathbf{X} \in \mathbb{R}^{m \times N}$ are the N random input parameters used to estimate the error norm. And hence $e_j \in \mathbb{R}^{1 \times N}$ is the j^{th} row of $\mathbf{E}$ (i.e., the error in the j^{th} response). Next let $w \in \mathbb{R}^N$ be *iid* sampled from a known distribution $w \sim \mathcal{D}$. And with s being a positive integer representing the number of w vectors used, then the probabilistic statement sought will look like:

$$\mathbb{P}\left\{ \frac{\|e_j\|}{\eta} \le estimator(s) \le \eta \|e_j\| \right\} \ge 1 - p_f(\eta, \mathcal{D}, s) \tag{4.6}$$

4.2.3.1 Averaged Statistical Estimator $\zeta(s)$:

www.manaraa.com

In this method the $w_i's \sim \left[\mathcal{N}(0,1)\right]^N; i=1,2,...,s$ over the unit hypersphere S_{N-1} as shown in details in Dixon's theory discussion, in this case, the estimator is:

$$\zeta(s) = \frac{\left|e_j w^{(1)}\right| + \left|e_j w^{(2)}\right| + \cdots + \left|e_j w^{(s)}\right|}{sE_n} \tag{4.7}$$

where E_n is computed from:

$$E_n = \begin{cases} 1 & n=1 \\ 2/\pi & n=2 \\ \dfrac{1.3.5...(n-2)}{2.4.6...(n-1)} & n \text{ is odd}>2 \\ \dfrac{2}{\pi}\dfrac{2.4.6...(n-2)}{1.3.5...(n-1)} & n \text{ is even}>2 \end{cases} \tag{4.8}$$

and with few manipulations with the probability distribution function that can be found in [96-96], the probabilistic statement can be written as follows:

$$\mathbb{P}\left\{\frac{\|e_j\|}{\eta} \le \zeta(s) \le \eta\|e_j\|\right\} \ge 1 - \frac{1}{s!}\left(\frac{2s}{\pi\eta}\right)^s + O\left(\frac{1}{\eta^{s+1}}\right); \eta \ge \max\left\{1, \frac{2s}{\pi}(s!)^{\frac{-1}{s}}\right\} \tag{4.9}$$

4.2.3.2 Subspace Statistical Estimator $\nu(s)$:

The only difference here is that the *s* random vectors (i.e., *w*'s) are orthogonalized via Gram-Schmidt, QR decomposition or SVD decomposition to construct an orthonormal basis for an *s*-dimensional subspace that has been randomly selected from all the *s*-dimensional subspaces from $\mathbb{R}^N$. Then the subspace estimator is taken to be directly proportional to the norm of the projection of vector under inspection (i.e., e_j) onto the span of *w*'s such that:

www.manaraa.com

$$\nu(s)=\frac{E_s}{E_N}\sqrt{\left|e_j w^{(1)}\right|^2+\left|e_j w^{(2)}\right|^2+\cdots\left|e_j w^{(s)}\right|^2} \tag{4.10}$$

and hence, the probabilistic statement can be recast as:

$$\mathbb{P}\left\{\frac{\|e_j\|}{\eta}\le\nu(s)\le\eta\|e_j\|\right\}=g_{N,s}\left(\frac{\eta E_N}{E_s}\right)-g_{N,s}\left(\frac{E_N}{\eta E_s}\right); \tag{4.11}$$

where

$$g_{N,s}(\varepsilon)=\begin{cases}0 & \text{for } \varepsilon\le 0\\ 1 & \text{for } \varepsilon\ge 1\\ \varepsilon\left(1+\frac{1}{2}\left(1-\varepsilon^2\right)+\frac{1.3}{2.4}\left(1-\varepsilon^2\right)^2+\cdots+\frac{(N-4)!!}{(N-3)!!}\left(1-\varepsilon^2\right)^{(N-3)/2}\right) & \text{for } s=1,\ odd\ N\\ \frac{2}{\pi}\varepsilon\left(\frac{\sin^{-1}(\varepsilon)}{\varepsilon}+\left(1-\varepsilon^2\right)+\frac{2}{3}\left(1-\varepsilon^2\right)^2+\cdots+\frac{(N-4)!!}{(N-3)!!}\left(1-\varepsilon^2\right)^{(N-3)/2}\right) & \text{for } s=1,\ even\ N\\ 1-\left(1-\varepsilon^2\right)^{(N-2)/2} & \text{for } s=2,\\ g_{N,s-2}(\varepsilon)-\frac{(N-2)!!\varepsilon^{s-2}}{(s-2)!!(N-s)!!}\left(1-\varepsilon^2\right)^{(N-s)/2} & \text{for } even\ s>2,\\ g_{N,s-2}(\varepsilon)-\frac{(N-1)!!\ \mathrm{E}_N\,\varepsilon^{s-2}}{(s-2)!!(N-s)!!}\left(1-\varepsilon^2\right)^{(N-s)/2} & \text{for } odd\ s>2,\end{cases}$$

(4.12)

where the double factorial symbol (!!) is the skip factorial (i.e., $n!!=n(n-2)(n-4)\cdots n_0$; and $n_0=1$ if n is odd and 2 if n is even). For more details about these methods, the reader may consult the formerly mentioned references [96-97]. The difference between the Small-Sample Statistical Estimation and the proposed methodology can be summarized as:

www.manaraa.com

- w is sampled from a binomial distribution with a user-specified probability of failure.
- The multiplier (factor) η is computed numerically for a given probability (R.H.S).
- The estimator $b(s) = \max_{i=1,2,\cdots s} \left| e_j w^{(i)} \right|$. And hence the probabilistic statement can be written as:

$$\mathbb{P}\left\{ \left\| e_j \right\| \le \eta b(s) \right\} \ge 1 - \left[p_f \right]^s \tag{4.13}$$

Before discussing more details about this probabilistic norm estimator, the root of all these theories namely Dixon's theory is to be discussed.

4.3 Supporting Theories

4.3.1 Dixon's Theory [1983]:

Probabilistic error bounds were first introduced by Dixon (1983) when he estimated the largest (and/or the smallest) eigenvalue and hence the condition number of a real positive definite matrix **A** [75, 76]. His theory can be regarded as the cornerstone of probabilistic error bounds framework. This theory finds an estimate for the upper bound of the 2-norm of a matrix by multiplying it with few random vectors sampled from a known distribution. The probability of the actual norm being less than the estimated upper bound depends on the distribution from which the random vectors are sampled. Several attempts to make use and develop this theory can be found in [89-93]. These methods need a solid background in linear algebra and numerical methods, the reader may consult [94-100] for refreshing these topics. To get a better grip on this theory and hence make the required modification to render our bound more realistic, the original theory will be explored.

www.manaraa.com

Lemma. Let $z=\left[z_1 z_2 \cdots z_N\right]^T$; $N \geq 2$, and z_i's are $iid \sim \mathcal{N}(0,1)$ one can show that:

$$\Rightarrow \frac{z_i}{\|z\|} \sim \mathcal{U}(-1,1) \tag{4.14}$$

$$\Rightarrow \frac{z_i^2}{\|z\|^2} \sim \beta\left(\frac{1}{2}, \frac{N-1}{2}\right) \tag{4.15}$$

The previous lemma assures that if the individual components of a vector are sampled from a normal distribution, then the normalized version of this vector is distributed over a unit hypersphere whereas squaring each component makes the probability distribution a Beta function. This is necessary for the following theorem.

Theorem. Let $\mathbf{A} \in \mathbb{R}^{N \times N}$ be a real positive definite matrix whose eigenvalues are $\lambda_1 \geq \lambda_2 \geq \ldots \geq \lambda_N > 0.$

Let S:=$\left\{w \in \mathbb{R}^N \mid w^T w = 1\right\}$ be a unit hypersphere such that $N \geq 2$ and $w_i \sim \mathcal{U}(0,1)$ over *S*. And if $\theta \in \mathbb{R}$>1 *then*:

$$\mathbb{P}\left\{w^T \mathbf{A} w \leq \lambda_1 \leq \theta w^T \mathbf{A} w\right\} \geq 1 - \sqrt{\frac{2}{\pi}} \sqrt{\frac{N}{\theta}}. \tag{4.16}$$

Proof. Since $\mathbf{A}$ is a real positive definite matrix, one can write that:

$$\mathbf{A} = \mathbf{U}\mathbf{D}\mathbf{U}^T,$$

where $\mathbf{U}$ is orthogonal, and $\mathbf{D} = diag\left(\lambda_1 \cdots \lambda_N\right)$. Let us expand w using the same orthonormal basis:

www.manaraa.com

$$w = \sum_{i=1}^{n} \tilde{w}_i u_i = \mathbf{U}\tilde{w}.$$

Then:

$$w^T \mathbf{A} w = \tilde{w}^T \underbrace{\mathbf{U}^T \mathbf{U}}_{\mathbf{I}} \mathbf{D} \underbrace{\mathbf{U}^T \mathbf{U}}_{\mathbf{I}} \tilde{w} = \tilde{w}^T \mathbf{D} \tilde{w} = \lambda_1 \tilde{w}_1^2 + \cdots + \lambda_N \tilde{w}_N^2$$
$$\leq \lambda_1 \underbrace{\left(\tilde{w}_1^2 + \cdots + \tilde{w}_N^2 \right)}_{\|\tilde{w}\|^2 = 1} = \lambda_1$$

So far we have proved the first inequality $w^T \mathbf{A} w \leq \lambda_1$..Next, we prove that $\lambda_1 \leq \theta w^T \mathbf{A} w$ or more precisely find the probability of this event being true since there are cases when this fails.

$$\lambda_1 \leq \theta w^T \mathbf{A} w = \theta \left(\lambda_1 \tilde{w}_1^2 + \cdots + \lambda_N \tilde{w}_N^2 \right)$$

This definitely occurs when $\theta \tilde{w}_1^2 \geq 1$

$$\mathbb{P}\left\{ \theta \tilde{w}_1^2 \geq 1 \right\} = \mathbb{P}\left\{ \tilde{w}_1^2 \geq \frac{1}{\theta} \right\} = 1 - \mathbb{P}\left\{ \tilde{w}_1^2 \leq \frac{1}{\theta} \right\}$$

$$\mathbb{P}\left\{ \tilde{w}_1^2 \leq \frac{1}{\theta} \right\} = \int_0^{\frac{1}{\theta}} f_{\tilde{w}_1^2}(t)\, dt;$$

where $f_{\tilde{w}_1^2}(t)$ is the probability density function of $\tilde{w}_1^2$ which is *iid* and $\sim \mathcal{N}(0,1)$ over *S*(normalized to $\|*\| = 1$). From lemma we know that:

$$f_{\tilde{w}_1^2}(t) = \beta\left(\frac{1}{2}, \frac{N-1}{2} \right) = a_N t^{\frac{-1}{2}} (1-t)^{\frac{N-3}{2}};\ 0 \leq t \leq 1$$

www.manaraa.com

where a_N is the normalization constant; $a_N = \dfrac{\Gamma\left(\frac{N}{2}\right)}{\Gamma\left(\frac{1}{2}\right)\Gamma\left(\frac{N-1}{2}\right)} \le \sqrt{\dfrac{N}{2\pi}}$

$$\mathbb{P}\left\{\tilde{w}_1^2 \le \frac{1}{\theta}\right\} = \int_0^{\frac{1}{\theta}} a_N t^{\frac{-1}{2}} (1-t)^{\frac{N-3}{2}} dt \tag{4.17}$$

This integral can be analytically evaluated, but Dixon has chosen to find an upper-bound instead, which is larger than the actual probability.

$$\mathbb{P}\left\{\tilde{w}_1^2 \le \frac{1}{\theta}\right\} = \int_0^{\frac{1}{\theta}} a_N t^{\frac{-1}{2}} (1-t)^{\frac{N-3}{2}} dt \le \frac{2a_N}{\sqrt{\theta}} \le \sqrt{\frac{2}{\pi}}\sqrt{\frac{N}{\theta}} \tag{4.18}$$

which means:

$$\mathbb{P}\left\{w^T \mathbf{A} w \le \lambda_1 \le \theta w^T \mathbf{A} w\right\} \ge 1 - \sqrt{\frac{2}{\pi}}\sqrt{\frac{N}{\theta}} \tag{4.19}$$

Corollary. If $\mathbf{B} \in \mathbb{R}^{m \times N}$ is a real matrix such that $\mathbf{A} = \mathbf{L}\mathbf{L}^T = \mathbf{B}^T\mathbf{B}$ where $\mathbf{L} = \mathbf{B}^T$ is the Cholesky factor of $\mathbf{A}$ and if $\sigma_1 \ge \cdots \ge \sigma_N > 0$ are the singular values of $\mathbf{B}$ (i.e. $\lambda_i = \sigma_i^2$), then the previous theorem can be written as:

$$\mathbb{P}\left\{\|\mathbf{B}w\| \le \left(\sigma_1 = \|\mathbf{B}\|\right) \le \sqrt{\theta}\,\|\mathbf{B}w\|\right\} \ge 1 - \sqrt{\frac{2}{\pi}}\sqrt{\frac{N}{\theta}} \tag{4.20}$$

Selecting $\theta = \left\lceil \alpha^2 \left(\frac{2}{\pi}\right) N \right\rceil$ where α>1 yields:

$$\mathbb{P}\left\{\|\mathbf{B}\| \le \alpha\sqrt{\frac{2}{\pi}}\sqrt{N}\,\|\mathbf{B}w\|\right\} \ge 1 - \alpha^{-1} \tag{4.21}$$

www.manaraa.com

4.3.1.1 Finding the Exact Probability for Rank-one Matrices:

Note that the singular values being positive is an explicit condition mentioned in Dixon's proof, yet it is important to test the performance of the theory for numerically singular matrices especially since it is most likely to be used to estimate the 2-norm of error matrices. To answer such a question let us give the proof a geometric nature and explore how a matrix with few significant singular values will behave. Let us write **B** as the sum of outer products:

$$\mathbf{B} = \sum_{i=1}^{r \le \min\{m,N\}} \sigma_i u_i v_i^T$$

where r is the intrinsic rank of **B**; σ_i is the i^{th} singular value of **B**, u_i and v_i are the i^{th} left and right singular vectors respectively. Then:

$$\mathbf{B}w = \sum_{i=1}^{r \le \min\{m,N\}} \sigma_i u_i \left(v_i^T w\right)$$

But $\left(v_i^T w\right)$ is the component of w in the direction $v_i \left(i.e.\ \tilde{w}_i\right)$ which is the cosine of the angle between w and v_i (remember that both w and v_i are unit vectors).

$$\mathbf{B}w = \sum_{i=1}^{r} \sigma_i \cos\left(\theta_i\right) u_i = \sigma_1 \cos\left(\theta_1\right) u_1 + \sigma_2 \cos\left(\theta_2\right) u_2 + \cdots \sigma_r \cos\left(\theta_r\right) u_r$$

and hence:

$$\mathbb{P}\left\{\|\mathbf{B}\|^2 \le \theta \|\mathbf{B}w\|^2\right\} = \mathbb{P}\left\{\sigma_1^2 \le \theta\left(\sigma_1^2 \cos^2(\theta_1) + \sigma_2^2 \cos^2(\theta_2) \cdots\right)\right\} \qquad (4.22)$$

www.manaraa.com

If the first term in the upper bound is greater than σ_i then definitely the bound is satisfied. This means that:

$$\mathbb{P}\left\{\|\mathbf{B}\|^2 \le \theta\|\mathbf{B}w\|^2\right\} = \mathbb{P}\left\{\cos^2(\theta_1) \ge \frac{1}{\theta}\right\} = 1 - \int_0^{\frac{1}{\theta}} f_{\cos^2(\theta_1)}(t)\,dt = 1 - \int_0^{\frac{1}{\theta}} f_{\tilde{x}_1^2}(t)\,dt \qquad (4.23)$$

This is the exact same result from Dixon's proof [75] but looking at it as vector *x* being projected on *v*'s scaled by σ's then rotated to *u*'s directions reveals that the probability predicted by the theory is much less than the actual probability for the following reasons:

1. The actual integral of the complement event is replaced by an upper bound which is larger than the exact integral.
2. The probability is computed based only on the first singular value:

$$\mathbb{P}\left\{\|\mathbf{B}\|^2 \le \theta\|\mathbf{B}w\|^2\right\} = \mathbb{P}\left\{\sigma_1^2 \le \theta\left(\sigma_1^2\cos^2(\theta_1) + \underbrace{\sigma_2^2\cos^2(\theta_2) + \cdots}_{\text{neglected}}\right)\right\} \qquad (4.24)$$

In other words, there are cases where the first term is less than σ_1^2 but the rest of the terms will compensate that. Those cases are not accounted for in the predicted probability. Which is another reason for making the predicted probability less than the actual one and hence the complementary probability greater than the actual one. We will compute the exact integral instead of an upper bound. We can pick **B** to be a rank-one matrix, which is the worst case scenario of singularity and then the bound will only be satisfied if the value of $\cos^2(\theta_1) \ge \frac{1}{\theta}$.

So the final step would be to compute the analytic integral corresponding to this probability:

www.manaraa.com

$$\mathbb{P}\left\{\|\mathbf{B}\| \le \sqrt{\theta}\,\|\mathbf{B}w\|\right\} = 1 - a_n \underbrace{\int_0^{\frac{1}{\theta}} t^{-\frac{1}{2}} (1-t)^{\frac{N-3}{2}}\, dt}_{I_N}$$

$$I_N = \int_0^{\frac{1}{\theta}} t^{-\frac{1}{2}} (1-t)^{\frac{N-3}{2}}\, dt$$

Use the substitution:

$$t = \sin^2(y) \qquad @t = 0 \rightarrow y = 0$$

$$dt = 2\sin(y)\cos(y)\,dy \qquad @t = \frac{1}{\theta} \rightarrow y = \sin^{-1}\left(\frac{1}{\sqrt{\theta}}\right)$$

$$I_N = \int_0^{\sin^{-1}\left(\frac{1}{\theta}\right)} \frac{1}{\cancel{\sin(y)}} \left(\cos^2(y)\right)^{\frac{N-3}{2}} 2\cancel{\sin(y)}\cos(y)\,dy$$

$$= 2\int_0^{\sin^{-1}\left(\frac{1}{\theta}\right)} \left(\cos(y)\right)^{N-2} dy$$

Using integration by parts:

$$I_N = 2\left(\cos^{N-3}(y)\sin(y)\right)\Big|_0^{\sin^{-1}\left(\frac{1}{\sqrt{\theta}}\right)} + 2\int_0^{\sin^{-1}\left(\frac{1}{\sqrt{\theta}}\right)} \overbrace{\sin^2(y)}^{1-\cos^2(y)} \cos^{N-4}(y)\,dy$$

$$I_N = 2\left(\cos\left(\sin^{-1}\left(\frac{1}{\sqrt{\theta}}\right)\right)\right)^{N-3} \frac{1}{\sqrt{\theta}} +$$

$$(N-3) \times \overbrace{2\int_0^{\sin^{-1}\left(\frac{1}{\sqrt{\theta}}\right)} \cos^{N-4}(y)\,dy}^{I_{N-2}} -$$

$$(N-3) \times \underbrace{2\int_0^{\sin^{-1}\left(\frac{1}{\sqrt{\theta}}\right)} \cos^{N-2}(y)\,dy}_{I_N}$$

$$I_N = 2\left(\cos\left(\sin^{-1}\left(\frac{1}{\sqrt{\theta}}\right)\right)\right)^{N-3} \frac{1}{\sqrt{\theta}} + (N-3)I_{N-2} - (N-3)I_N$$

www.manaraa.com

$$I_N = \frac{2\left(\cos\left(\sin^{-1}\left(\frac{1}{\sqrt{\theta}}\right)\right)\right)^{N-3}}{N-2}\frac{1}{\sqrt{\theta}} + \frac{N-3}{N-2}I_{N-2}$$

$$I_N = \frac{2}{N-2}\sqrt{\frac{(\theta-1)^{N-3}}{\theta^{N-2}}} - \frac{N-3}{N-2}I_{N-2};\ N \geq 2 \text{ and } I_1 = 2\sin^{-1}\left(\frac{1}{\sqrt{\theta}}\right);\ I_0 = \frac{2}{\sqrt{\theta}}. \quad (4.25)$$

Finally, if the matrix-vector multiplication was repeated *s* times then the probabilities will be raised to *s* since these are independent events.

$$\mathbb{P}\left\{\|\mathbf{B}\| \leq \sqrt{\theta}\max_{i=1,2,\cdots s}\left\|\mathbf{B}w^{(i)}\right\|\right\} = 1-\left(a_N I_N\right)^s \leq 1-\left(\sqrt{\frac{2}{\pi}}\sqrt{\frac{N}{\theta}}\right)^s \quad (4.26)$$

where $N \geq 2; \theta \geq 1;$ usually $\theta = \alpha^2\left(\frac{2}{\pi}\right)N;\ \alpha = 10$ and:

$$a_N = \frac{\Gamma\left(\frac{N}{2}\right)}{\Gamma\left(\frac{1}{2}\right)\Gamma\left(\frac{N-1}{2}\right)};$$

$$I_N = \frac{2}{N-2}\sqrt{\frac{(\theta-1)^{N-3}}{\theta^{N-2}}} - \frac{N-3}{N-2}I_{N-2} \quad \forall N \geq 2;$$

$$I_1 = \frac{2}{\sqrt{\theta}};\ I_0 = 2\sin^{-1}\left(\frac{1}{\sqrt{\theta}}\right).$$

This analytic integral gives a very close probability to the numerical tests when a rank-one matrix is used because all two sources of inaccuracy are eliminated.

One intuitive question arises here if the error due to a reduction based on a specific dataset is bounded how can we guarantee that this will still hold for different input parameters? To answer this question we need to review the Tensor-free expansion which is needed to prove

www.manaraa.com

that any other input parameter once constrained to the active subspace will produce an error that is necessarily less than the bound.

4.3.2 Tensor-Free Expansion

This expansion [73] is a generalized version of Taylor expansion that theoretically expands any Taylor expandable function in terms of arbitrary once-differentiable scalar functional basis as shown next.

$$R(\bar{x}) = R(\bar{x}_0) + \sum_{i_1=1}^{n_1} \psi_{i_1}\left(\bar{\beta}_{i_1}^{(1)T}\Delta\bar{x}\right) + \sum_{i_1,i_2=1}^{n_2} \psi_{i_1}\left(\bar{\beta}_{i_1}^{(2)T}\Delta\bar{x}\right)\psi_{i_2}\left(\bar{\beta}_{i_2}^{(2)T}\Delta\bar{x}\right) + \sum_{i_1,i_2,i_3=1}^{n_3} \psi_{i_1}\left(\bar{\beta}_{i_1}^{(3)T}\Delta\bar{x}\right)\psi_{i_2}\left(\bar{\beta}_{i_2}^{(3)T}\Delta\bar{x}\right)\psi_{i_3}\left(\bar{\beta}_{i_3}^{(3)T}\Delta\bar{x}\right) + \cdots \tag{4.27}$$

which can be written in a shorter form as:

$$R(\bar{x}) - R(\bar{x}_0) = \sum_{k=1}^{\infty} \sum_{i_1,i_2,\cdots i_k=1}^{n_k} \prod_{j=1}^{k} \psi_{i_j}\left(\bar{\beta}_{i_j}^{(k)T}\Delta\bar{x}\right) \tag{4.28}$$

where $x \in \mathbb{R}^n$ is the parameter vector, β's are the basis vectors and ψ's are the once-differentiable basis functions.

Next, we show that the *m* responses from a nonlinear function $f(x)$ can be constrained to a subspace and hence can be upper-bounded. The individual components of the response vector can be written as:

$$[y]_p = f_p(x), p = 1,2,\cdots m$$

where $[y]_p$ is the p^{th} component of the response vector *y*. Assuming that the functions $f_p(x)$ are integrable everywhere in the parameter space, implying that there exist *m* functions z_p such that:

www.manaraa.com

$$\frac{\partial z_p}{\partial x_q} = [y]_p = f_p(x), p = 1, 2, \cdots m \ \forall l. \tag{4.29}$$

Without loss of generality, we pick $p = q$ and assume that the integrated functions z_p are smooth and can be Taylor expanded and hence can be expanded using the *tensor-free* expansion as follows:

$$z_p(x) = \sum_{k=1}^{\infty} \sum_{i_1, i_2, \cdots i_k = 1}^{n_k} \psi_{1,p}\left(\beta_{1,p}^{(k)T} x\right) .. \ \psi_{1,p}\left(\beta_{l,p}^{(k)T} x\right) .. \ \psi_{k,p}\left(\beta_{k,p}^{(k)T} x\right)$$

whose derivatives with respect to x are given by a vector:

$$\nabla z_p(x) = \sum_{k=1}^{\infty} \sum_{j_1, .. j_l .., j_k = 1}^{n} \psi_{1,p}\left(\beta_{j_1,p}^{(k)T} x\right) .. \psi'_{l,p}\left(\beta_{j_l,p}^{(k)T} x\right) .. \psi_{k,p}\left(\beta_{j_k,p}^{(k)T} x\right) \beta_{j_l,p}^{(k)}$$

This expansion was developed in support of gradient-based reduction algorithm described in section 3.2.2. The previous expression implies that the derivative at any point in the parameter space may be viewed as a linear combination of a number of □ vectors. By randomly sampling the derivatives, one could identify a basis of reduced dimension that approximates the derivatives anywhere in the parameter space, and upper-bound the error resulting from the reduction.

Next form a super vector that aggregates all the derivatives for all the z_q functions as follows:

$$g = \left[\nabla z_1(x)^T \quad .... \quad \nabla z_m(x)^T \right]^T \in \mathbb{R}^{mn \times 1}$$

www.manaraa.com

Since one can find a basis in the parameter space that can upper-bound the construction error for each of the $\nabla z_q(x)$ vectors, one can find another super basis that upper bounds the construction error for the vector g. This was proved in earlier work using the idea of pseudo-response.

Now, design a matrix **K** such that:

$$\mathbf{K} \in \mathbb{R}^{m \times mn} = \left[\mathbf{K}_1 \quad \ldots \quad \mathbf{K}_m\right]$$

where $\mathbf{K}_p$ is the null matrix except the p^{th} diagonal element is given by: $\left[\mathbf{K}_p\right]_{pp} = 1.0$. This matrix is designed to pick the derivative of the function z_p with respect to the p^{th} vector in order to take advantage of Eq. (4.29):

$$\mathbf{K}g = \left[\frac{\partial z_1}{\partial x_1} \quad \ldots \quad \frac{\partial z_m}{\partial x_m}\right]^T = y.$$

This equation implies that given a subspace that constrains the vector *g* with the reduction error-upper-bounded, one can find a subspace for the vector *y*, which also ensures that its associated reduction error is upper-bounded.

4.3.3 Numerical Inspection of Different Distributions used to construct Error Bounds:

The previous discussion gave rise to some important questions such as: what if the singular values of the matrix were close to each other? This means that the other singular values (that were neglected in the analysis) will render the bound much larger than the actual norm which will result in a non-realistic bound that can be orders of magnitudes off the actual norm. It is desirable that the probability of failure is very small and that the multiplier $\sqrt{\theta}$ (we will call it η from now on) is as close to 1 as possible. This means that the preferable distributions are those

www.manaraa.com

that have a small area under the pdf curve from 0 to $1/\eta^2$ then a sharp increase from $1/\eta^2$ to 1. This is exactly the opposite case of both normal and uniform distributions which explains why these distributions result in a conservative error bound. The advantage of the normal distribution is that it allows one to calculate the bound analytically. One however can inspect other forms for the distributions and calculate the bound numerically as shown below [105, 106]:

$$\mathbb{P}\left\{\|\mathbf{B}\| \le \eta \max_{i=1,2,\cdots s} \left\|\mathbf{B}w^{(i)}\right\|\right\} \le 1-\left(\int_0^{1/\eta^2} pdf_{w_1^2}(t)\,dt\right)^s = 1-\left(p_f(\eta,\mathcal{D})\right)^s \tag{4.30}$$

This allows one to compute the multiplier η for a general distribution and a user-defined probability. For illustration we pick s = 1 and probability of failure $p_f(\eta,\mathcal{D}) \le 0.1$ then numerically search for η that makes the actual norm less than the estimated one in 90% of the cases. This is repeated for many distributions and the multiplier η is tabulated in table I. In practice, after deciding which distribution will be used and numerically computing the corresponding multiplier, the random matrix **B** will be replaced by the error matrix **E** which is a problem-dependent error operator.

www.manaraa.com

Figures 4-1 through 4-3 depict the comparison between using the normal, uniform and binomial distributions with a probability of failure $p_f\left(\eta, \mathcal{D}\right) \leq 0.1$.

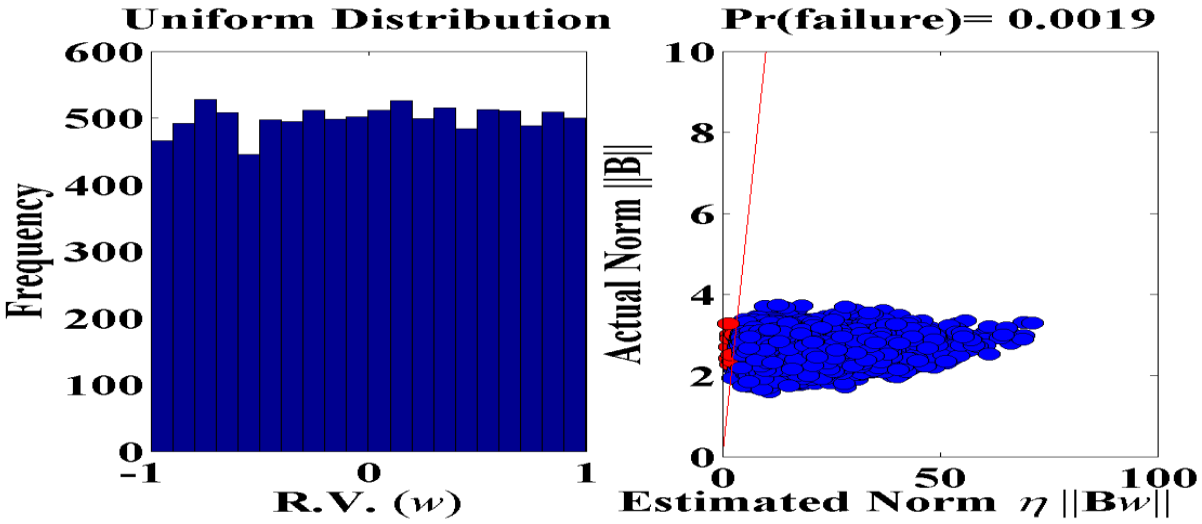

Fig. 4-1. Uniform Distribution.

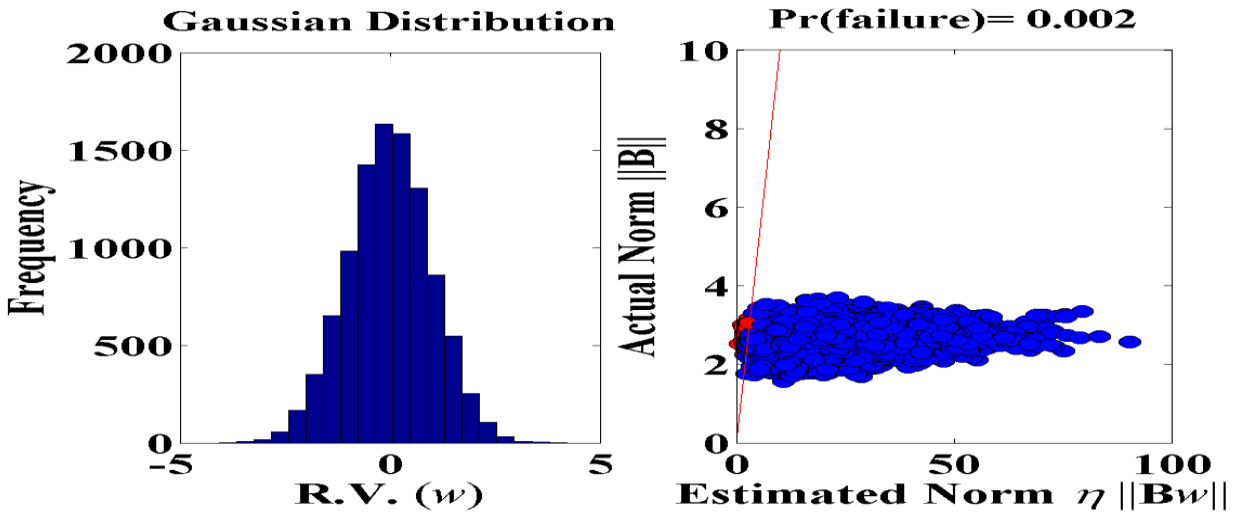

Fig. 4-2. Normal Distribution.

www.manaraa.com

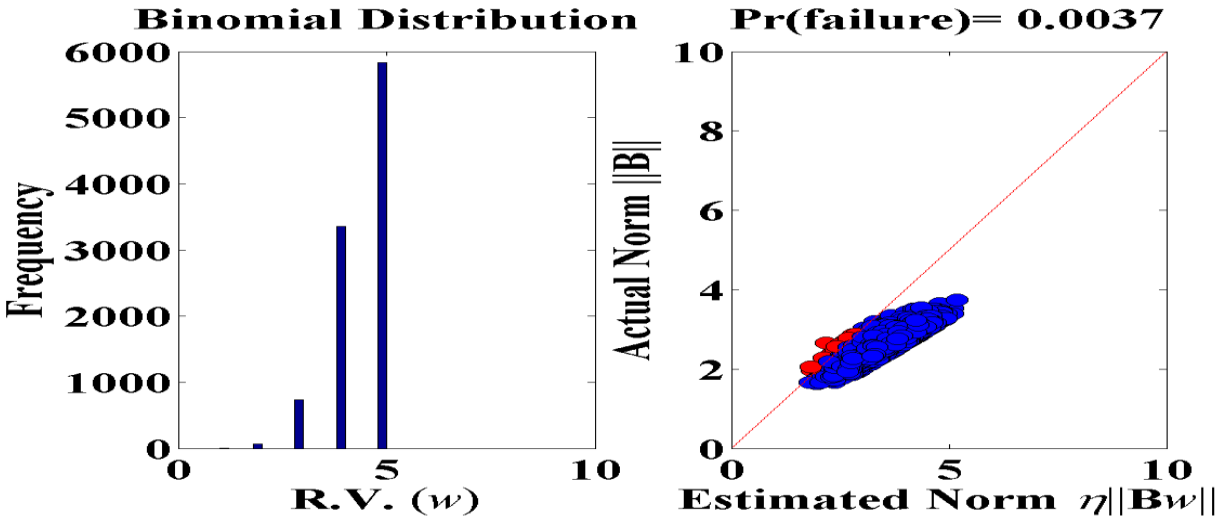

Fig. 4-3. Binomial Distribution

The figures show that fixing the probability of failure gives the least multiplier η when sampling from the binomial distribution. Further, the same distribution results in a linear trend with narrow scatter around the 45-degree solid red line implying that for the failed instances the actual norm will be very close to the estimated one.

4.3.4 Proposed Binomial Estimator *b(s)*:

It is instructive to question why binomial distribution, unlike the normal or uniform distributions as used by Dixon, Kenney, Laub, Gudmundsson, and others, exhibits this appealing behavior in which the estimated bound is very close to the true errors. We shed some light on this question in this section.

It is undeniable that the Gaussian (i.e., normal) distribution is the most widely used distribution in many naturally and man-driven systems and has been well studied and

www.manaraa.com

analytically explored by practitioners and scientists from various backgrounds. In addition, due to the central limit theorem and loosely speaking, the interaction between many distributions in most engineering problems can be well approximated by a Gaussian distribution. Another reason for using a Gaussian is the existence of the lemma discussed in section 4.3.1 which assures that the pdf required to compute an analytic form for the probabilistic statement is known:

$$pdf_{\tilde{w}_1^2}(t) = \beta\left(\frac{1}{2}, \frac{n-1}{2}\right) = t^{-1/2}(1-t)^{(n-3)/2}.$$

To mimic this work for the binomial distribution one needs to look at the distribution of the squared components of unit vectors drawn from a binomial distribution. This is carried out numerically revealing that the resulting distribution is also Gaussian with a mean and standard deviation that depends solely on *N*; the length of the random vector. If one fixes the lower bound of the probability of success $p_s = 1 - \left(\int_0^{1/\eta^2} \frac{1}{\sqrt{2\pi\sigma^2}} e^{\frac{-(t-\mu)^2}{2\sigma^2}} dt \right)$ in case of using a binomial distribution or $p_s = 1 - \left(\int_0^{1/\eta^2} t^{-1/2}(1-t)^{(N-3)/2} dt \right)$ in the case of using a Gaussian distributed random unit vector, it is easy to numerically determine the value of η for each case.

This relation can be explored further by fitting a curve to predict the value of η at any *N*. This can be seen in figure 4-4.

www.manaraa.com

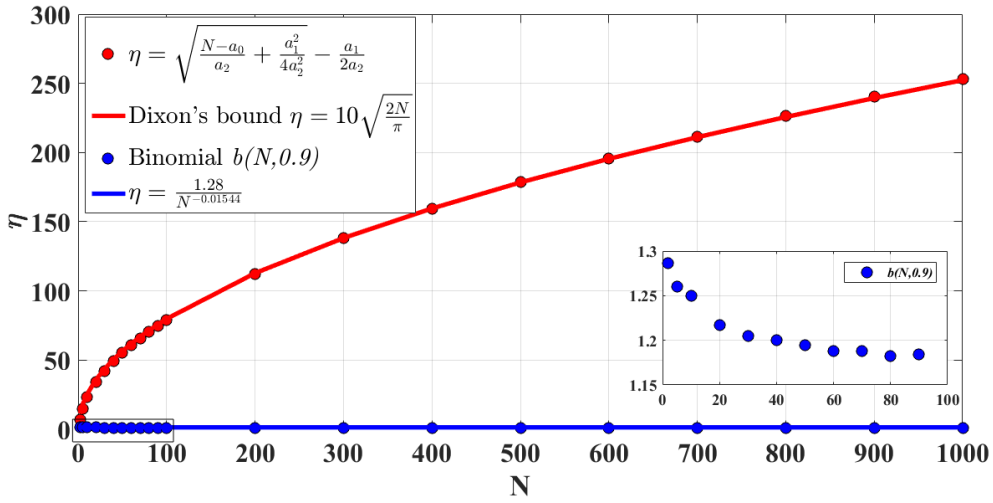

Fig. 4-4. Multiplier Values vs. *N*.

From the previous figure one can infer that the *N* can be modeled as a quadratic function in η for the Gaussian case i.e., $N^G = a_2^G\left(\eta^G\right)^2 + a_1^G\eta^G + a_0^G$ and as a power function for the binomial case $N^B = a_1^B\left(\eta^B\right)^{a_2^B}$ from the observation that for $p_f \le 0.3$ η^B decreases with *N*, where the superscripts G, B refers to Gaussian and Binomial Distributions respectively. This can be rewritten as: $\eta^G = \sqrt{\frac{N^G - a_0^G}{a_2^G} + \frac{\left(a_1^G\right)^2}{4\left(a_2^G\right)^2}} - \frac{a_1^G}{2a_2^G}$;. For the shown case, *s=1* the Gaussian case gave the coefficients $a_2^G = 0.01545,\ a_1^G = 0.03226,\ a_0^G = 1.037.$ looking at these constants reveals that $\eta^G < \frac{1}{\sqrt{a_2^G}}\sqrt{N} \approx 8\sqrt{N}$ this is consistent with Dixon's theory when $p = 1 - \alpha^{-s} = 0.9$ and thus $\alpha = 10$ which means that the multiplier will be $\sqrt{\frac{2}{\pi}}\alpha\sqrt{N} \approx 7.979\sqrt{N}$. Whereas fitting the binomial case gave that $a_1^B = 1.1386E-7$ and $a_2^B = -64.7668$ or in other words, $\eta^B = 1.28N^{-0.01544}$ as shown in figure 4-4. Many facts can be inferred from the figure, for

www.manaraa.com

instance, as N increases the η^G increases, on the contrary as N increases η^B decreases as long as $p_f \leq 0.3$. This is a very appealing behavior as one should not care much for the value of N when dealing with the binomial distribution, instead, the value at $N = 2$ (minimum) can be safely used for it corresponds to the maximum multiplier. Furthermore, the figure shows how the binomial distribution gives a multiplier that significantly less than the one from the Gaussian distribution rendering the estimated norm to be non-conservative enough to lend it more robustness. Next, it is natural to look at how does the probability of failure affect the relation between the binomial multiplier η^B and N. Figure 4-5 performs this inspection and reveals that for $p_f > 0.3$ the multiplier η^B increases as a consequence of larger N.

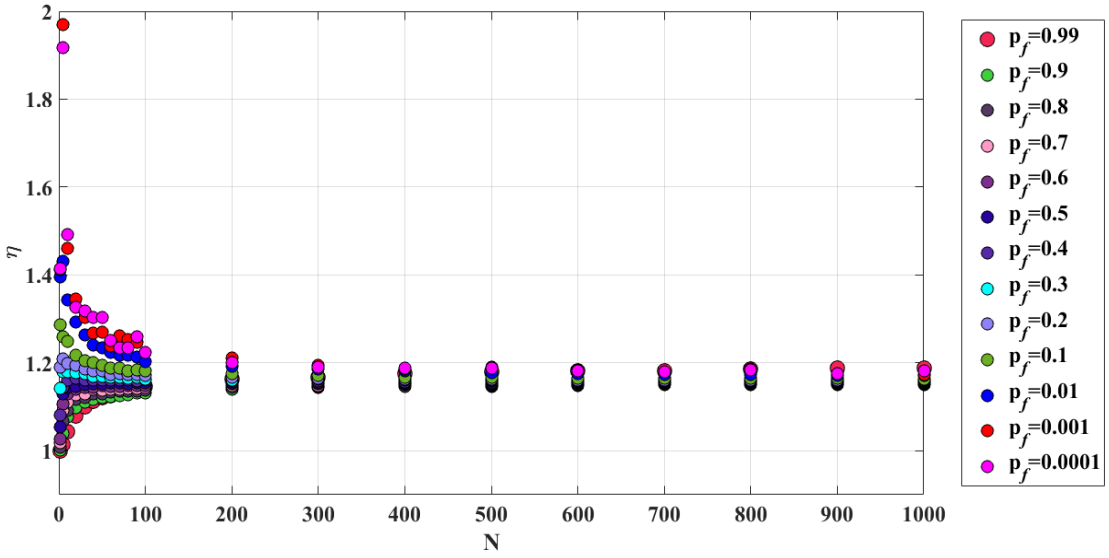

Fig. 4-5. Binomial Multiplier vs. N for different probabilities of failure.

www.manaraa.com

4.4 Propagating Error Bounds across Different Interfaces:

Here we are concerned with the propagation of error bounds across various levels that is to estimate the error due to both reductions based on a reduction in the parameter space only, and a reduction in the response of interest space only. This can be regarded as a brick in the multi-physics error estimation framework [107]. Consider the physical model $y = f(x)$. Let

$$\mathbf{X} = \begin{bmatrix} x_1 & x_2 & \cdots & x_N \end{bmatrix} \text{ and } \mathbf{Y} = \begin{bmatrix} y_1 & y_2 & \cdots & y_N \end{bmatrix}$$

where the vectors x_i's are randomly generated realizations for the parameters whose corresponding responses are given by:

$$y_i = f(x_i)$$

Let

$$\mathbf{X}^x = \mathbf{U}_x^{(r)} \mathbf{U}_x^{(r)T} \mathbf{X};$$

where $\mathbf{U}_x^{(r)}$ defines a basis for the parameters active subspace. Next, define:

$$\mathbf{Y}^x = \begin{bmatrix} y_1^x & y_2^x & \cdots & y_N^x \end{bmatrix};$$

with $y_i^x = f\left(\mathbf{U}_x^{(r)} \mathbf{U}_x^{(r)T} x_i\right)$. Note that the vector y_i^x corresponds to the response value resulting from a single reduction in the parameter space. Next, define:

$$\mathbf{Y}^y = \mathbf{U}_y^{(r)} \mathbf{U}_y^{(r)T} \mathbf{Y}$$

www.manaraa.com

where $\mathbf{U}_y^{(r)}$ is the matrix associated with the response active subspace calculated based on the snapshots matrix $\mathbf{Y}$ (obtained from the Gradient-Free algorithm). Let

$$\mathbf{Y}^{xy} = \mathbf{U}_y^{(r)}\mathbf{U}_y^{(r)T}\mathbf{Y}^x$$

This equation implies two reductions, one embedded in $\mathbf{Y}^x$ due to a reduction in the parameter space followed by another reduction in the response space via the projector $\mathbf{U}_y^{(r)}\mathbf{U}_y^{(r)T}$. To calculate the total errors resulting from both reductions, define the following error bounds:

$$\varepsilon_y^x = \eta \max_{i=1,2,\cdots k_1} \left\| \left(\mathbf{Y} - \mathbf{Y}^x \right) w_i \right\|; \tag{4.31}$$

is the response error due to parameter reduction, and

$$\varepsilon_y^y = \eta \max_{i=1,2,\cdots k_2} \left\| \left(\mathbf{Y} - \mathbf{Y}^y \right) w_i \right\|; \tag{4.32}$$

is the response error due to response reduction. Then the response error due to both reductions can be calculated from:

$$\mathbb{P}\left\{ \left\| \mathbf{Y} - \mathbf{Y}^{xy} \right\| \le \varepsilon_y^x + \varepsilon_y^y \right\} \ge \left(1 - \alpha_1^{-k_1}\right)\left(1 - \alpha_2^{-k2}\right) \tag{4.33}$$

Proof. From the corollary in section 4.3.1 one can write:

$$\mathbb{P}\left\{ \left\| \mathbf{Y} - \mathbf{Y}^x \right\| \le \varepsilon_y^x \right\} \ge \left(1 - \alpha_1^{-k_1}\right) \tag{4.34}$$

$$\mathbb{P}\left\{ \left\| \mathbf{Y} - \mathbf{Y}^y \right\| \le \varepsilon_y^y \right\} \ge \left(1 - \alpha_2^{-k_2}\right) \tag{4.35}$$

www.manaraa.com

But

$$\mathbf{Y}-\mathbf{Y}^{xy}=\left(\mathbf{Y}-\mathbf{Y}^{y}\right)+\mathbf{U}_{y}^{(r)}\mathbf{U}_{y}^{(r)T}\left(\mathbf{Y}-\mathbf{Y}^{x}\right).$$

And hence:

$$\left\|\mathbf{Y}-\mathbf{Y}^{xy}\right\|\le\left\|\mathbf{Y}-\mathbf{Y}^{y}\right\|+\left\|\mathbf{U}_{y}^{(r)}\mathbf{U}_{y}^{(r)T}\right\|\left\|\mathbf{Y}-\mathbf{Y}^{x}\right\|. \tag{4.36}$$

Provided that $\mathbf{U}_{r_y}$ has orthonormal basis, we know that:

$$\left\|\mathbf{U}_{y}^{(r)}\mathbf{U}_{y}^{(r)T}\right\|=1.0\,.$$

Plugging this into (4.36), then taking the probability and substituting from (4.34) and (4.35) we get (4.33).□

Based on the previous theorem it is possible now to establish a stopping criterion for the reduction algorithms based on that the upper-bound computed by the theory should be less than a user-defined tolerance and once this is achieved then we have found the intrinsic dimensionality corresponding to this tolerance. It is time now to introduce the definition, algorithms and applications of ROM in our context.

4.5 Numerical Tests and Results

In this section, two case studies are presented in support of the previous discussions. In the first case study, the binomial estimator is compared to the Averaged Small-Sample Statistical Estimator and the Subspace Statistical Estimator discussed in section 4.2.3. The second case study adopts the propagation technique in section 4.4 to a PWR UO_2 pin cell. A two-stage

www.manaraa.com

reduction is performed on the parameter level and the response level, then on both simultaneously.

4.5.1 Case Study 1: Comparison between Small-Sample Estimators and the Binomial Estimator:

A comparison between the Small-Sample Statistical Estimation methods using both averaged and subspace estimators, and the binomial variant of the small sample estimator is presented. This case study employs computing the norm estimates for a single *N*-dimensional vector using the three formerly mentioned methods, averaged Small-Sample Statistical Estimation, Subspace statistical Estimation, and the Binomial Variant of the small sample estimator. These estimators will be compared once by fixing the probability of success and search for the least multiplier then by fixing the multiplier η then the winning method is the one giving the least probability of failure. Figure 4-6 depicts the case where the upper bound of the theoretical probability of failure is fixed to 0.1 with a single matrix-vector multiplication ($s = 1$).

www.manaraa.com

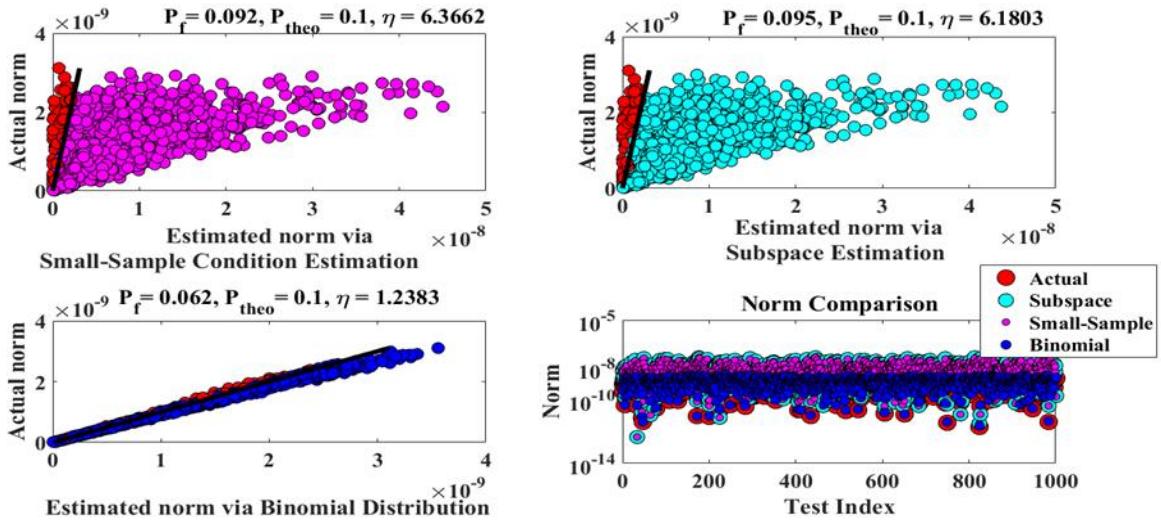

Fig. 4-6. Comparison between norm estimation methods. Upper left: Small-Sample method. Upper right: Subspace norm estimation. Lower left: Binomial Distribution. Lower right: Norm Comparison using the three methods. ($P_f = 0.1$, $s = 1$).

The figure shows that the binomial distribution outperforms the other two methods in this case as it gives the lowest multiplier η = 1.2383 and hence the least conservative bound. Using the binomial distribution exhibits the following desirable features:

- A linear structure around the 45-degree solid black line which promises that even in the failed cases the actual norm is very close to the estimated one.
- A less conservative estimate is constructed which reflects a more robust and realistic bound without violating the expected failure probability.
- The binomial distribution shows less variance as can be inferred from the lower left and right graphs, this explains that most of the tests will be very close to the actual norm.
- Worst case scenario occurs at N = 2 which means that however large was N the analyst can avoid pre-computing the corresponding multiplier and uses the one corresponding to N = 2

www.manaraa.com

using a conservative bound but still far less conservative than the other methods using standard normal distributions.

Next to give room for the subspace condition estimator to better perform we need to increase *s* and hence use more orthonormal vectors to enhance the performance of that method. Figure 4-7 compares the methods using $s = 4$ and still use the multiplier values results in a comparable probability of failure of 0.1. The figure shows that with as low as four matrix-vector multiplications (or four orthonormal basis vectors for the subspace method), the binomial distribution can pick a more accurate estimate.

Figure 4-7 supports that the binomial distribution exhibits a significantly less variance (lower left corner) and a closer mean to the actual mean where the remaining two methods sometimes are off by two orders of magnitude from the actual norm as can be inferred from the right lower corner. It can be concluded from a quick peak to the top two graphs that both tests are identical in the estimated norms, this is obviously because only one random vector was used (i.e., $s = 1$). This will not show the significance of the subspace estimator until more vectors are used. Figure 4.7 depicts the same test using 4 random vectors ($s = 4$).

www.manaraa.com

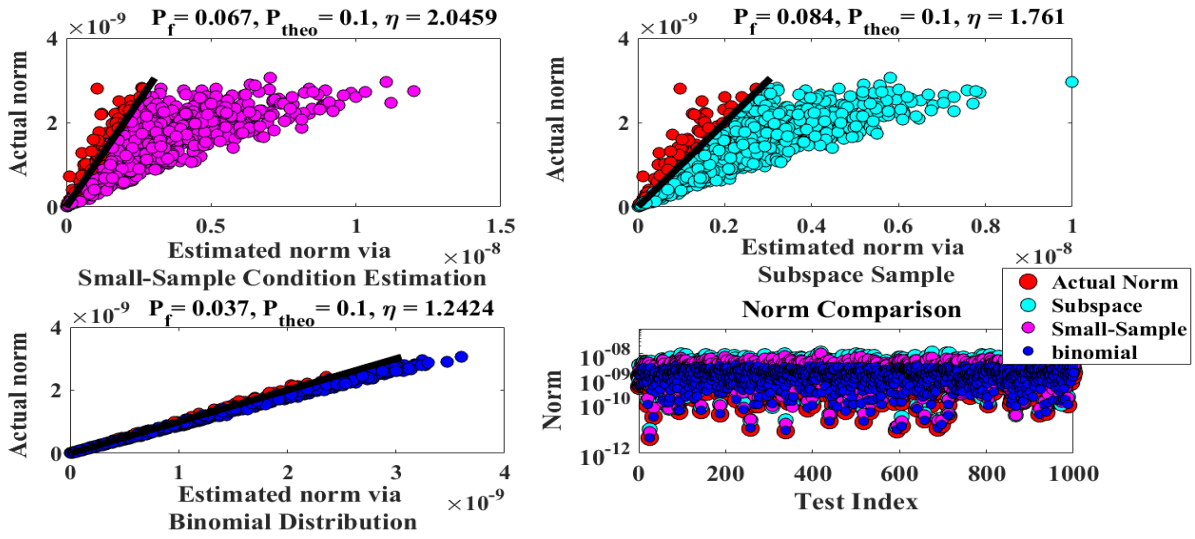

Fig. 4-7. Comparison between norm estimation methods. Upper left: Small-Sample method. Upper right: Subspace norm estimation. Lower left: Binomial Distribution. Lower right: Norm Comparison using the three methods. ($P_f = 0.1$, $s = 4$).

In this case, the Subspace estimator gives better results than the Small-Sample estimator in the sense that it results in a smaller multiplier and hence a closer estimate, yet the binomial distribution is still giving slightly closer estimates and less failed cases. These cases are conducted based on a probability of failure of $P_f = \left[p_f\left(\eta, \mathcal{D}\right)\right]^s = \left(0.5623\right)^4 = 0.1$. This was selected to be impractically high to force more failures, in practice this probability is taken to be at least $P_f = \left[p_f\left(\eta, \mathcal{D}\right)\right]^s = \left(0.1\right)^4 = 0.0001$. Figure 4-7 draws a more practical view of the test. To correctly predict %99.99 of the cases the estimated norm/bound might reach at least 10 times the actual norm in both Small-Sample estimators whereas this multiplier $\left(\eta\right)$ will still lie between 1 -2 using the binomial distribution. These values can be verified from tables I, II in

www.manaraa.com

[104] for N = 20, m = 4 and p = 0.9999 $\alpha \simeq 10$ which are similar to our (N, s, p and η respectively).

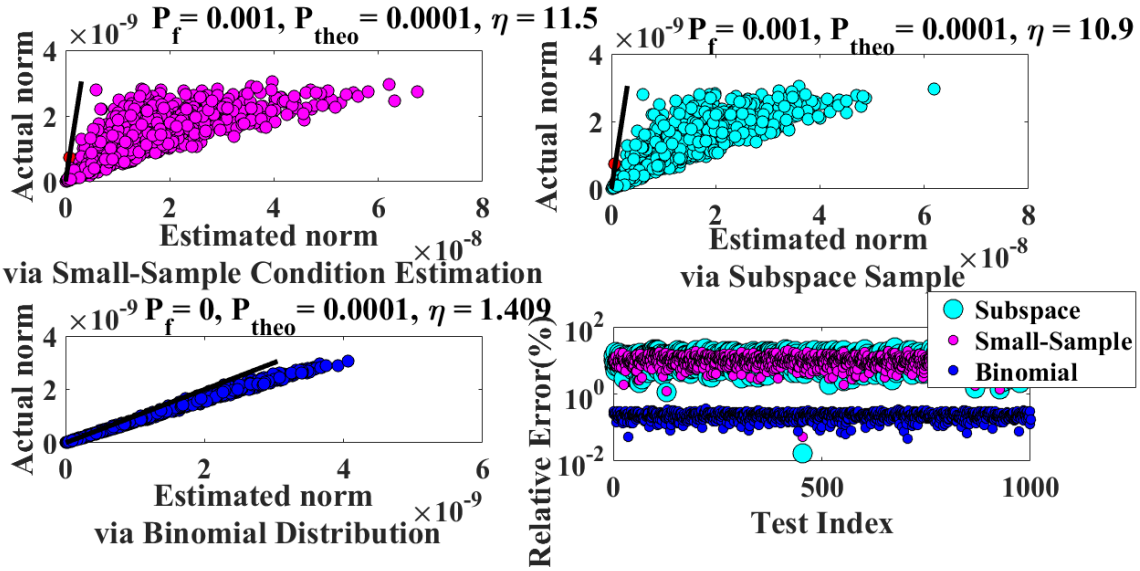

Fig. 4-8. Comparison between norm estimation methods. Upper left: Small-Sample method. Upper right: Subspace norm estimation. Lower left: Binomial Distribution. Lower right: norm comparison using the three methods. (P_f = 0.0001, s = 4).

Previous tests examined the performance of the binomial estimator vs. two Small-Sample Statistical Estimation by fixing the user-defined probability of success. What if the multiplier η is fixed, which estimator will outperform the rest?

Figures 4-9 through 4-11 illustrate the cases where the multiplier η is user-defined and the probabilities of failure are inspected along with the error from the actual norm in each case.probabilities of failure are inspected along with the error from the actual norm in each case.

www.manaraa.com

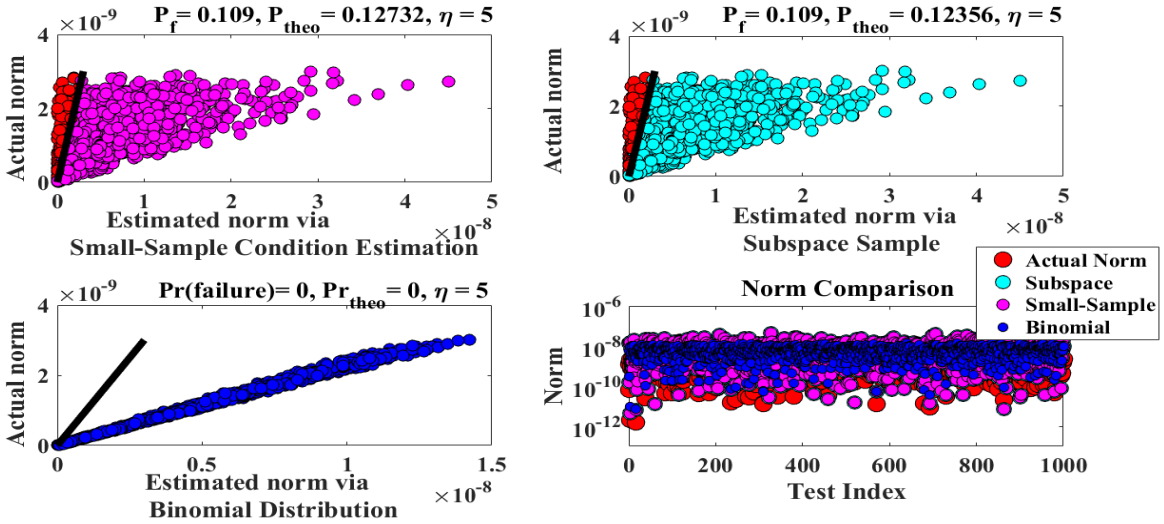

Fig. 4-9. Comparison between norm estimation methods. Upper left: Small-Sample method. Upper right: Subspace norm estimation. Lower left: Binomial Distribution. Lower right: norm comparison using the three methods. ($\eta = 5$, $s = 1$).

Figure 4-9 clearly shows that a multiplier of 5 is too large for the binomial estimator and unlike the other methods where some cases lied close to the 45-degree solid line showing that actual norm can still be close or maybe larger than the estimated one, the binomial estimators were all very far from the line which means that these bounds (estimators) are impractically conservative. This motivates the use of the multiplier values from the binomial distribution for all other methods, moreover, the bottom right graph is replaced by relative errors in norm estimation instead of plotting the norm value because these values are expected to be close to each other for the three methods since we have forced the same multiplier.

www.manaraa.com

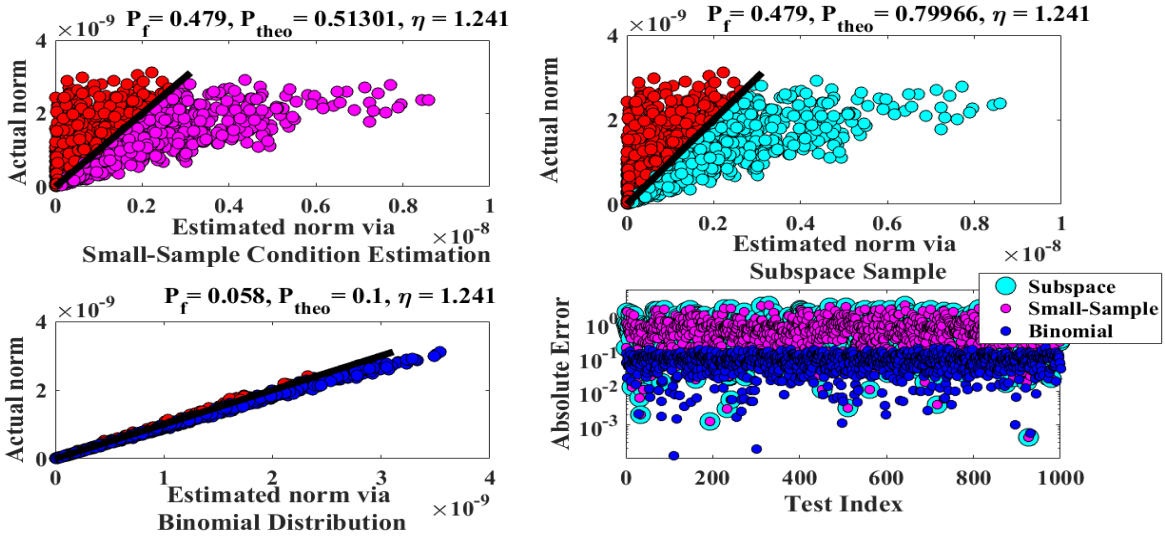

Fig. 4-10. Comparison between norm estimation methods. Upper left: Small-Sample method. Upper right: Subspace norm estimation. Lower left: Binomial Distribution. Lower right: norm comparison using the three methods. ($\eta = 1.241$, s = 1).

It can be seen in figure 4-10 that the binomial estimator can be within a factor of 1.241 from the actual norm and still gives a probability of failure that is less than 0.1 using a single random vector multiplication, whereas in both Small-Sample variants the probability of failure is exceeding %50 for the same factor $\eta = 1.241$. However, Even with the same multiplier, the binomial estimator relative error is from 1-3 orders of magnitudes less than the other Small-Sample methods. This can be enhanced even more using 4 random vector multiplications (i.e. s=4 implying 4 orthonormal basis vectors in the subspace estimator method) as shown in the following figure.

www.manaraa.com

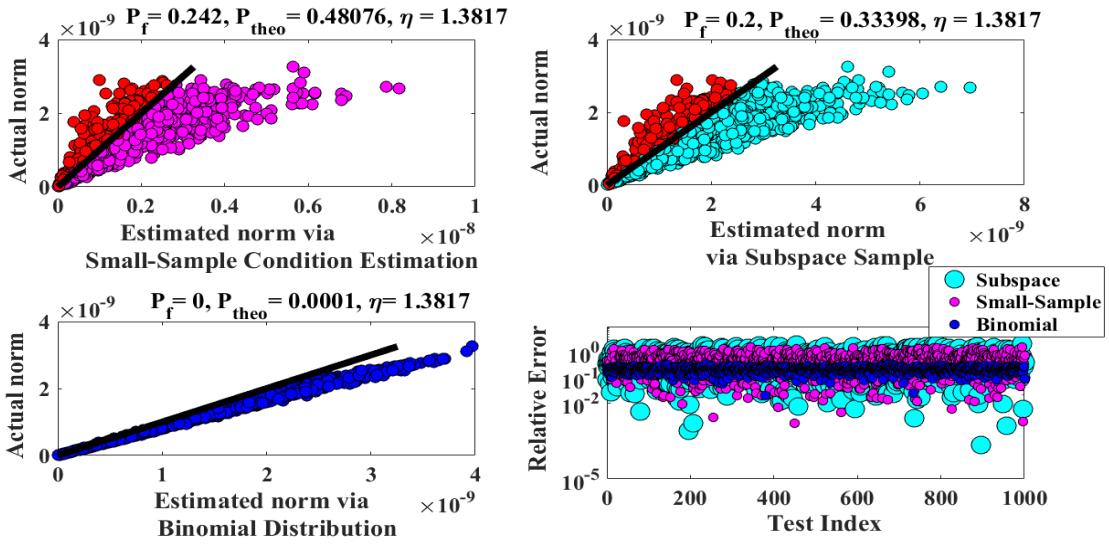

Fig. 4-11. Comparison between norm estimation methods. Upper left: Small-Sample method. Upper right: Subspace norm estimation. Lower left: Binomial Distribution. Lower right: norm comparison using the three methods. ($\eta = 1.3817$, s = 4).

Using s=4 enhanced both the Small-Sample and the Subspace estimators but the binomial distribution still gives a probability of failure of $p_f = (0.1)^4 = 0.0001$, where the probability of failure for both Small-Sample and Subspace estimators methods are reduced to 0.242 and 0.2 respectively. The relative error is still at least one order of magnitude less than the other two.

4.5.2 Case Study 2: Bounding a Nonlinear Vector-Valued Function.

In this case study, a nonlinear multi-response function is tailored to adequately assess the outcome of nonlinearity on active subspace identification algorithm, compare the classical Gradient-Based methodology to the use of the pseudo response trick and finally compare the binomial estimator to Small-Sample Statistical Estimators showing how these methods can set a priori bound and use it for future runs. For these goals consider the function $y = f(x)$ where:

www.manaraa.com

$x \in \mathbb{R}^{15}$ and $y \in \mathbb{R}^{13}$. Such that $y = \begin{pmatrix} y_I^T & y_{II}^T & y_{III}^T \end{pmatrix}^T$;

$$y_I = \begin{pmatrix} a_1^T x & \left(a_2^T x\right)^2 & \cos\left(a_3^T x\right) & \sin\left(a_4^T x\right) & \tan\left(a_5^T x\right) \end{pmatrix}^T;$$

$$y_{II} = \begin{bmatrix} \cos^2\left(a_6^T x\right) & \sin^2\left(a_7^T x\right) & \tan^2\left(a_8^T x\right) & e^{a_9^T x} & 1/\left(1+e^{a_{10}^T x}\right) \end{bmatrix}^T$$

and

$$y_{III} = \begin{bmatrix} x^T \sin\left(a_{11} \bullet * x\right) & \cos\left(a_{12}^T x + \left(a_{12}^T x\right)^2\right) & \sin\left(a_{12}^T x + \left(a_{12}^T x\right)^2\right) \end{bmatrix}^T$$

where the $(\bullet *)$ operator stands for the product of corresponding elements, i.e., $a_1 \bullet * x = \begin{pmatrix} a_{11}x_1 & a_{21}x_2 & \cdots & a_{(15)1}x_{15} \end{pmatrix}^T$. It is obviously clear that many of these y's are correlated either linearly or nonlinearly. Also among the components of *x* itself, few constraints are added to inject some correlations and hence reducibility. The gradient is analytically computed using the symbolic differentiation in MATLAB and the pseudo response is defined such that $R^{pseudo} = b^T y$; where *b* is a random weighting vector, the derivatives of the pseudo-responses are stored in **J** where the derivatives of the original individual responses are stored in $\left[\mathbf{G}_k\right]_{ij} = \frac{\partial y_k}{\partial x_{ij}}$.

The Singular Value Decomposition (SVD) [93, 96] for both derivatives are carried out and based on that the orthonormal columns of the active subspaces for the whole function and the individual responses are identified from the left singular matrices from **J** and $\mathbf{G}_k$ respectively.

The following first set of figures depicts the comparison between the binomial estimator, the Averaged Small-Sample Statistical Estimation and the Subspace Statistical Estimator and their ability to estimate the norm of error vector due to projection onto the active subspace $\mathbf{U}_x^{(r)}$ extracted from the sensitivities of pseudo-responses, i.e.,

www.manaraa.com

$$\|e_k\| = \left\| \frac{f_k(x_1) - f_k\left(\mathbf{U}_x^{(r)}\mathbf{U}_x^{(r)T}x_1\right)}{f_k(x_1)} \quad \cdots \quad \frac{f_k(x_N) - f_k\left(\mathbf{U}_x^{(r)}\mathbf{U}_x^{(r)T}x_N\right)}{f_k(x_N)} \right\|.$$ Figures 4-12 thru 4-24

illustrate the estimated error norm for each response and compare the accuracy of the estimators.

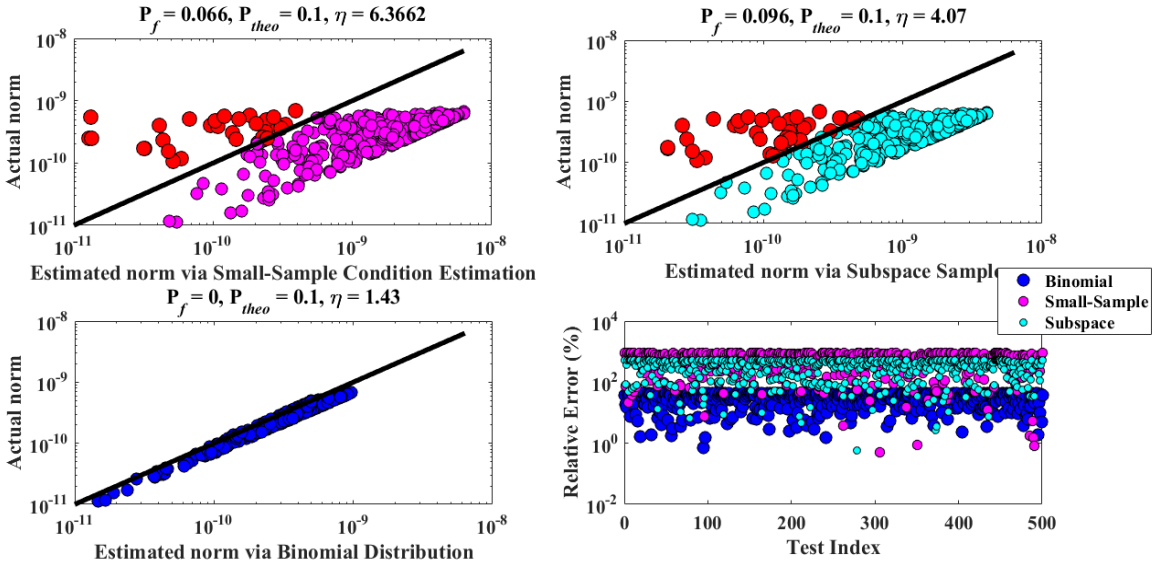

Fig. 4-12. Comparison of Errors in y_1.

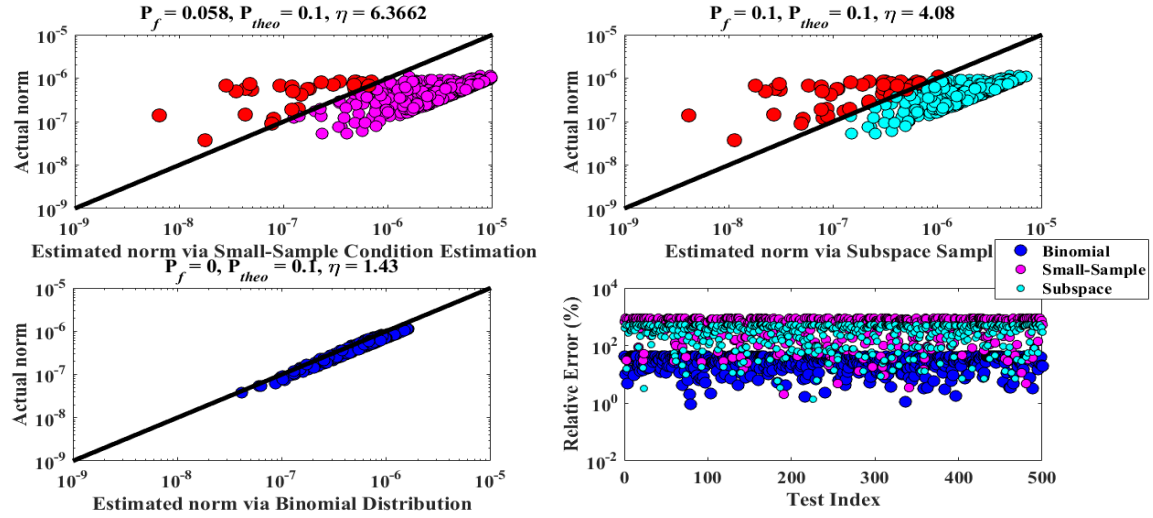

Fig. 4-13. Comparison of Errors in y_2

www.manaraa.com

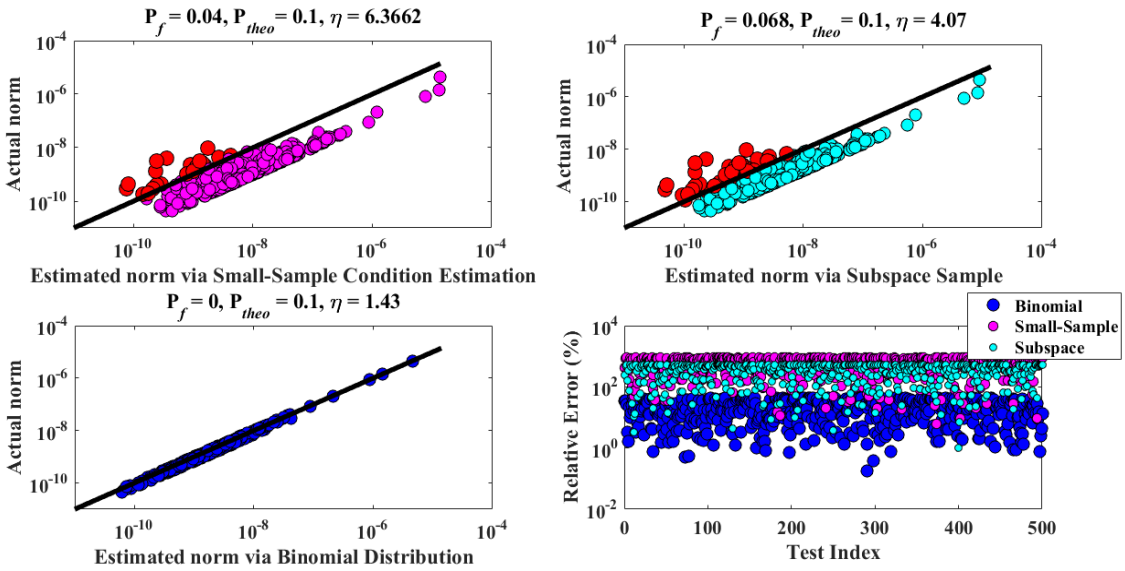

Fig. 4-14. Comparison of Errors in y_3.

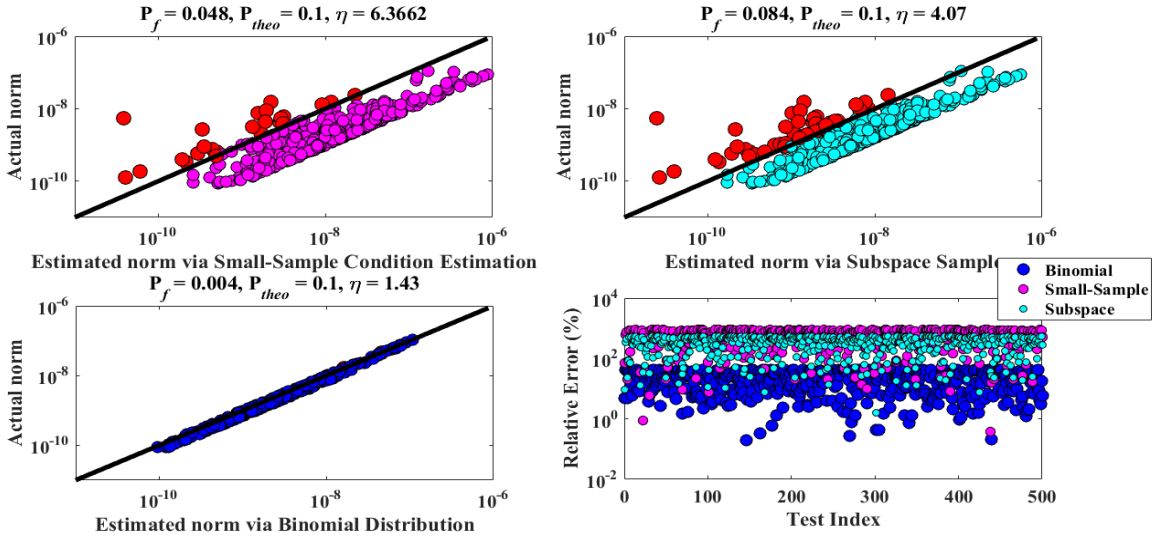

Fig. 4-15. Comparison of Errors in y_4.

www.manaraa.com

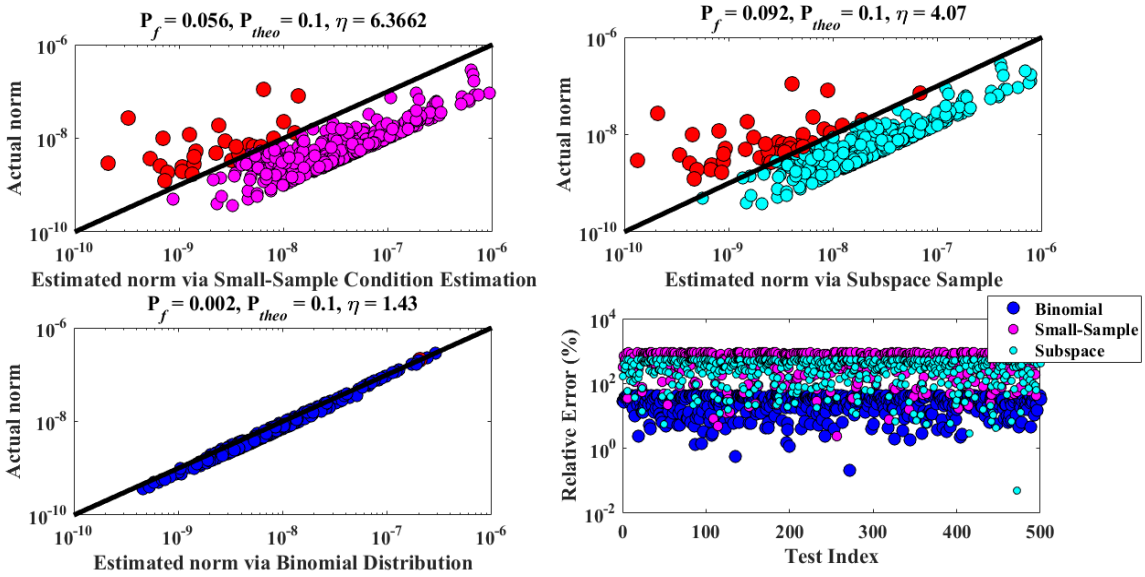

Fig. 4-16. Comparison of Errors in y_5.

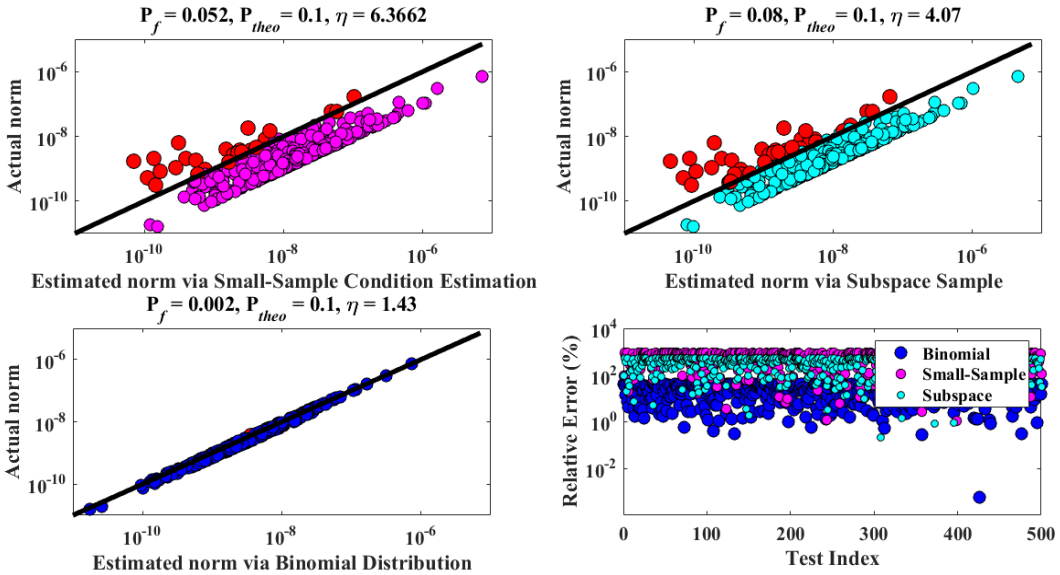

Fig. 4-17. Comparison of Errors in y_6.

www.manaraa.com

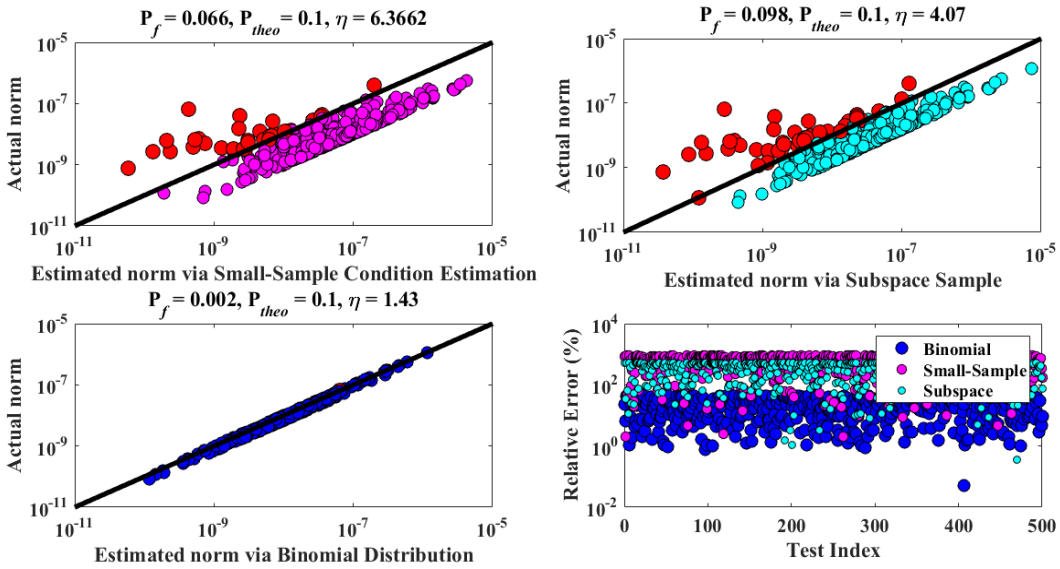

Fig. 4-18. Comparison of Errors in y_7.

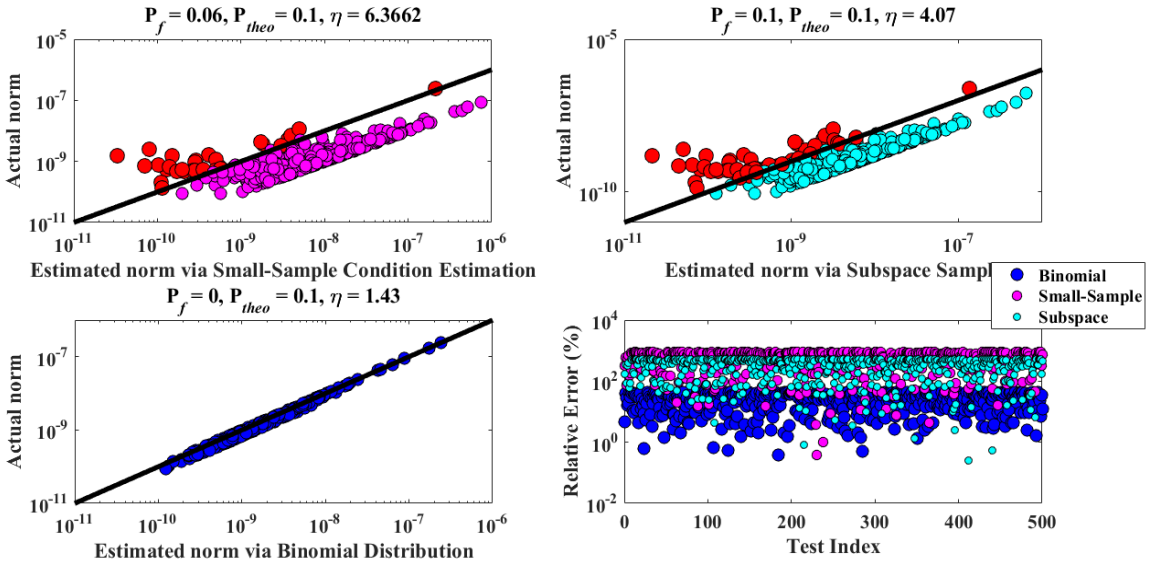

Fig. 4-19. Comparison of Errors in y_8.

www.manaraa.com

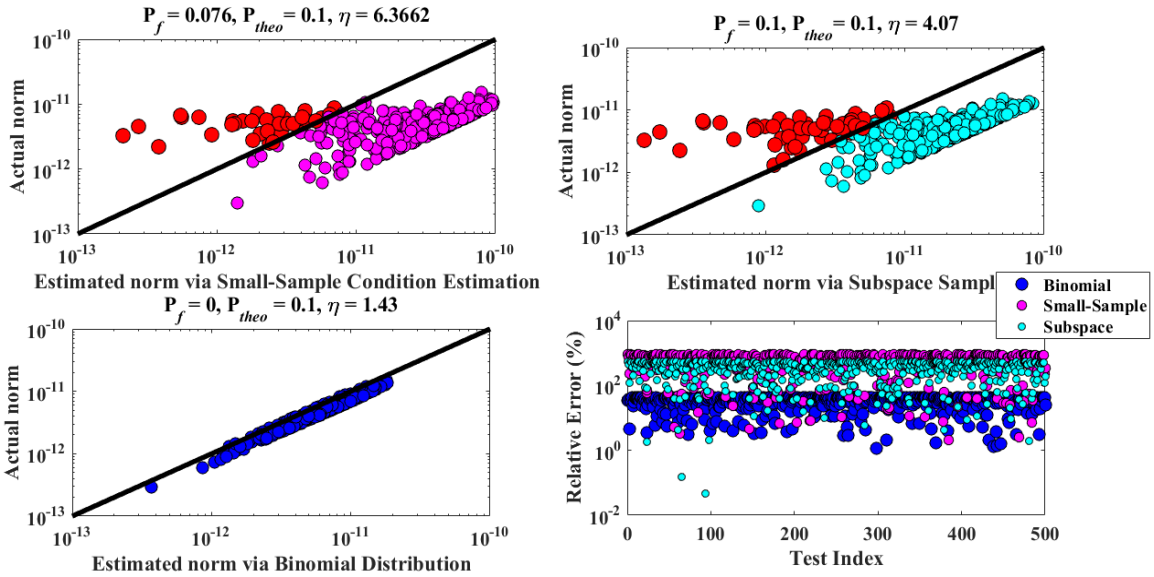

Fig. 4-20. Comparison of Errors in y_9.

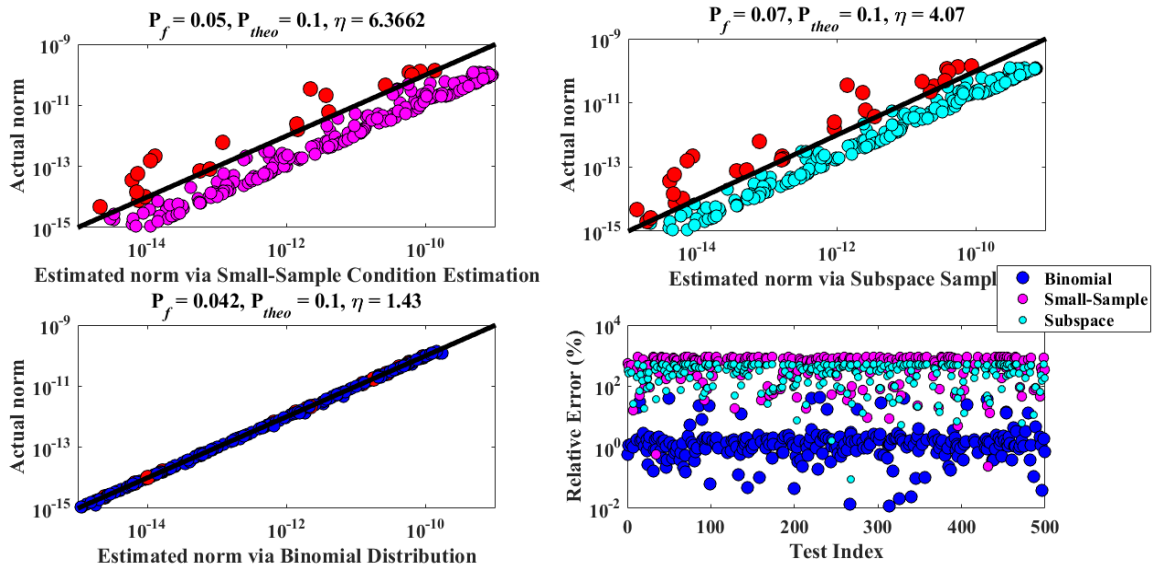

Fig. 4-21. Comparison of Errors in y_{10}.

www.manaraa.com

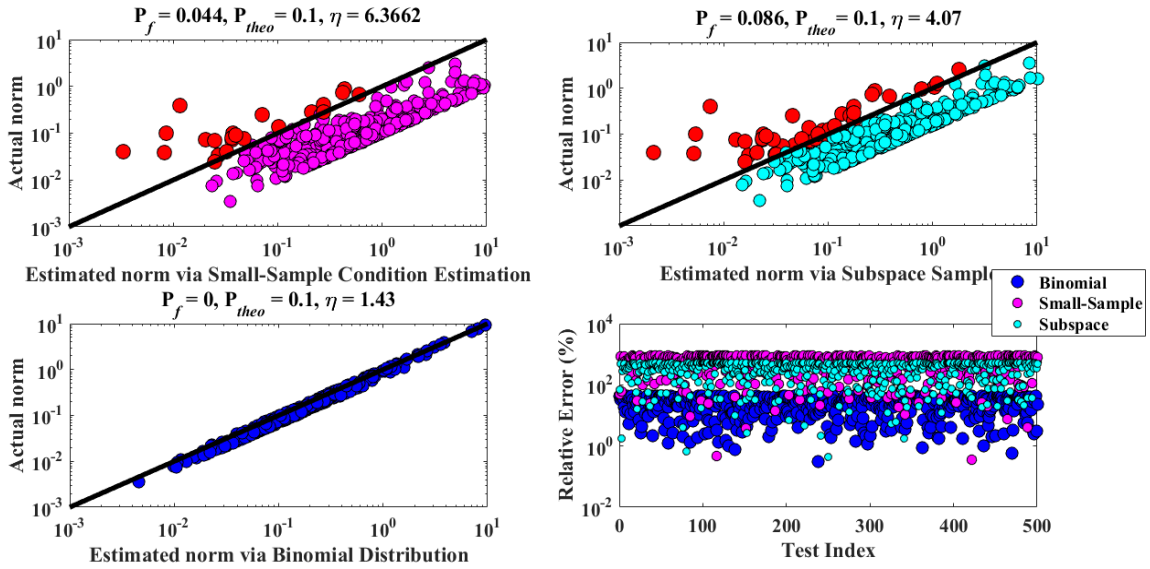

Fig. 4-22. Comparison of Errors in y_{11}.

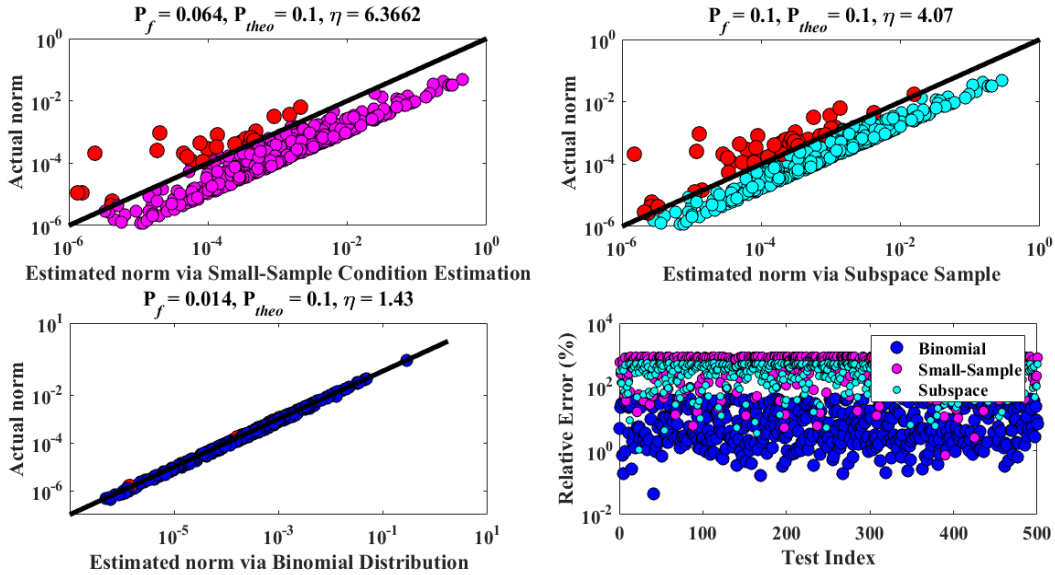

Fig. 4-23. Comparison of Errors in y_{12}.

www.manaraa.com

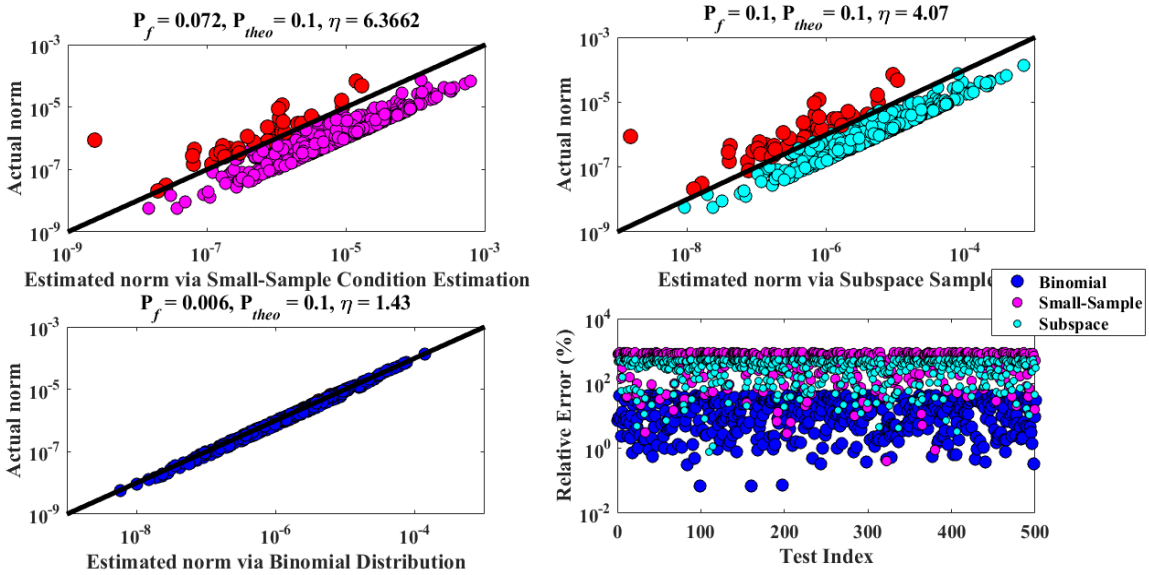

Fig. 4-24. Comparison of Errors in y_{13}.

The figures demonstrate the same result of the binomial estimator outperforming the averaged and the Subspace Statistical Estimator giving the least multiplier with fewer failures (higher actual probability of success). This is showing that the methodology not only works for estimating random norms but also predicts reasonable estimates for the errors resulting from constraining the inputs to the proposed active subspace. The figures defend the claim that the high nonlinearity might affect the quality of the basis and hence increase the errors for a given size of the active subspace but this nonlinearity will not affect the accuracy of the estimators and hence the estimated error bounds will reflect the quality of the active subspace suggesting more sampling and better basis. Next set of figures (i.e., from fig 4-25 to 4-37) assess the bounds for new runs showing whether these bounds are violated once new perturbations are performed given that these perturbations are still constrained to the same subspace.subspace but this nonlinearity will not affect the accuracy of the estimators and hence the estimated error bounds will reflect the quality of the active subspace suggesting more sampling and better basis. Next set of figures (i.e., from fig 4-24 to 4-.36) assess the bounds for new runs showing whether these

www.manaraa.com

bounds are violated once new perturbations are performed given that these perturbations are still constrained to the same subspace.

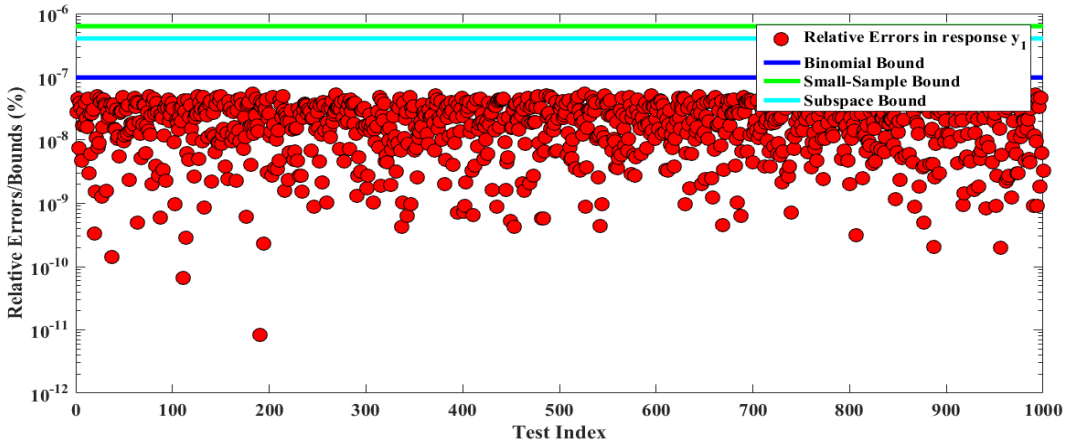

Fig. 4-25. Bounds of y_1 at different runs.

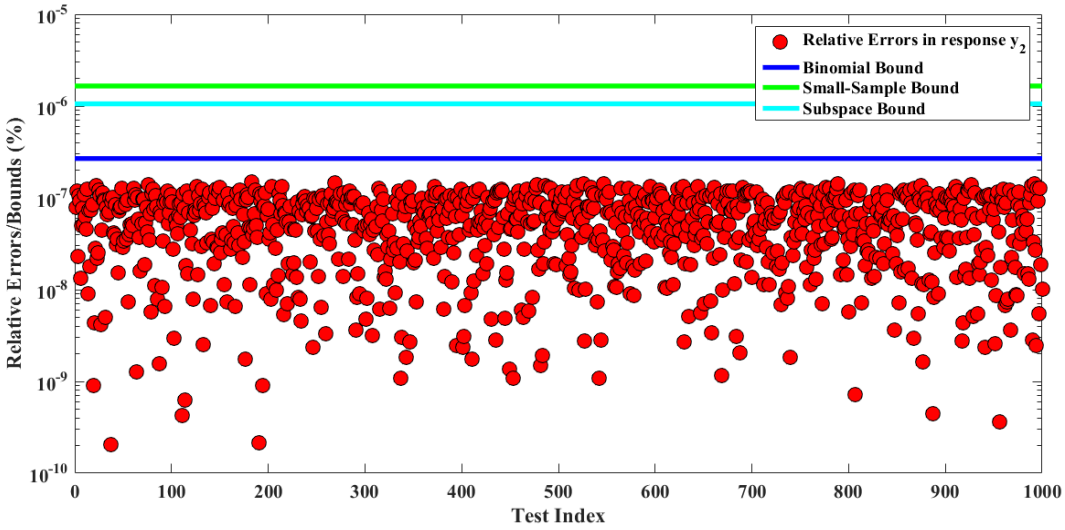

Fig. 4-26. Bounds of y_2 at different runs.

www.manaraa.com

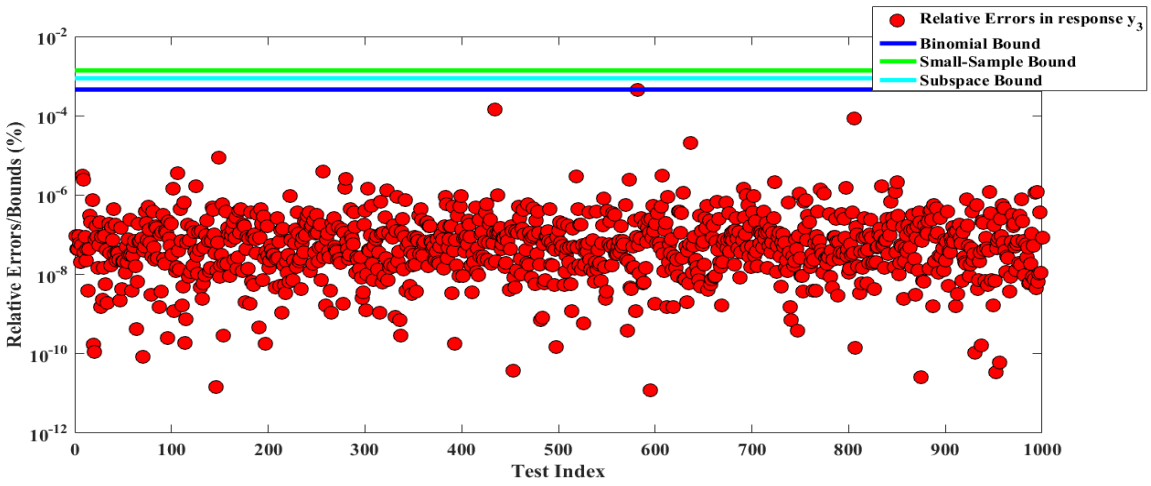

Fig. 4-27. Bounds of y_3 at different runs.

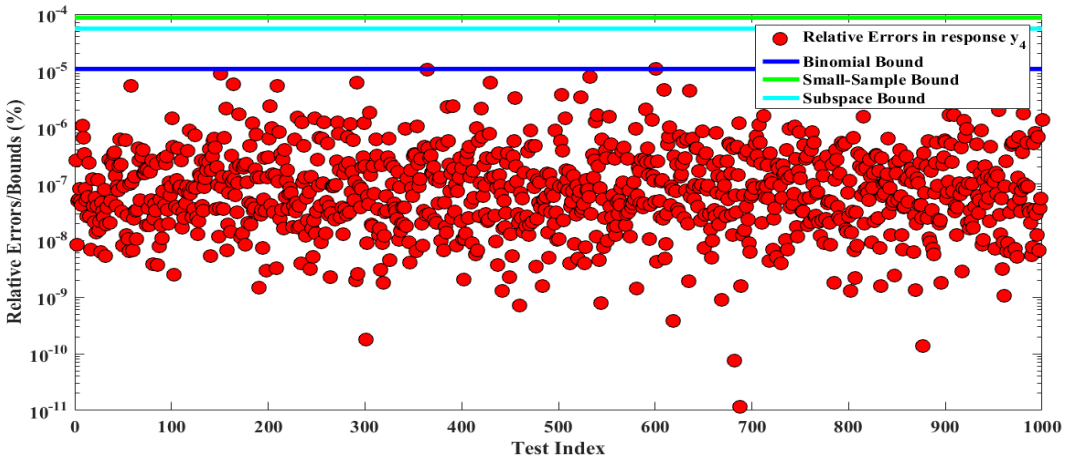

Fig. 4-28. Bounds of y_4 at different runs.

www.manaraa.com

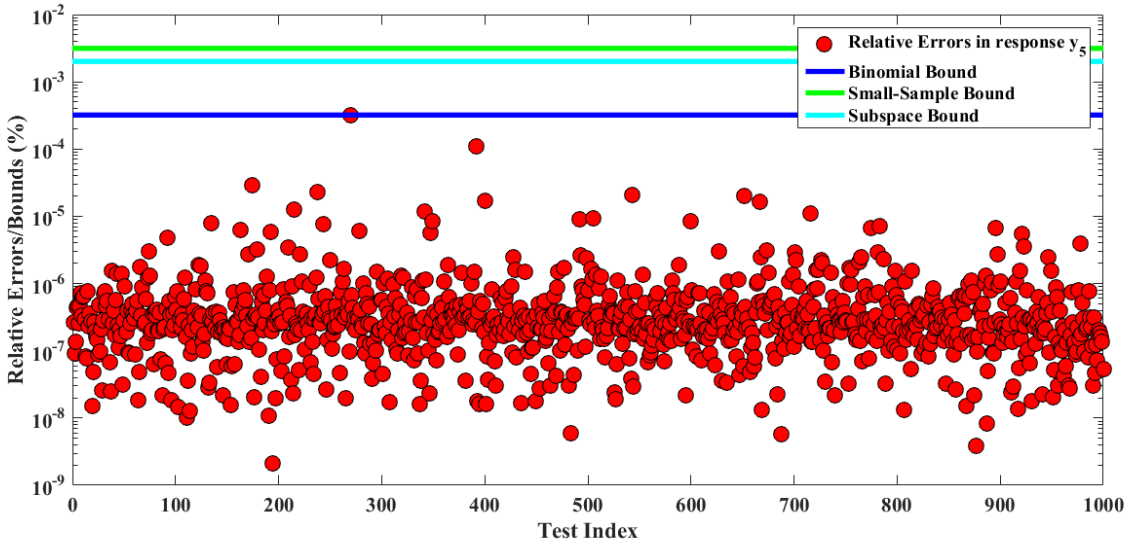

Fig. 4-29. Bounds of y_5 at different runs.

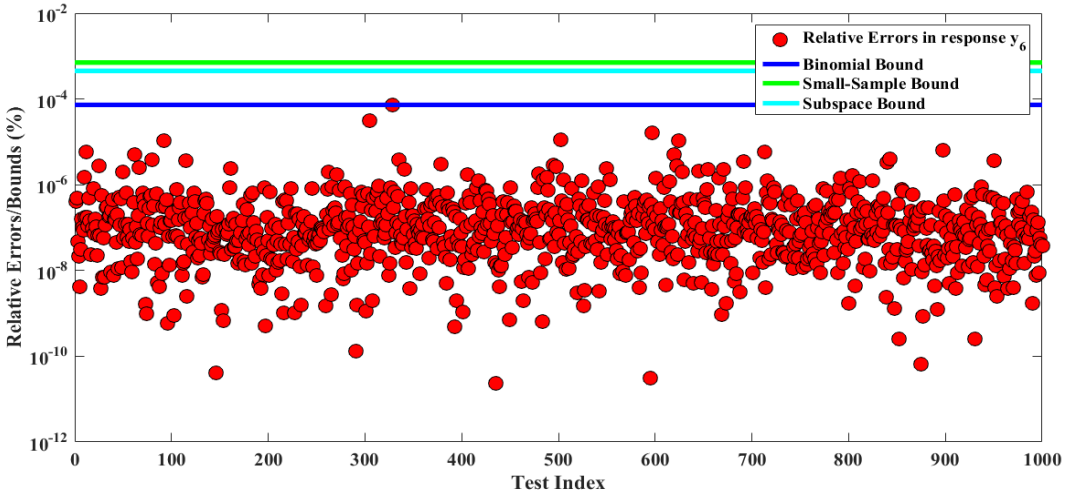

Fig. 4-30. Bounds of y_6 at different runs.

www.manaraa.com

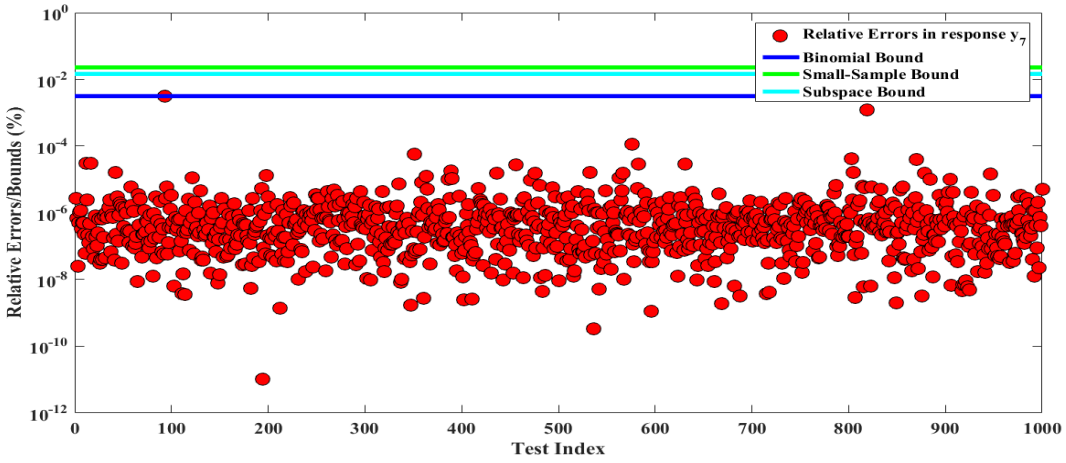

Fig. 4-31. Bounds of y_7 at different runs.

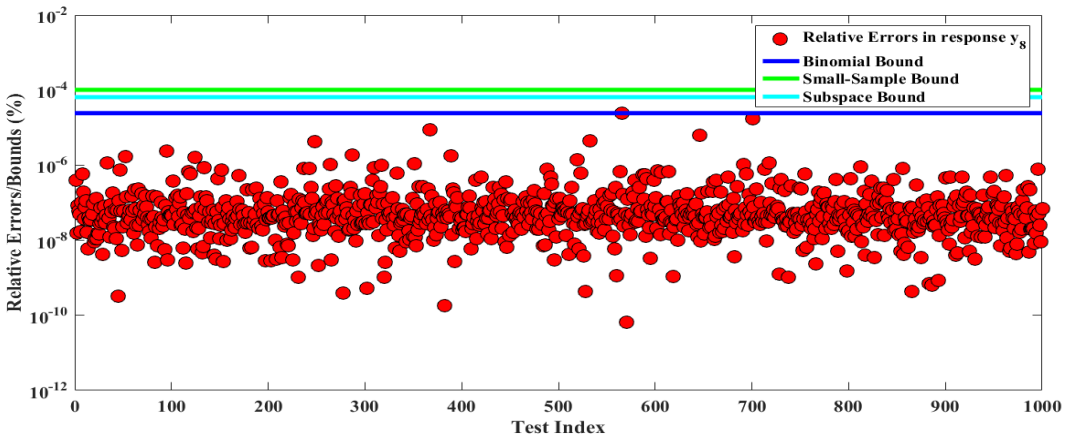

Fig. 4-32. Bounds of y_8 at different runs.

www.manaraa.com

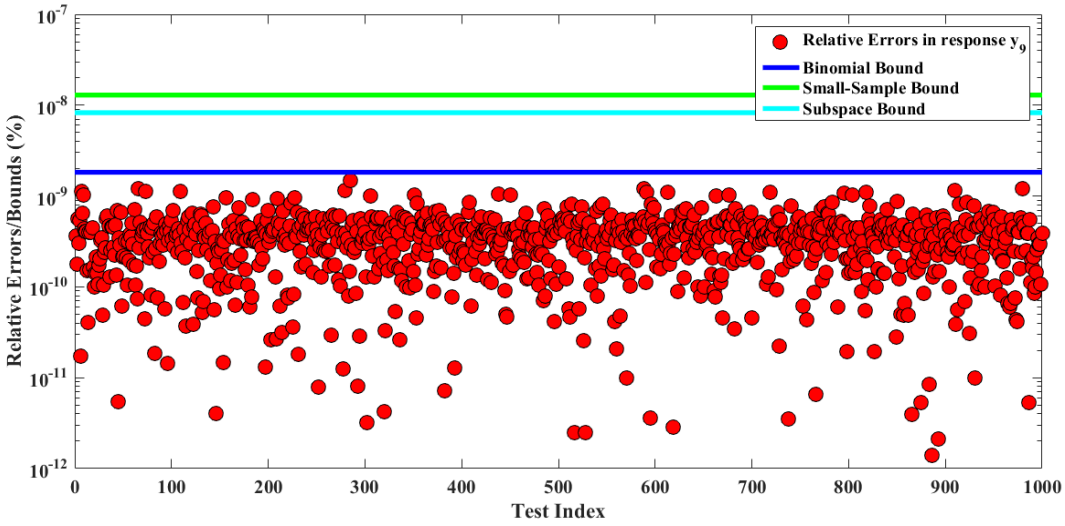

Fig. 4-33. Bounds of y_9 at different runs.

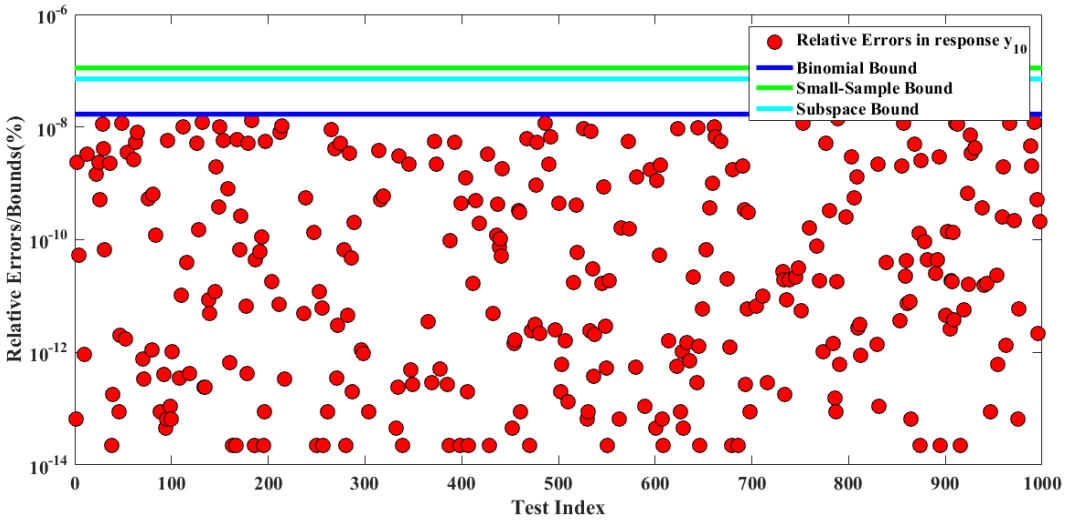

Fig. 4-34. Bounds of y_{10} at different runs.

www.manaraa.com

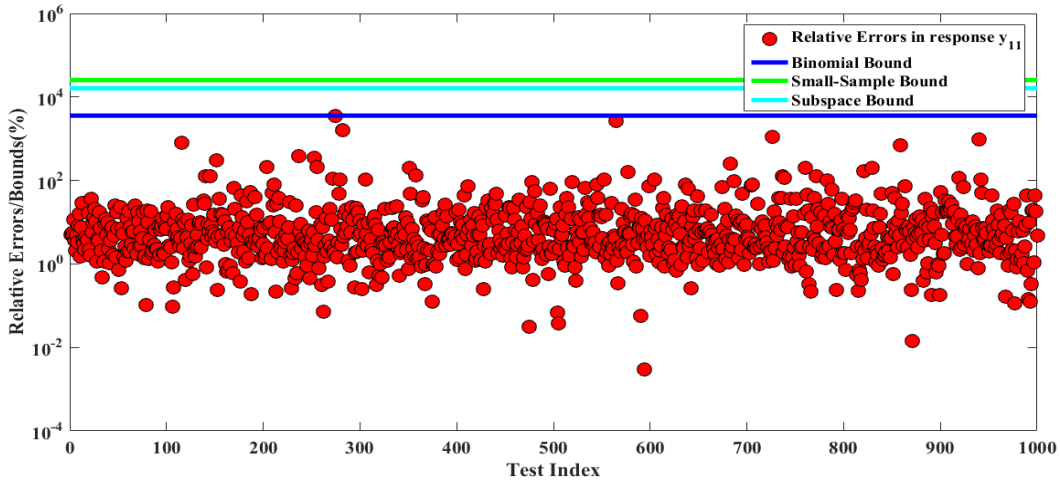

Fig. 4-35. Bounds of y_{11} at different runs.

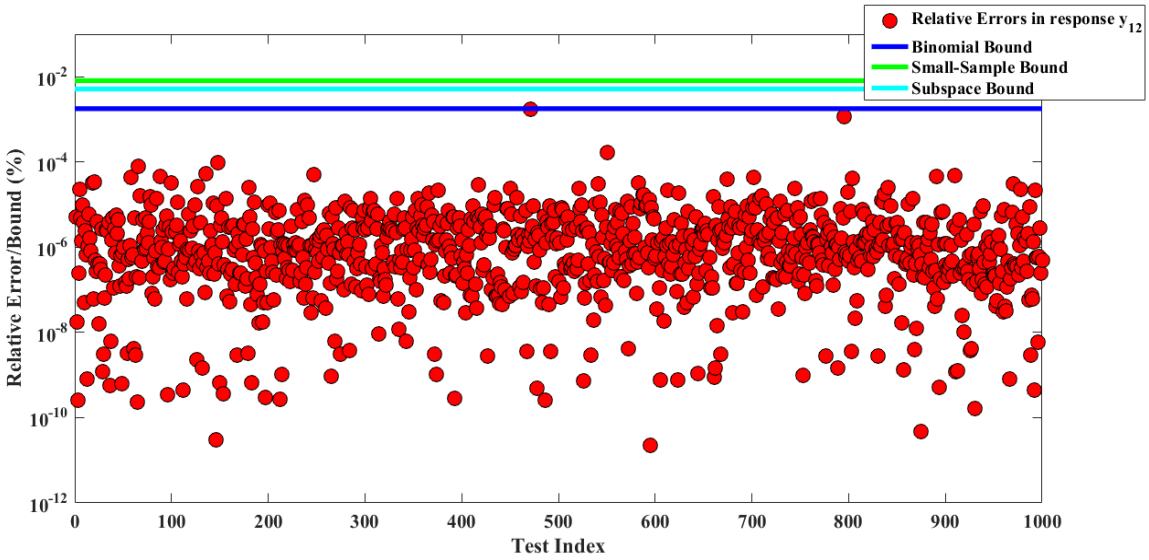

Fig. 4-36. Bounds of y_{12} at different runs.

www.manaraa.com

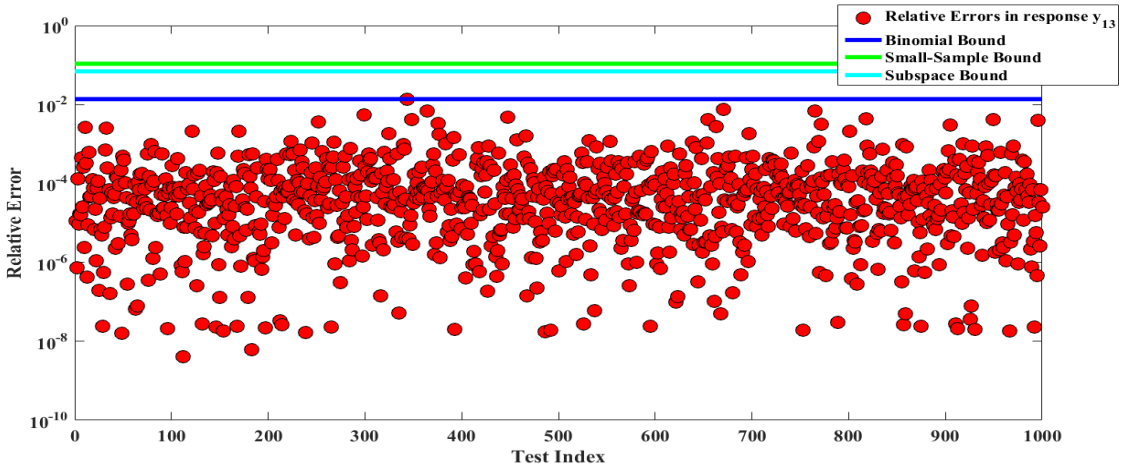

Fig. 4-37. Bounds of y_{13} at different runs.

It is noteworthy that y_{11} gives an extremely large error which reflects that this particular response was not efficiently captured by the active subspace and thus the user needs to sample to add more basis vectors to the active subspace if this individual response is of high interest.

Next, we compare the subspaces extracted for each response individually versus the subspace extracted using the pseudo response. Figures 4-38 thru 4-50 are dedicated to that goal, each figure illustrates the error in one response due to projection onto the subspaces extracted based on each response along with the subspace extracted based on the sensitivities of the pseudo response. It is intuitive to expect that for instance, the error in a certain response will be minimum using the active subspace extracted from the sensitivities of that same response, but how will it the other subspaces behave? The answer can be inferred from the following figures.

www.manaraa.com

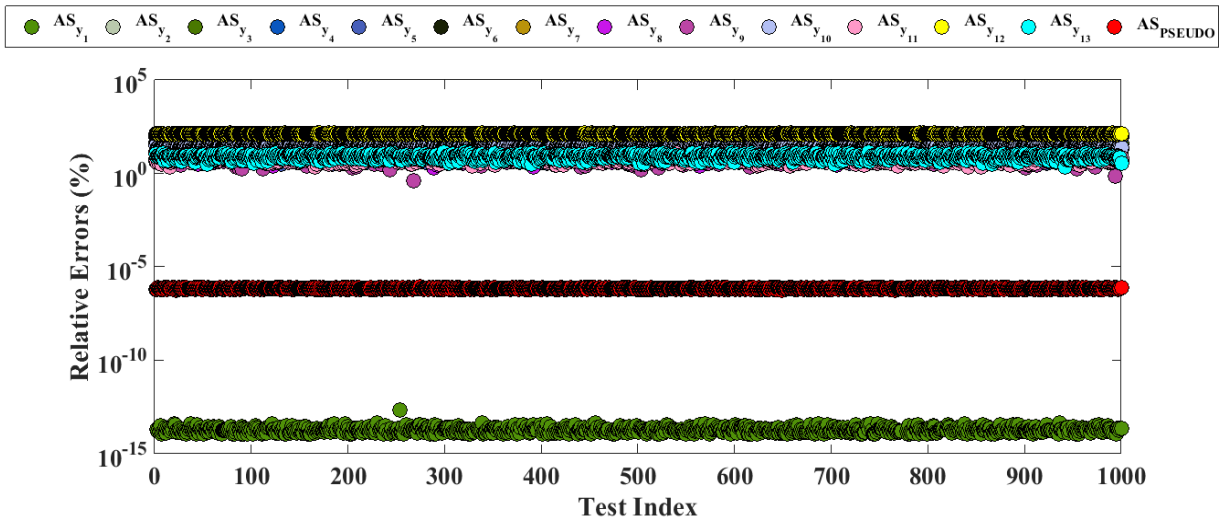

Fig. 4-38. Errors in y_1 due to projection onto all subspaces.

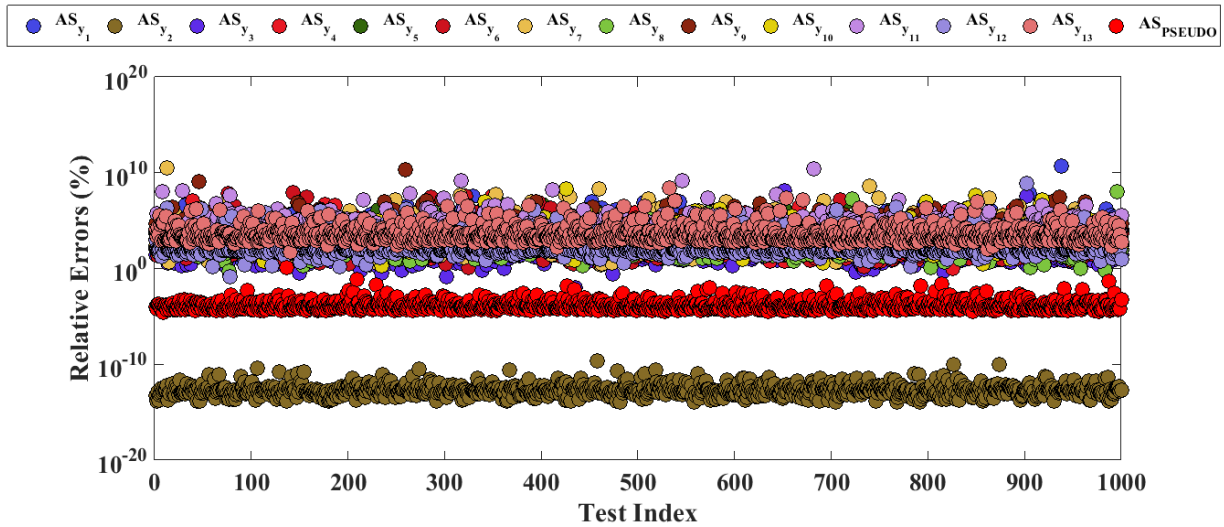

Fig. 4-39. Errors in y_2 due to projection onto all subspaces.

www.manaraa.com

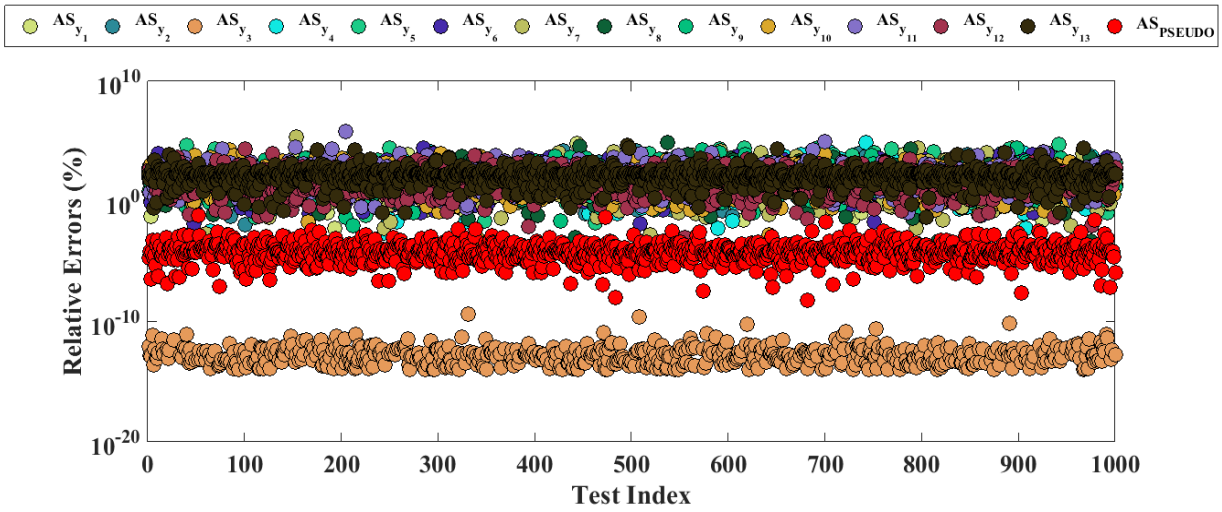

Fig. 4-40. Errors in y_3 due to projection onto all subspaces.

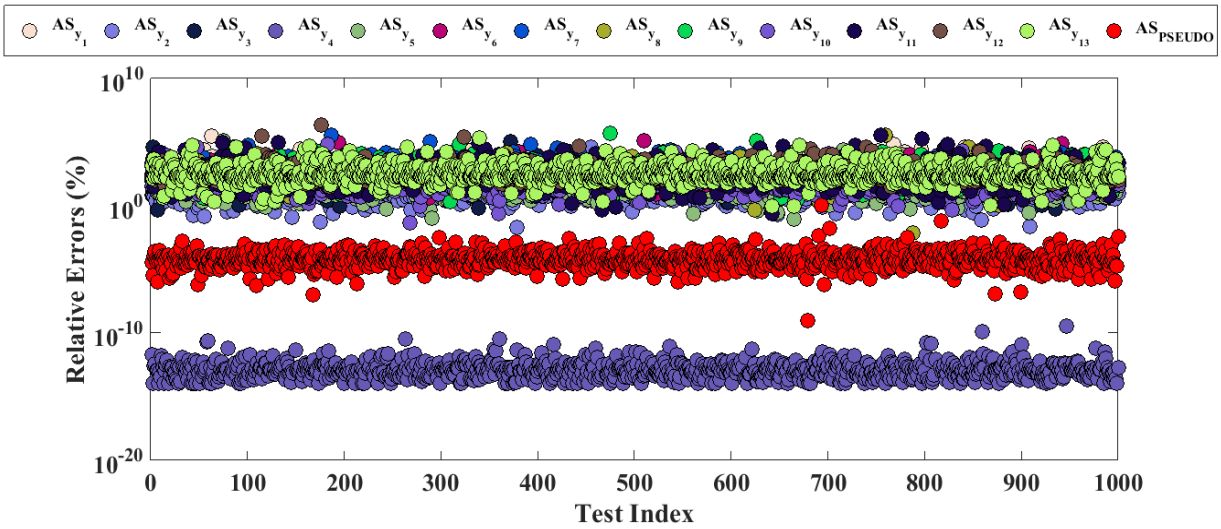

Fig. 4-41. Errors in y_4 due to projection onto all subspaces.

www.manaraa.com

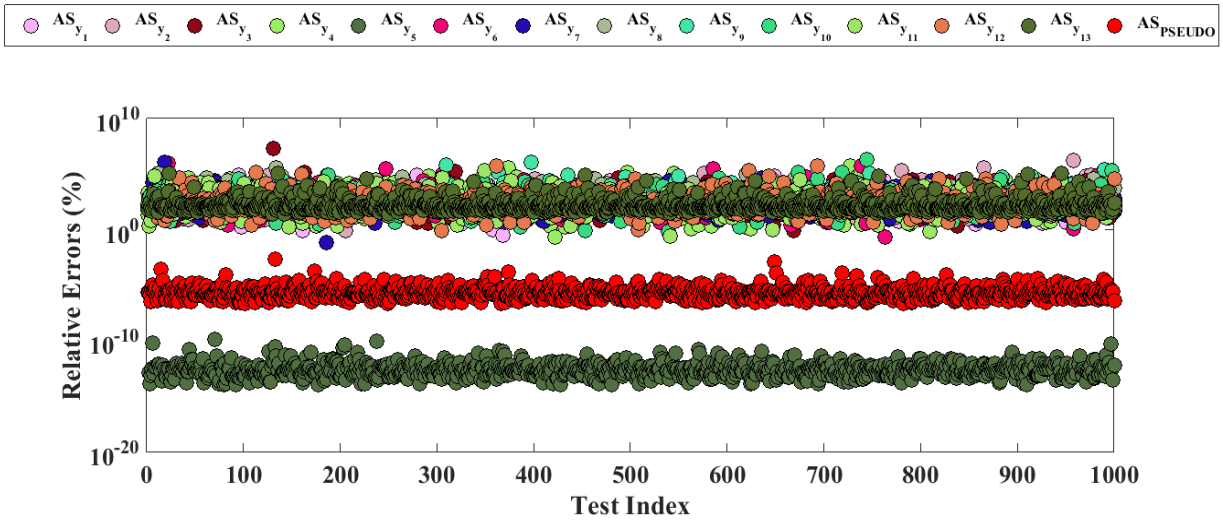

Fig. 4-42. Errors in y_5 due to projection onto all subspaces.

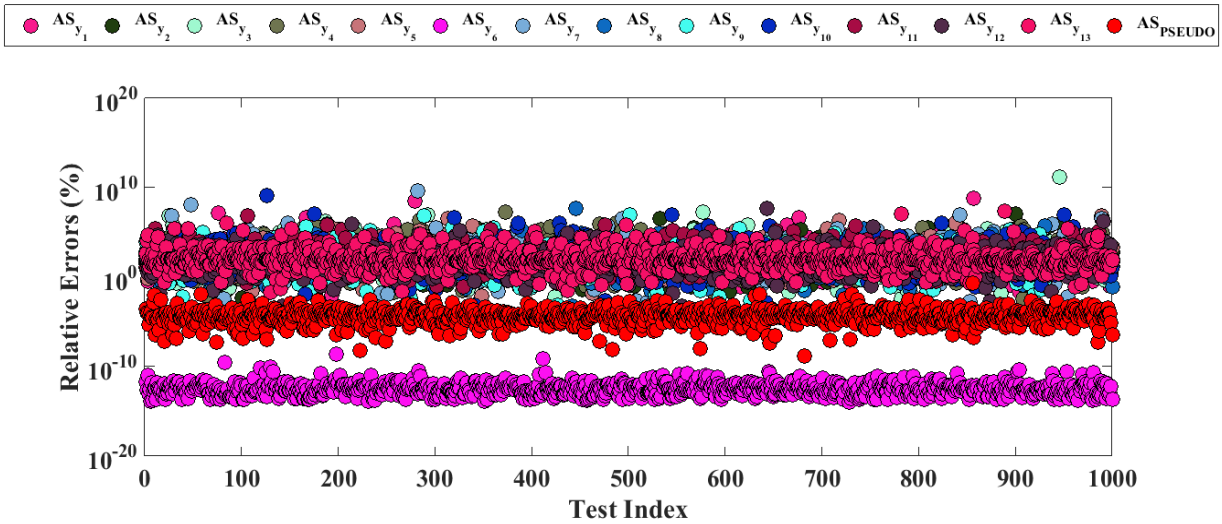

Fig. 4-43. Errors in y_6 due to projection onto all subspaces.

www.manaraa.com

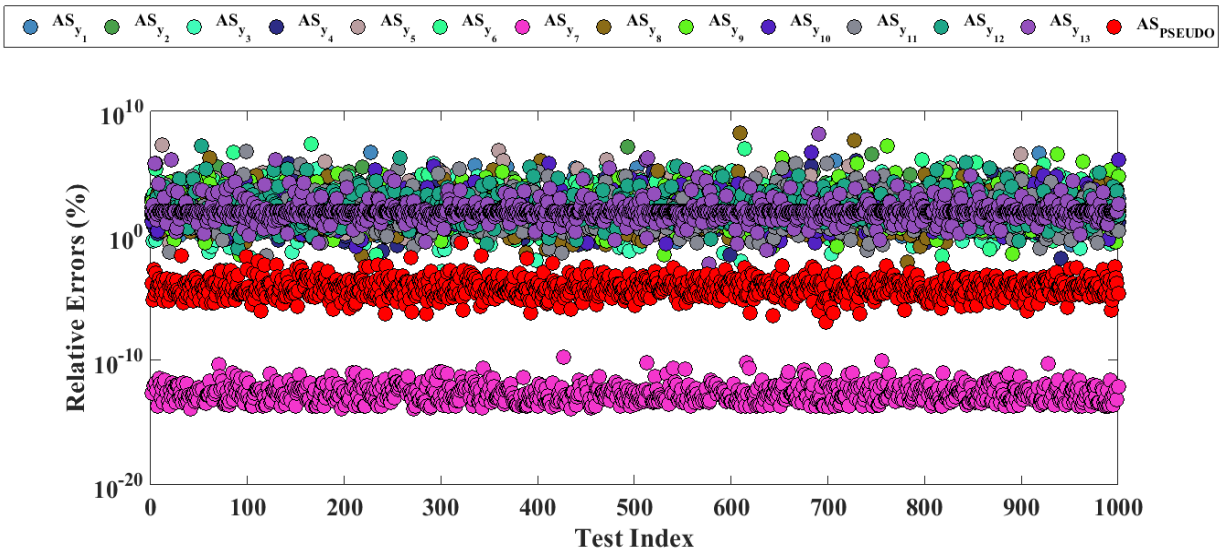

Fig. 4-44. Errors in y_7 due to projection onto all subspaces.

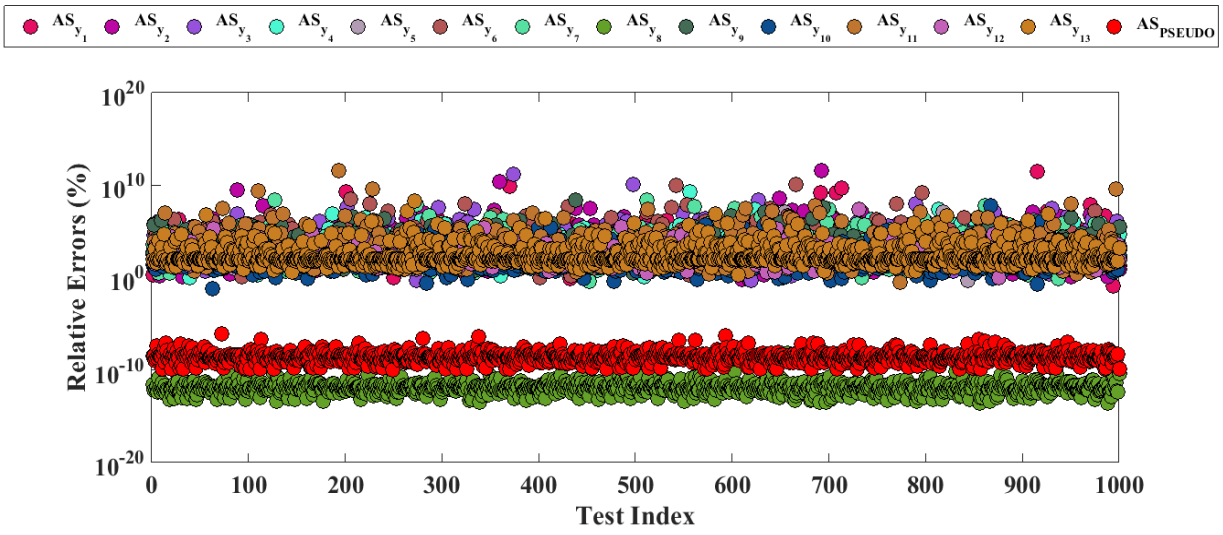

Fig. 4-45. Errors in y_8 due to projection onto all subspaces.

www.manaraa.com

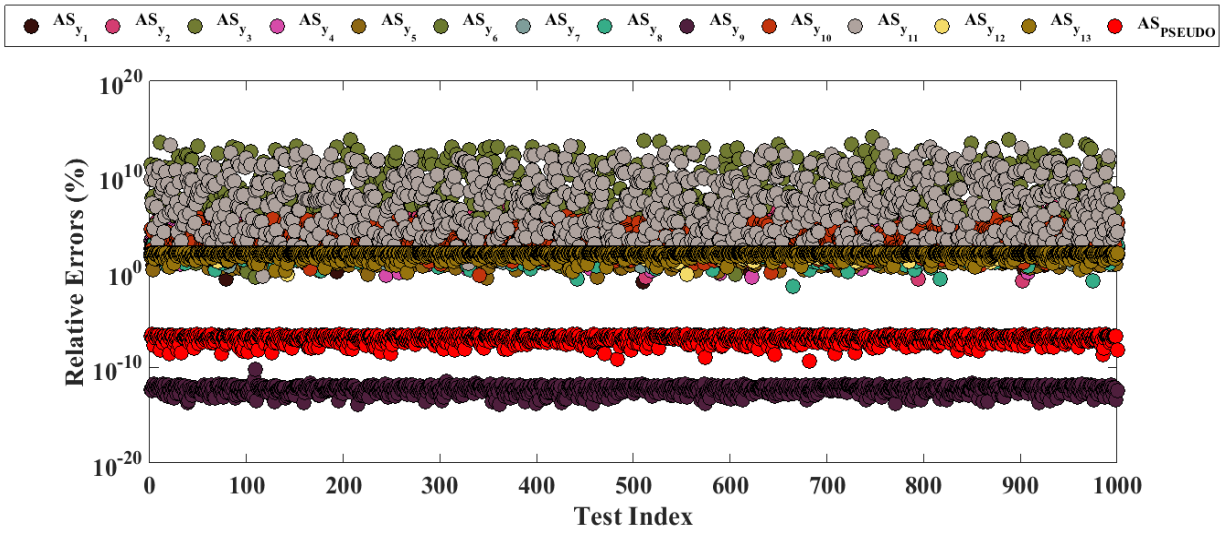

Fig. 4-46. Errors in y_9 due to projection onto all subspaces.

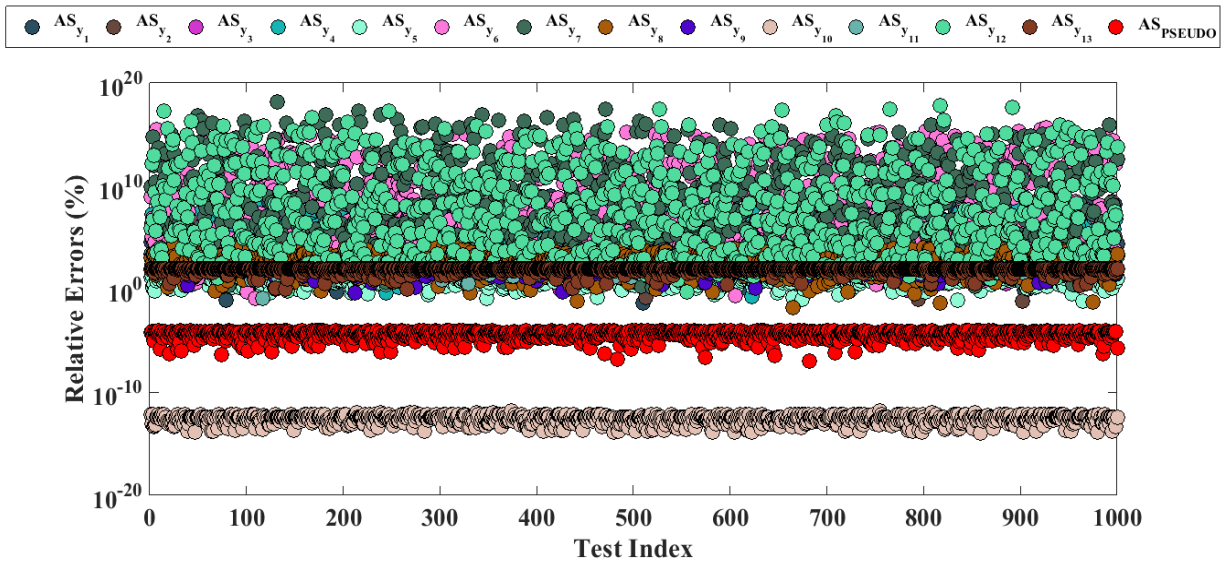

Fig. 4-47. Errors in y_{10} due to projection onto all subspaces.

www.manaraa.com

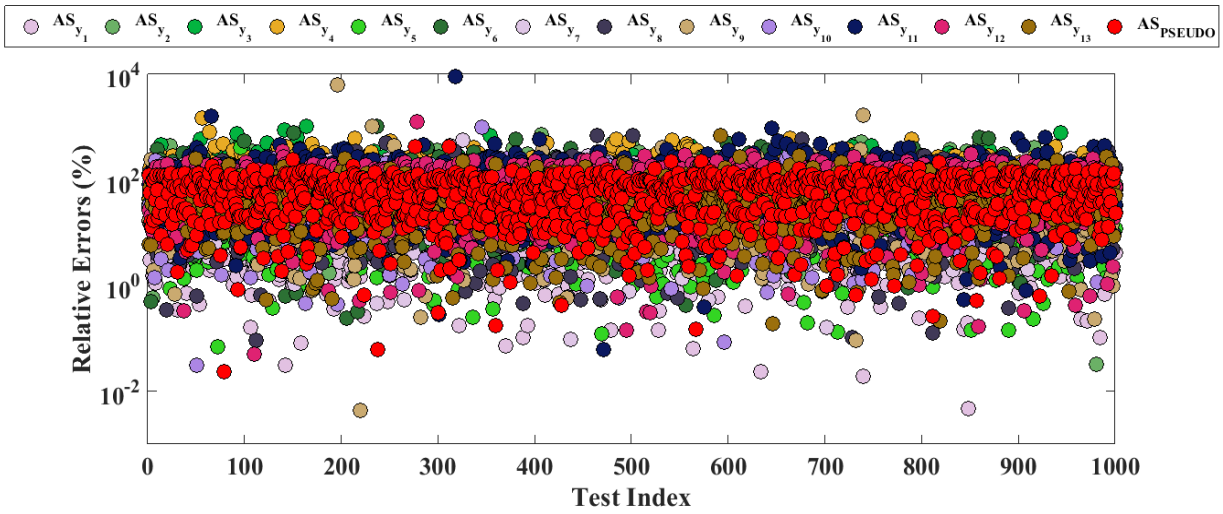

Fig. 4-48. Errors in y_{11} due to projection onto all subspaces.

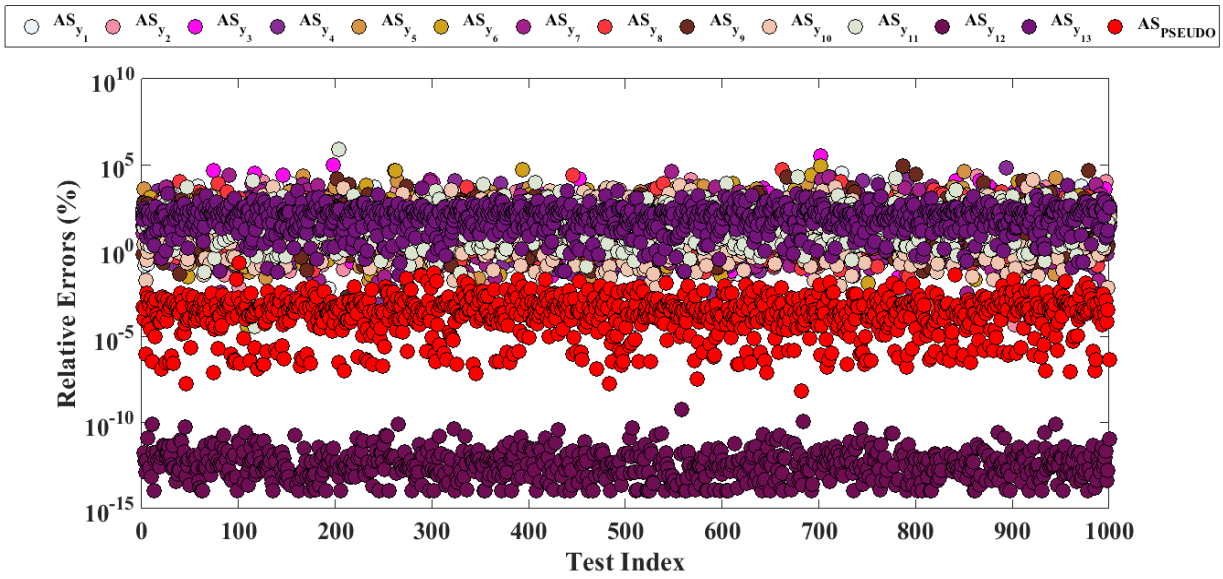

Fig. 4-49. Errors in y_{12} due to projection onto all subspaces.

www.manaraa.com

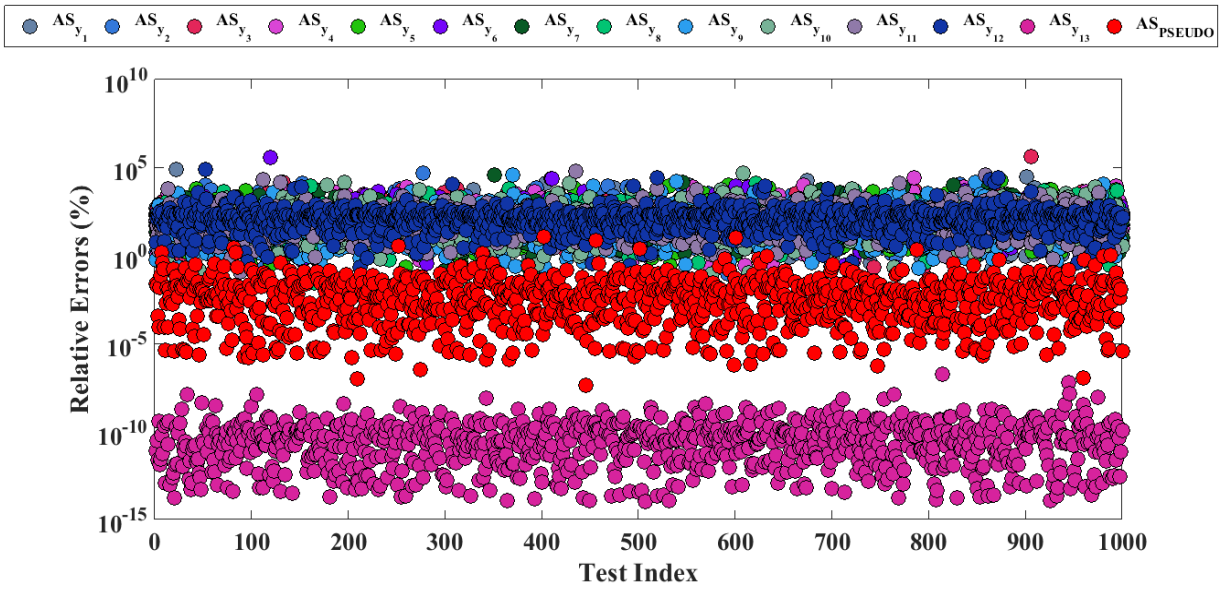

Fig. 4-50. Errors in y_{13} due to projection onto all subspaces.

From the previous figures and discussion, one can infer that although the subspace extracted from an individual response will lead to the least error for the given response, it will not be representative of other responses. On the other hand, the active subspace extracted via the pseudo response is representative of all responses and results in errors that are comparable to the single response active subspace. In other words, if we consider the whole problem (i.e., all the responses), we will find that the pseudo-response-based-subspace outperforms the individual active subspaces for the same size. Of course, one can take that to the next level and solve an optimization problem to get the optimum weights b_{opt} such that $R^{pseudo} = b_{opt}^T y$ minimizes the error for that subspace size. This is beyond the scope of this work, especially that the subspace captured by the random pseudo-response gives an acceptable error. This conclusion can be tested if all the active subspaces are plotted and the relative position or angles are visualized. One obstacle is the high dimensionality of the subspaces. For illustration, we show the first three

www.manaraa.com

components of the active subspace in Figure 4-51. The figure supports this conclusion and hence defends the claim that the pseudo response is an essential entity in identifying the active parameter subspace for vector-valued functions especially when the number of responses is as large as nuclear reactor applications, this number is typically in the order of 10^4-10^6 which means that to get the parameter subspace one needs to find 10^4-10^6 active subspaces and then somehow aggregate them to find a single active subspace which is impractical in reactor physics applications. Fig. 4-51 illustrates few of the active subspaces with the red subspace places such that it gives the minimum error among all the active subspaces as shown in the former figure.

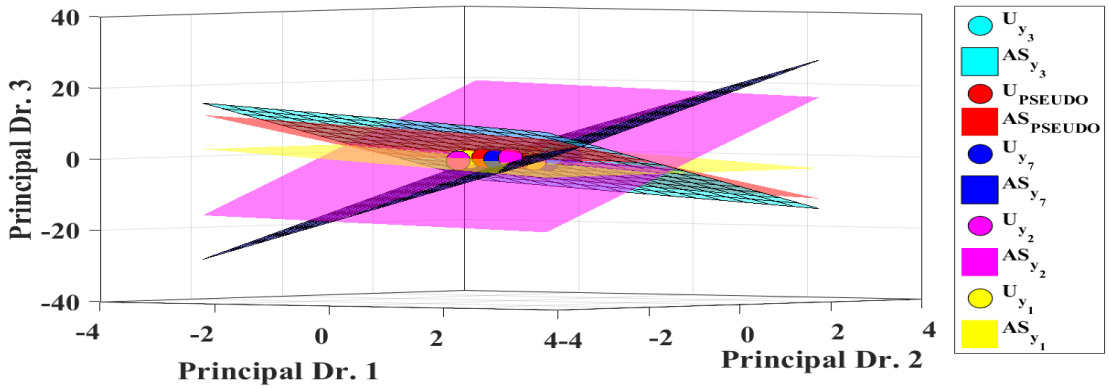

Fig. 4-51. Active Subspaces from individual responses and from the pseudo response(showing only the first 3 principal directions).

4.5.3 Case Study 3: Propagation of Error Bounds.

This case study aims to employ the estimator to construct error bounds due to reduction at different interfaces, for this purpose a PWR UO_2 pin cell model is engaged in a three steps test where the reduction is performed at the parameter level, then on the state level then both. A PWR UO_2 pin cell is depleted to (3.0 GWd/MTU) and is used as the reference on which the active subspace extraction is based. For that purpose SCALE 6.1 [49] is used, sequences like t-

www.manaraa.com

depl, t-newt and tsunami-2d are needed for depletion, neutronics, and sensitivity analysis respectively.

The original parameter space contains 7 nuclides * 2 reactions * 238 energy groups = 3332 parameters, whereas the nominal dimension of the response space is 238 representing the material flux at 238 energy group. As usual, the probability of failure is intentionally picked to be huge (10 %) which gives room for some failures to occur. After making a statement about the probabilistic error bound for this case and extracting the active subspaces, these subspaces are then tested in completely different conditions. The goal here is to check if the 3.0 GWd/MTU was the proper point for designing our spaces? Are the spaces capturing all the expected physics? Shall they behave as good when the some of the conditions change, (say temperature for instance)? And most importantly, will the error bound act as an alarm for the user to direct him to go sample the active spaces at different conditions or even advise him to add more directions to his so-called "important directions" spanning the active space? Motivated by these questions another case is employed, this time, the initial composition came from a depletion of 24 GWd/MTU and at room temperature.

Next Figures. 4-52 through 4-59 display the results due to reductions in parameter and/or response spaces. In the odd-numbered figures, the response is the total collision rate in the energy range 1.85 to 2.35 MeV. The even figures show the same response but in the thermal range between 0.975 and 1.0 eV. We use these small ranges to depict the power of the reduction in capturing localized responses. In each of the figures, the left graph compares the actual error resulting from the reduction to the error bound calculated from Eq. (4.13). The 45-degree solid line indicates the limit of the failure region, i.e., when the actual error exceeds the bound

www.manaraa.com

predicted by the theory. The right graphs show the actual variation of the response due to a random perturbation of 30% in the parameters.

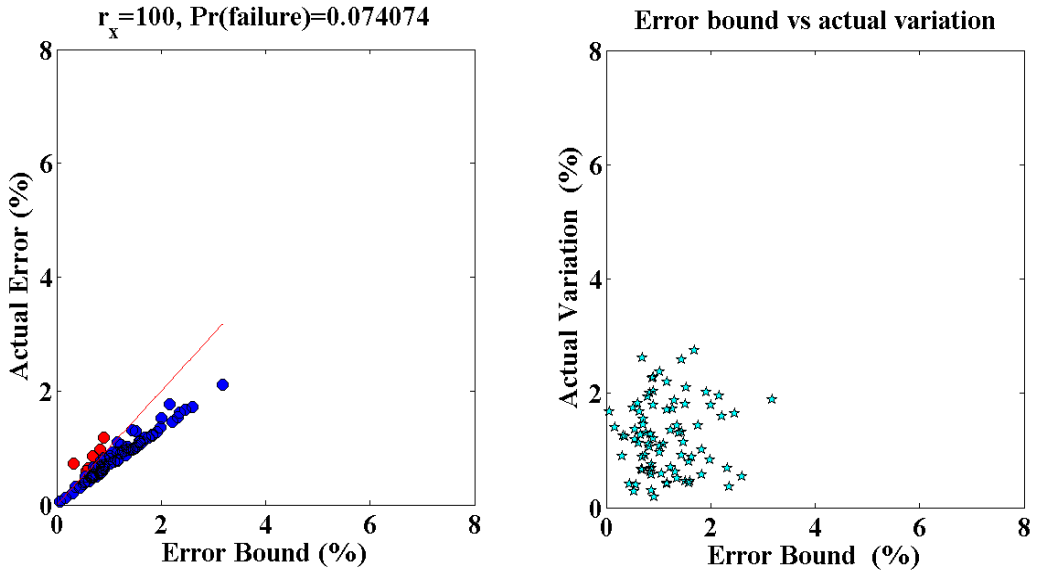

Fig. 4-52. Fast Collision Rate Errors – Parameter Reduction Only.

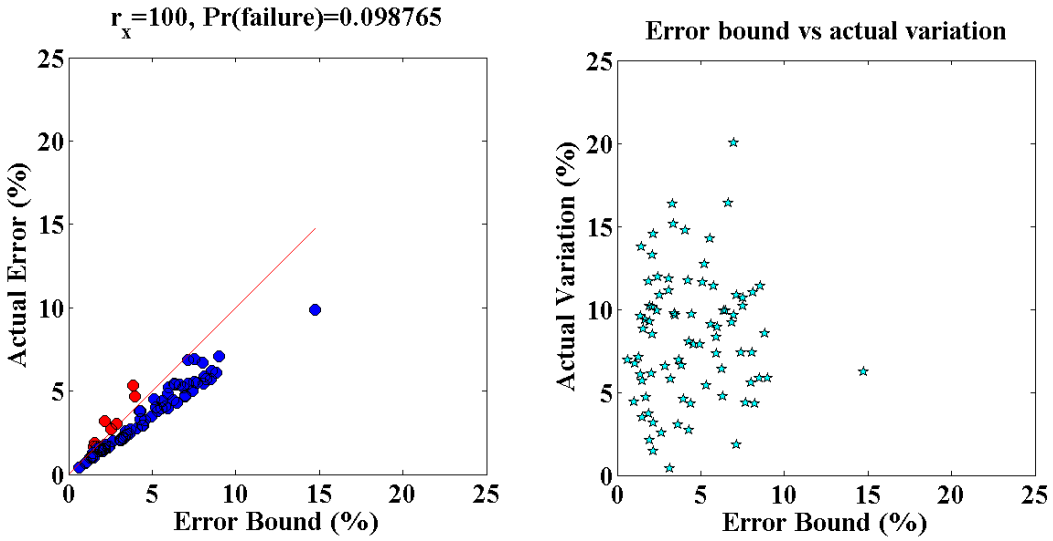

Fig. 4-53. Thermal collision rate errors – parameter reduction only.

www.manaraa.com

Figures 4-52 and 4-53 show a parameter-only-based reduction, meaning that the reduction is rendered in the parameter space. Both the level of reduction in terms of the rank of the active parameter subspace r_x and the actual probability of failure are shown on the top of the right graph. The reader should remember that we picked *s* and the multiplier in eq. (4.13) such that the probability of success is 0.9. In reality, *s* is picked to be 5 which results in a probability of success of 99.999%. Figs. 4.54 and 4.55 employ response-based reduction only, implying no reduction in the parameter space. The rank of response active subspace r_y is indicated in a similar manner.

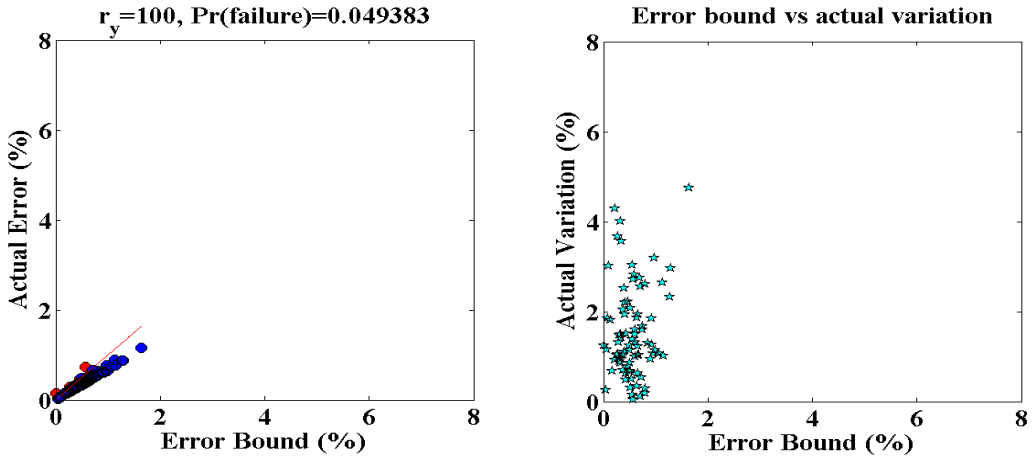

Fig. 4-54. Fast Collision Rate Errors – Response Reduction Only

www.manaraa.com

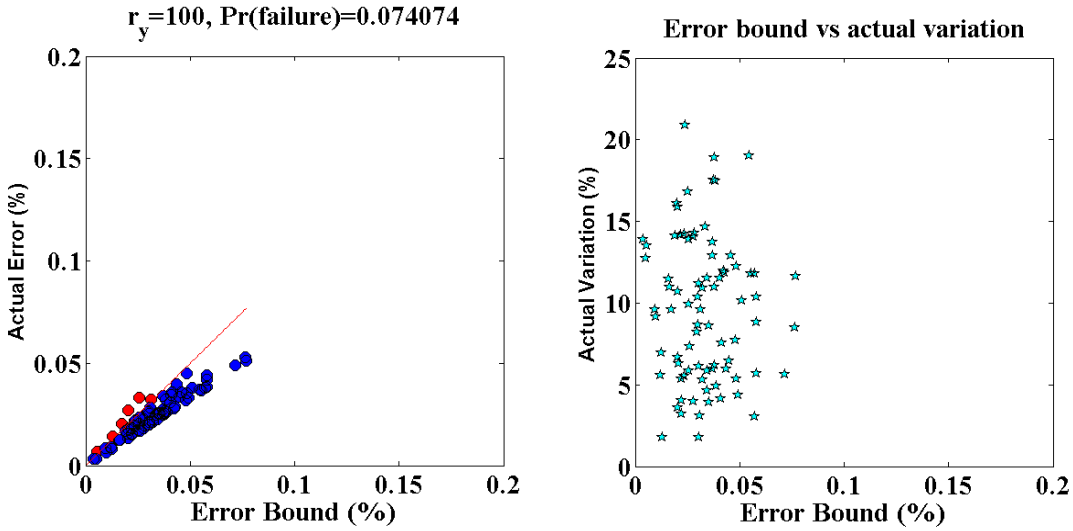

Fig. 4-55. Thermal Collision Rate Errors– Response Reduction Only.

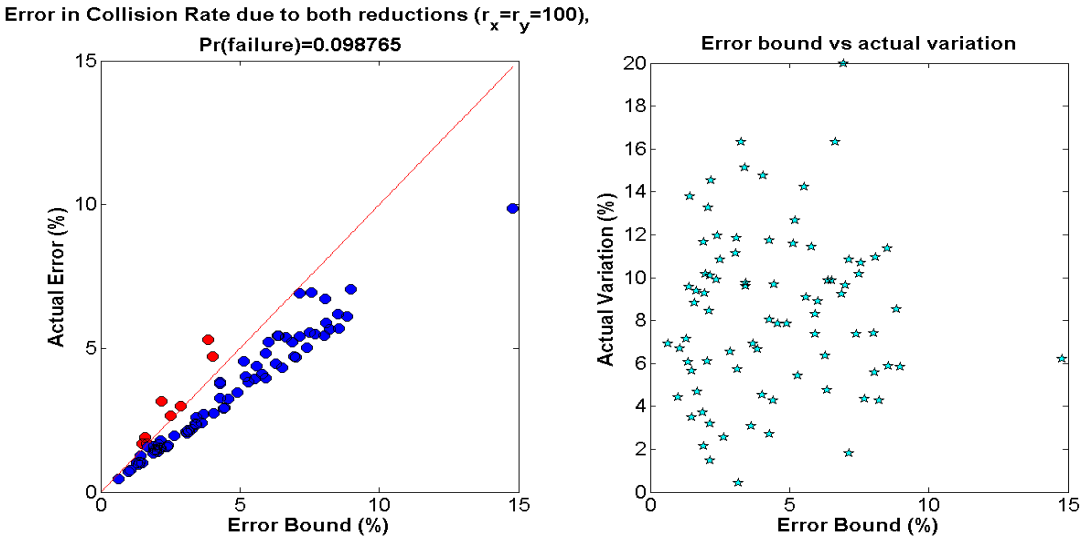

Fig. 4-56. Fast Collision Rate – Both Reductions.

www.manaraa.com

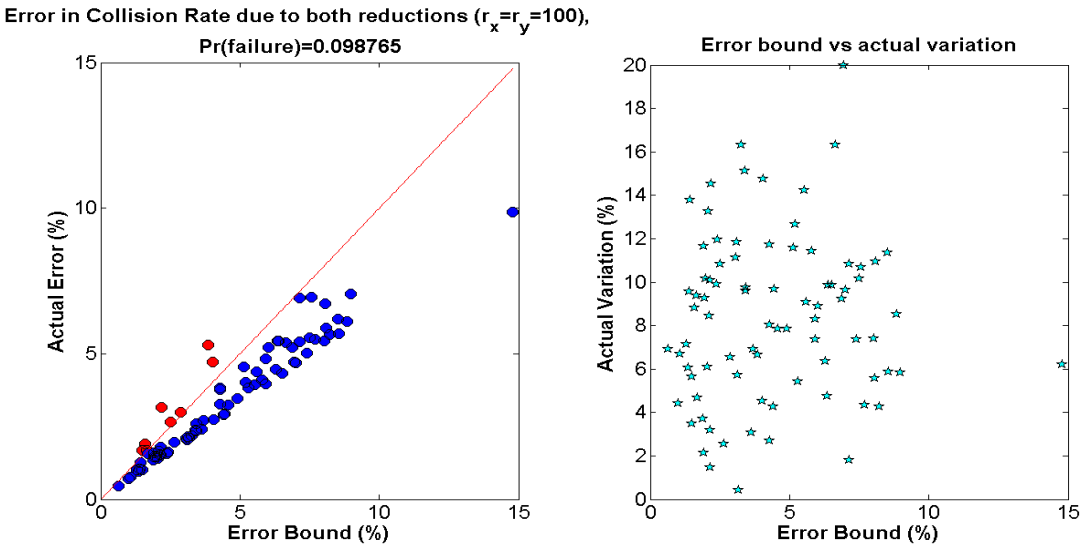

Fig. 4-57. Thermal Collision Rate -Both Reductions.

The previous six figures are for a 3 GWd/MTU depleted pin cell used to construct the bounds, notice that the reduction errors calculated will depend on whether the parameter-based reduction captures the important parameter directions that control the model response variations. Moreover, the response reduction, if not captured correctly, will miss directions along which the response is expected to vary. This situation will be clearer when we consider different physics conditions as done in the next case study.

Next, the following six figures employ the active subspaces extracted from the previous reference model to predict the response variations at different physics conditions. We employ a 24 GWd/MTU depleted fuel simulated at cold conditions. This emulates the effect of starting up a reactor with a once-burned fuel.

Figs. 4-58 through 4-63 correspond respectively to Figs. 4-52 through 4-57, where now the model is being evaluated at different physics conditions, using the reduction results from the previous case study, i.e., same ranks for parameter and response spaces, same responses, and

www.manaraa.com

same size of parameter perturbations. The idea here is to check whether the model reduced at hot conditions could be employed at sufficiently different physics conditions.

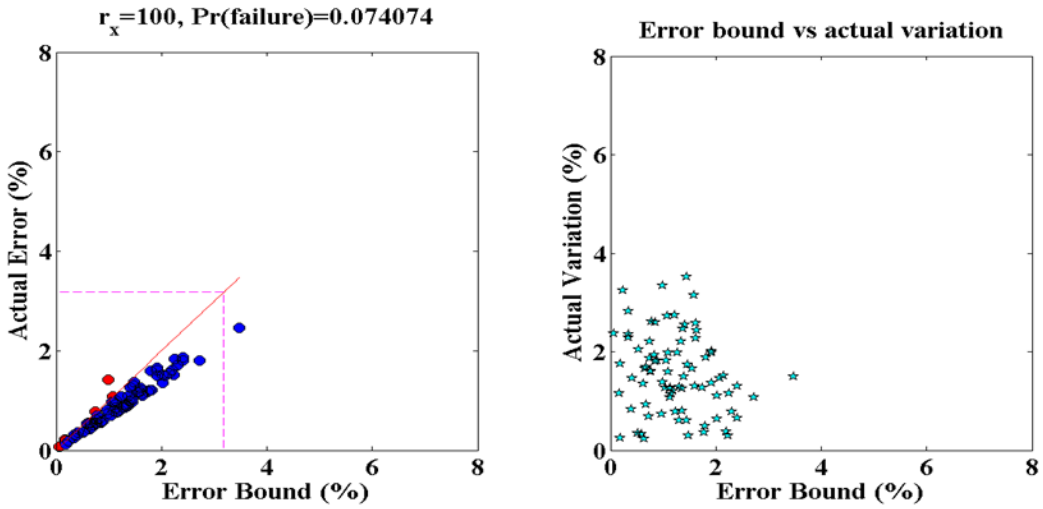

Fig. 4-58. Fast Collision Rate Errors - Parameter Reduction Only.

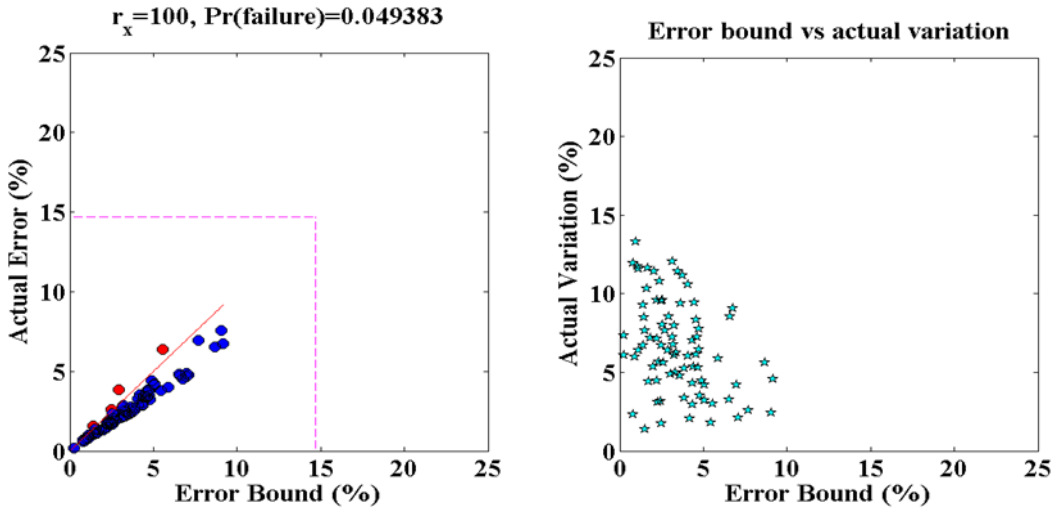

Fig. 4-59. Thermal Collision Rate Errors - Parameter Reduction Only.

www.manaraa.com

Figs. 4-58 and 4-59 show that the actual errors and the predicted bounds due to the parameter reduction are slightly higher than the errors in figs. 4-52 and 4-53. This indicates that the active subspace extracted using the reference model have approximately the same level of accuracy at new physics conditions.

Figs. 4-60 and 4-61 behave in a different fashion, where now results indicate that the actual errors and their bounds have noticeably increased beyond those in Figs. 4-54 and 4-55. This indicates that the responses at the new physics conditions are changing along new directions in the response space that are not captured by the reference physics models. Also, notice that in all cases, the actual probability of failure is always less than the theoretical value of $1\text{-}10^{-s}$.

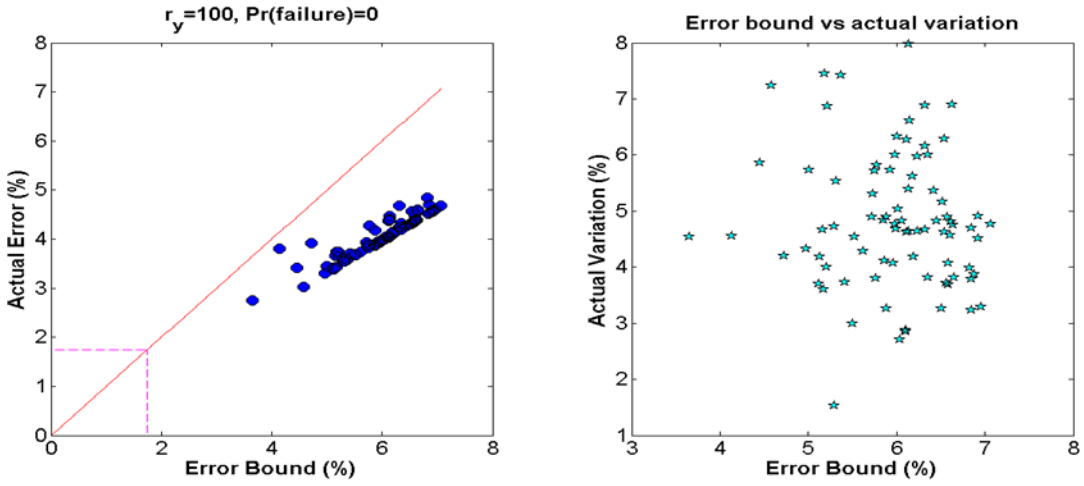

Fig. 4-60. Fast Collision Rate Errors - Response Reduction Only.

www.manaraa.com

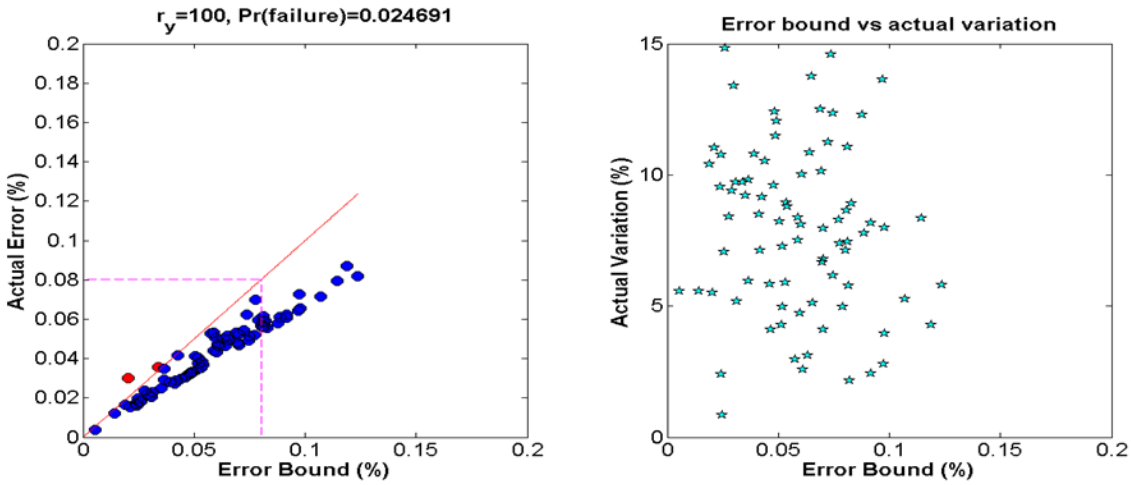

Fig. 4-61. Thermal Collision Rate Errors - Response Reduction Only.

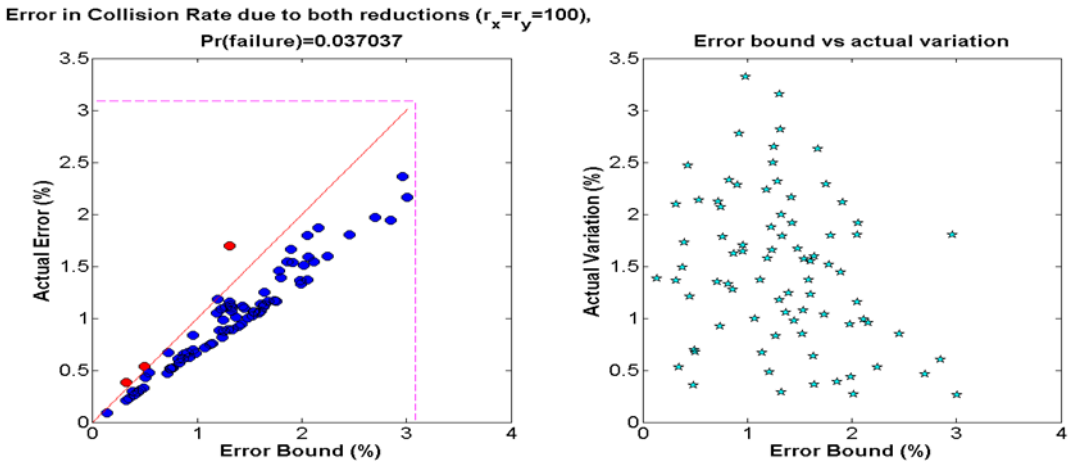

Fig. 4-62. Fast Collision Rate – Both Reductions.

www.manaraa.com

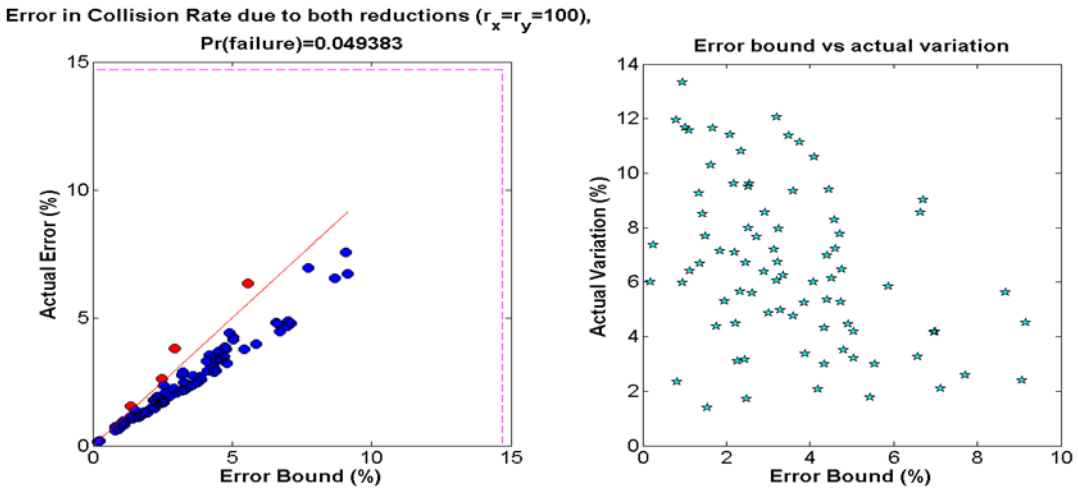

Fig. 4.63. Thermal Collision Rate – Both Reduction.

The following table shows a comparison between the reduction errors in case of parameter reduction, response reduction and simultaneous reductions for selective responses. The table shows that error bound for both reductions is greater than or equal to the sum of the two error bounds for each interface separately which numerically prove eq. (4.33).

www.manaraa.com

Table I. Errors at Different Reduction Interfaces.

Energy(eV)	Parameter Reduction (%)	Response Reduction (%)	Both (%)
1E-01-1.25E-01	3.440119127	1.96191E-07	3.440119194
5E-02-6E-02	3.349602423	2.0457E-07	3.349602447
6E-02 - 7E-02	3.955629492	1.97934E-07	3.955629436
7E-02 - 8E-02	3.7945243	2.53609E-07	3.794524287
4E-02 - 5E-02	3.44621065	1.9803E-07	3.446210638
1E-02-2.53E-02	4.188254639	1.21176E-07	4.18825466
8E-02 - 9E-02	3.453572923	3.03608E-07	3.453572969
3E-02 - 4E-02	3.902596376	1.47336E-07	3.902596405
9E-02 - 1E-01	3.433820983	2.47241E-07	3.433820863
1.25E-01-1.5E-01	3.526796356	2.4417E-07	3.526796456
2.53E-02-3E-02	3.752223964	9.76915E-07	3.75222389
1.5E-01-1.75E-01	3.70786145	1.63389E-06	3.707861774
1.75E-01-2E-01	3.445241801	4.65338E-06	3.44524029
7.5E-03-1E-02	5.357536753	1.0331E-05	5.357536306
2E-01-2.25E-01	3.952214865	1.43248E-05	3.952211457
5E-03-7.5E-02	7.886686911	1.28685E-05	7.886686507
2.25E-01-2.5E-01	3.352496404	5.18546E-05	3.352499921
4.0E-03-5.0E-03	7.322258969	0.000120071	7.322260748
2.5E-01-2.75E-01	3.620834966	0.00010714	3.620834811
3.0E-03 – 4.0E-03	7.887529058	0.000171297	7.887612678
2.75E-01- 3.0E-01	4.290836693	0.000178194	4.290871286
5.0E00- 5.4E00	3.563834792	0.002618404	3.564156127
3.0E-01 - 3.25 E-01	3.572903889	0.000407313	3.573024426
4.0E-01-4.5E-01	3.701153845	0.001769107	3.701377851
2.5E-03-3.0E-03	7.004411863	0.000816018	7.004288304
4.75E00-5.0E00	3.229780944	0.008471093	3.231645888
4.0E00-4.75E00	3.257848945	0.007573203	3.258867235
3.25E-01-3.5E-01	3.599056621	0.000905715	3.598498847
4.5E-01-5.0E-01	3.228058887	0.004004937	3.22862494
2.0E-03-2.5E-03	8.00777732	0.001022243	8.007345542
5.5E-01-6.0E-01	3.268039191	0.00951038	3.265611306
5.0E-01-5.5E-01	3.456567367	0.007802879	3.457179184
3.5E-01-3.75E-01	3.471976284	0.001599284	3.472051206
1.5E-03-2.0E-03	8.404778008	0.001760966	8.405178647
3.75E-01-4.0E-01	3.549323071	0.004358526	3.547520923
1.0E-03-1.2E-03	2.933508304	0.005250533	2.934386114
3.05E+02-5.5E+02	2.844417009	0.04124776	2.843561939
5.40E+00-6.00E+00	4.074100721	0.016322211	4.074944698
6.50E-01-7.00E-01	3.570617637	0.034846603	3.56734263
6.00E-01-6.25E-01	3.299556823	0.040263079	3.314687676

www.manaraa.com

Table I. Continued.

Energy(eV)	Parameter Reduction (%)	Response Reduction (%)	Both (%)
8.10E+00-9.10E+00	2.979535709	0.053468195	2.971807272
1.20E-03-1.50E-03	8.806732958	0.005031538	8.807632996
6.25E-01-6.50E-01	2.85300282	0.048711304	2.857971939
7.00E-01-7.50E-01	3.000604253	0.032137416	3.005533808
1.22E+02-1.86E+02	3.096156876	0.14700422	3.098386868
1.86E+00-1.94E+00	3.30643634	0.435769093	3.274282031
7.50E-04-1.00E-03	10.14884207	0.008543768	10.14911996
3.15E+00-3.50E+00	3.304932906	0.70442187	3.321994678
7.50E-01-8.00E-01	3.481919803	0.110131449	3.485124135
1.00E-03-1.20E-03	8.921925394	0.025576981	8.926885303
8.00E-01-8.50E-01	3.340759312	0.083782018	3.344441834
8.50E-01-9.00E-01	3.408852916	0.074667076	3.398109037
3.73E+00-4.00E+00	3.267999643	0.588855401	3.277918267
5.00E-04-7.50E-04	10.9842659	0.026901158	10.99812037
1.50E+00-1.59E+00	3.229417345	0.569922291	3.270350255
1.77E+00-1.86E+00	3.363233823	0.632339006	3.427290995
2.00E+00-2.12E+00	3.121457334	0.486267471	3.213677634
1.94E+00-2.00E+00	3.14323654	0.707228962	3.249938464
1.00E-04-5.00E-04	10.31416024	0.035525182	10.31480489
1.40E+00-1.45E+00	3.18535022	0.794470291	2.84917482
1.35E+00-1.40E+00	2.438763758	0.765872509	2.478244486
1.45E+00-1.50E+00	3.671618674	0.611078126	3.782569923
1.30E+00-1.35E+00	3.454533038	0.416090082	3.651712544
3.50E+00-3.73E+00	3.175719636	1.04835234	3.025468598
1.68E+00-1.77E+00	3.158062497	0.459241369	3.082581375
1.59E+00-1.68E+00	2.979590178	0.673087997	2.840554963
1.15E+03-1.50E+03	3.228473236	0.949831745	3.528308305
6.83E+02-9.50E+02	3.25350879	0.563854646	3.326281454
1.44E+01-1.51E+01	3.971263281	0.36431594	4.037361159
1.38E+01-1.44E+01	3.416538128	0.7029957	3.3529768
1.25E+00-1.30E+00	3.460826456	0.370328831	3.320335018
8.20E+01-9.00E+01	3.616811469	1.051309343	3.766329772
2.57E+00-2.67E+00	5.429779234	0.113663378	5.472640915
1.70E+01-1.85E+01	3.585454991	1.220966558	3.756504833
1.00E+01-1.15E+01	3.766336589	0.880316917	3.699577556
2.67E+00-2.77E+00	5.36234571	0.09530898	5.350362995
2.47E+00-2.57E+00	3.686998979	1.120642066	3.926400591
3.90E+03-6.00E+03	2.938200081	0.994489016	3.003289723

www.manaraa.com

Table I. Continued.

Energy(eV)	Parameter Reduction (%)	Response Reduction (%)	Both (%)
1.85E+06-2.35E+06	3.176916754	1.745885613	3.087929813
3.00E+06-4.30E+06	3.219765218	1.536677144	4.01260657
1.50E+06-1.85E+06	3.208845536	1.238970135	3.333488129
9.10E+00-1.00E+01	3.008185386	0.831895875	2.921320334
2.40E+02-2.85E+02	3.280331754	1.461150385	3.348388236
9.00E-01-9.25E-01	5.900216027	0.217383742	5.84683601
2.00E+05-2.70E+05	3.175679906	0.380489859	3.12146127
9.00E+01-1.00E+02	3.302432797	0.799491871	3.336966003
1.70E+04-2.50E+04	3.162743498	0.598742178	2.929230334
2.12E+00-2.21E+00	3.05428968	0.411605753	3.118420389
6.00E+00-6.25E+00	4.832544945	0.171753354	4.795208137
2.38E+00-2.47E+00	2.72963177	0.77101732	3.013134903
2.10E+02-2.40E+02	3.282014086	1.783145197	4.011639266
2.48E+06-3.00E+06	3.220309362	1.920806293	2.831543032
9.50E+02-1.15E+03	3.033028898	1.357191091	2.742660931
9.25E-01-9.50E-01	6.634054631	0.205969842	6.698071554
3.00E+04-4.50E+04	3.067794821	0.60935555	2.792272436
1.50E+05-2.00E+05	3.178987788	0.448914218	3.10929216
2.21E+00-2.30E+00	2.666092295	0.517205142	2.675728758
5.50E+02-6.70E+02	3.388384206	1.817784541	3.976954492
2.77E+00-2.87E+00	3.064841491	2.00378162	3.143030632
1.19E+01-1.29E+01	3.018142829	1.225637723	3.303674481
2.70E+05-3.30E+05	2.972939308	0.395030859	2.90421054
2.25E+01-2.50E+01	3.230008405	1.376279935	3.236231644
3.18E+01-3.33E+01	3.415804606	1.037478497	3.254078748
9.50E-01-9.75E-01	6.682313603	0.191869864	6.70300759
2.30E+00-2.38E+00	3.036527504	0.510561599	3.093250825
3.30E+05-4.00E+05	3.159357046	0.319790829	3.110190193
6.00E+03-8.03E+03	2.987608679	0.997613659	2.890946699
9.50E+03-1.30E+04	3.153772264	0.644871842	3.382349245
2.87E+00-2.97E+00	3.381593419	0.609806148	3.318457369
4.10E+01-4.24E+01	3.630283599	2.251093178	3.060625834
9.75E-01-1.00E+00	14.67190246	0.080256984	14.69449436
5.34E+01-5.90E+01	2.995121721	0.945342045	2.945282552
1.80E+03-2.20E+03	3.221452043	1.049650986	3.499907353
1.51E+01-1.60E+01	3.244212774	0.713549379	3.324859705
1.23E+00-1.25E+00	4.120721904	0.592750393	4.103246268
1.15E+00-1.18E+00	6.757476819	0.188408885	6.786055278
2.75E+01-3.00E+01	2.98640029	0.70862293	2.81875584
1.18E+00-1.20E+00	5.51424824	0.592085803	5.353111832

www.manaraa.com

Table I. Continued.

Energy(eV)	Parameter Reduction (%)	Response Reduction (%)	Both (%)
1.20E+00-1.23E+00	6.519062845	1.032079949	6.787587662
1.00E+05-1.28E+05	3.106382777	0.379456487	2.907653351
3.05E+00-3.15E+00	3.156117489	0.640844263	3.110611465
3.00E+03-3.74E+03	2.959276793	1.26489337	3.143872342
1.29E+01-1.38E+01	2.780480768	0.893004549	2.794946277
2.85E+02-3.05E+02	3.414493735	2.186812974	4.33111915
1.60E+01-1.70E+01	3.026020104	0.926802482	3.141075316
2.50E+01-2.75E+01	3.276564717	0.855370687	3.044203329
6.25E+00-6.50E+00	7.718007084	0.159837643	7.743665695
6.00E+05-6.70E+05	3.111038929	0.379657044	3.103192322
7.50E+05-8.20E+05	3.138093844	0.473529887	3.047403204
1.30E+04-1.70E+04	3.040135793	0.841119545	3.057165875
6.79E+05-7.50E+05	3.087013798	0.441131027	2.957487678
1.55E+03-1.80E+03	3.485925075	1.597105019	3.580792575
4.24E+01-4.40E+01	3.110838432	0.407541857	3.032197577
2.10E+01-2.25E+01	3.972201745	0.673281038	3.89828236
2.58E+03-3.00E+03	3.059333736	1.03751009	3.045309668
1.93E+02-2.08E+02	3.945704236	2.392708959	3.052332647
4.40E+01-4.52E+01	3.063421027	1.343540369	3.088322646
3.96E+01-4.10E+01	3.476759919	1.156999111	3.555916767
1.00E+02-1.08E+02	3.786351292	1.133611191	3.766836025
5.00E+05-5.50E+05	2.771590123	0.329781379	2.769015993
6.00E+04-7.30E+04	3.168675541	0.422676647	3.004628167
6.75E+01-7.20E+01	3.072821349	0.688226534	2.882766621
1.10E+06-1.20E+06	3.215990021	0.418189124	3.039951691
7.20E+01-7.60E+01	2.931155169	1.204872421	2.984211672
1.28E+05-1.50E+05	3.206134953	0.388075407	3.176003786
1.19E+02-1.22E+02	3.422767266	0.629001011	3.326796352
1.08E+02-1.15E+02	3.317528966	0.638192322	3.366936099
8.50E+04-1.00E+05	3.143749013	0.339079111	3.038985281
3.00E+01-3.13E+01	3.07794049	0.70222597	3.16283641
8.03E+03-9.50E+03	3.031021515	0.728528284	3.104140285
1.90E+01-2.00E+01	4.133089518	4.090490463	4.511339704
2.29E+03-2.58E+03	2.821658604	1.291395743	3.117001558
9.20E+05-1.01E+06	3.249781302	0.376999228	3.209337868
2.50E+04-3.00E+04	3.352517707	0.657106035	3.054070866
4.80E+06-6.43E+06	3.217052189	2.319122544	3.679142251
7.60E+01-8.00E+01	2.864366502	0.407879056	2.919077853
6.10E+01-6.50E+01	2.822762656	1.340351087	2.768349664
1.40E+06-1.50E+06	3.220109072	0.782115017	3.325465953

www.manaraa.com

Table I. Continued.

Energy(eV)	Parameter Reduction (%)	Response Reduction (%)	Both (%)
1.01E+06-1.10E+06	2.850855869	0.349376802	2.79422865
7.00E+00-7.15E+00	8.589577168	1.104430241	8.610117229
4.52E+01-4.70E+01	2.9472128	0.403652145	2.950077916
1.85E+01-1.90E+01	2.743295308	2.218707703	3.38546367
2.00E+01-2.10E+01	6.313389666	0.715807596	6.487809101
5.20E+04-6.00E+04	3.189945148	0.473294298	3.047901321
3.00E+00-3.05E+00	3.328896003	0.560353476	3.322918572
1.86E+02-1.93E+02	3.484060881	3.379121918	4.520543885
3.33E+01-3.38E+01	3.449448095	1.525843365	3.991197516
1.15E+01-1.19E+01	3.627915331	2.494369694	3.678287139
8.20E+05-8.61E+05	3.19292962	0.384499932	3.149225937
2.35E+06-2.48E+06	3.116400309	1.884333592	3.361530738
1.13E+00-1.14E+00	16.06272664	1.012493116	15.96943342
1.14E+00-1.15E+00	13.1215594	1.332576348	12.91629698
5.90E+01-6.10E+01	3.259753985	1.062406668	3.171443628
1.12E+00-1.13E+00	19.25408896	0.823583447	19.19507661
1.11E+00-1.12E+00	28.40826643	0.73792133	27.70563315
1.00E+00-1.01E+00	29.54845937	0.556872689	29.42842751
1.25E+06-1.32E+06	3.176745292	0.406012148	3.172296959
1.10E+00-1.11E+00	25.29329731	0.774812724	25.47794365
3.80E+01-3.91E+01	3.922997667	3.947742267	4.614513315
4.70E+05-5.00E+05	3.045699092	0.373784125	3.021491526
1.01E+00-1.02E+00	33.59576825	0.387101223	33.58409846
1.09E+00-1.10E+00	33.95068191	0.428600223	33.85923349
1.02E+00-1.03E+00	32.50851034	0.411412637	32.42343229
1.08E+00-1.09E+00	32.30224322	0.61779347	32.44405121
1.03E+00-1.04E+00	33.12480181	0.577589705	33.03925809
1.07E+00-1.08E+00	33.98903723	0.54448215	33.95319308
3.91E+01-3.96E+01	3.70884527	1.822419546	4.009509314
1.05E+00-1.06E+00	34.14680566	0.586645806	34.30480535
1.04E+00-1.05E+00	36.22793192	0.58966325	36.16242968
1.06E+00-1.07E+00	36.9548458	0.529419599	37.00397494
5.73E+05-6.00E+05	3.148913957	0.463502702	3.093421134
4.50E+04-5.00E+04	3.190552737	0.728944164	3.143101155
4.70E+01-4.83E+01	2.695623736	0.558037829	2.789307483
2.97E+00-3.00E+00	3.089020785	0.561902161	3.185111705
1.20E+06-1.25E+06	3.18827519	0.335803718	3.154405387
6.75E+00-7.00E+00	14.35002581	0.675049151	14.36852549
4.40E+05-4.70E+05	3.203942912	0.350165622	3.139106614
4.30E+06-4.80E+06	2.851389668	2.397640085	3.502489547

www.manaraa.com

Table I. Continued.

Energy(eV)	Parameter Reduction (%)	Response Reduction (%)	Both (%)
7.50E+04-8.20E+04	3.019653098	0.49038035	2.927516098
5.06E+01-5.20E+01	2.947144339	0.864449708	3.024941283
5.50E+05-5.73E+05	2.949834038	0.41911658	2.977260384
3.70E+01-3.80E+01	10.15670657	2.414522085	10.12591683
5.20E+01-5.34E+01	2.982918243	1.505588734	3.468357397
4.92E+01-5.06E+01	3.021375114	0.745479296	3.002005079
6.50E+01-6.75E+01	6.177972558	2.480591822	6.278510841
1.36E+06-1.40E+06	3.174124473	0.580356312	3.095144704
4.00E+05-4.20E+05	3.217378809	0.31385384	3.16663353
8.00E+01-8.20E+01	6.523370161	3.214616095	7.123052748
3.38E+01-3.46E+01	2.873542407	2.509087363	3.412715727
4.83E+01-4.92E+01	3.323443568	0.493222469	3.43098238
1.15E+02-1.19E+02	3.592186254	6.269392312	5.849618048
3.46E+01-3.55E+01	4.467109911	5.323014233	4.524150726
8.75E+05-9.00E+05	3.267598485	0.401438877	3.157889337
3.74E+03-3.90E+03	3.174379477	0.937937011	3.212323745
1.50E+03-1.55E+03	3.304687874	0.927158984	3.241155242
4.20E+05-4.40E+05	3.192573025	0.364518198	3.159269541
1.32E+06-1.36E+06	3.198147667	0.385882945	3.10516558
3.13E+01-3.18E+01	3.125820739	0.620673846	3.127160324
6.43E+06-8.19E+06	3.087081522	5.276383593	4.923731049
2.20E+03-2.29E+03	3.210812464	1.068281042	3.247702304
3.55E+01-3.70E+01	7.779992563	5.828968455	7.894776261
1.00E-05-1.00E-04	13.52273172	14.21245979	11.20261079
9.00E+05-9.20E+05	3.089582199	0.501323351	3.116603694
8.20E+04-8.50E+04	3.099841581	0.468170183	3.033782806
5.00E+04-5.20E+04	3.3158727	0.549254122	3.195619214
8.61E+05-8.75E+05	3.26386224	0.40454677	3.17831173
6.70E+02-6.83E+02	3.242498873	0.404983734	3.226443691
6.70E+05-6.79E+05	3.108524743	0.392184974	3.013186878
7.30E+04-7.50E+04	3.145353031	0.439195326	3.128320518
8.19E+06-1.00E+07	3.184262661	4.855364239	5.669018221
6.50E+00-6.75E+00	39.82442634	67.38295168	56.44445726
2.08E+02-2.10E+02	10.77085537	19.76873596	17.47878447
1.00E+07-1.28E+07	4.414708119	6.038002502	6.052646317
1.28E+07-1.38E+07	4.903521462	5.554203188	5.623117927
1.38E+07-1.46E+07	6.812689533	6.177168865	8.31239257
1.46E+07-1.57E+07	6.782327127	7.961462528	9.245218544
1.57E+07-1.73E+07	5.82694347	9.705894792	8.725912172
1.73E+07-2.00E+07	8.510243016	13.30405731	10.70046423

www.manaraa.com

Table I. Continued.

Energy(eV)	Parameter Reduction (%)	Response Reduction (%)	Both (%)
max	39.82442634	67.38295168	56.44445726
Mean	5.797226707	1.395116938	5.987287655

4.6 Conclusions:

The binomial estimator is presented and is compared to two of the most successful methodologies; the Averaged Small-Sample Statistical Estimator and the Subspace Statistical Estimator to estimate vector/matrix norms. The proposed distribution and numerical methodology defend the argument that we do not necessarily need to find an analytic closed form for the probability and that via numerical sampling from a binomial distribution one can find the multiplier necessary to give a user-defined probability of success. This enables the analyst to build a robust estimate that is much closer to the actual norm than the small-sample or the subspace estimator. Usually, these small-sample methods accept a multiplier of the order of 10-100 which gives an estimate that is within two order of magnitudes from the actual norm. The binomial distribution, on the other hand, gives an estimate that is within 1-2 from the actual norm. This relaxation in the bounds enabled the analyst to perform more reductions and reaches a probability of 0.99999 only with the cost of 5 additional matrix-vector multiplications. The binomial estimator has succeeded to outperform both versions of Small-Sample estimators in both aspects (i.e., giving the least multiplier for a fixed probability of success and the highest probability of success for fixed multipliers).

www.manaraa.com

The binomial distribution showed the tendency to pick non-conservative realistic bounds, furthermore it exhibits a linear structure around the failure fence determined by the 45-degree solid line in the estimated vs. actual norm plot revealing that even for failed cases, although the actual norm is greater than the estimated bound but they are so close to each other which lends robustness to the constructed bound. The reason for this behavior is the very low variance resulting from the squared components of the binomial random vector compared to other distributions. This low variance negates the divergence of the test points and explains the linear structure near the actual norm. This work motivates a more rigorous exploration for the binomial distribution and maybe analytical forms for the probability of success and how it does relate to the multiplier η. This is left for future work for the author has mainly focused on the applicability of the bound in real-world applications. Having such a reliable bound motivated the propagation of reduction errors due to reductions at different interfaces as shown in case study 3. This work has equipped previously developed ROM techniques with probabilistic error metrics that bound the maximum errors resulting from the reduction. Given that reduction algorithms can be applied at any of the various model interfaces, e.g., parameters, state, and responses, the developed metric effectively propagates the associated errors to estimate an error bound on the response of interest that efficiently predicts the total error due to reductions at different interfaces and thus can be generalized to loosely-coupled multi-physics problems.

www.manaraa.com

CHAPTER FIVE

DEVELOPMENT OF MULTI-LEVEL REDUCED ORDER MODELING METHODOLOGY (M_LROM):

5.1 Introduction

Over the past few decades, the vast majority of computational scientists have been heavily investing in the development of modeling and simulation techniques. Empowered by the exponential growth in computing powers, scientists continuously seek to improve their models by adding additional levels of details (i.e., employing fine-mesh, fine energy resolution, multi-phase analysis, tightly coupled multi-physics, etc.). Although these models are expected to improve the understanding of the physics and physical behaviors, and despite this noticeable increase in computing power, the performance of such high fidelity model is still handicapped by the overwhelmingly high computational cost, especially when computationally intensive analyses are of interest such as data assimilation, sensitivity analysis, uncertainty quantification and design optimization. To address this challenge, active subspace identification techniques can be applied to reduce the complexity of the original models thus help realize the goals of advanced modeling and simulation techniques.

Chapters 3 and 4 have shown that a small number of code runs can be used to reduce the effective dimensionality of the model interfaces. For example, using r_x adjoint runs can identify the active parameter subspace whereas using r_y forward runs is enough to capture the active response subspace, where r_x and r_y are the intrinsic dimensions of the parameter and response spaces respectively. While this basic approach proved valuable, and has been shown to reduce the dimensionality by several orders of magnitude for reactor physics calculations, it may not be

www.manaraa.com

enough to render ROM practical, especially when the intrinsic dimensionality of the models is too high, which is the case for extremely detailed models operating on leadership computing platforms. In this chapter, we explore an alternative approach to rendering a reduction that significantly reduces the cost of building an ROM when the execution of the full model either in the forward or adjoint model is computationally taxing. Specifically, we show that a lower fidelity model, i.e., one employing simpler physics model, or coarser mesh, can be used to render a reduction with comparable performance to that produced using the original high fidelity model. We refer to this methodology as multi-level ROM [108]

5.2 M_LROM Methodology

The general outcome of this methodology is that one may identify the active subspaces and thus render reduction for a high fidelity model by executing such model a number of times equal to *r* (the intrinsic dimensionality of the model's parameter and/or response spaces which is typically in the order of few hundreds of reactor physics models), this is several orders of magnitude smaller than the original dimensionality, which measures either the size of the state space (i.e., flux), the parameters (e.g., cross-sections), or responses (e.g., pin power distribution), all expected to be very large in dimensionality (typically in the order of 10^4-10^6 for reactor applications). Notwithstanding this significant reduction, few hundred runs of high fidelity codes remains impractical even on supercomputers. Multi-level ROM (M_LROM) is a new development in ROM, which allows one to extract the active subspaces by executing a low-fidelity model in lieu of the high fidelity model on a small sub-domain of the overall problem domain, (i.e., pin cell or 2D lattice vs. whole core, coarse mesh vs. fine mesh, homogenized material vs.

www.manaraa.com

heterogeneous media, collapsed energy structure vs. fine energy structure, etc.). The goal is to show that this approach is capable of capturing the important directions spanning the active subspaces without violating the error bounds constructed from employing the binomial estimator to the low fidelity model to establish realistic upper-bounds over the expected range of variations for the high fidelity model. Familiarity with the physics of the problem will help educating the choice of the sub-domain(s) used to represent the low-fidelity model.

5.2.1 Mathematical Description:

The M_LROM methodology can be mathematically described as follows: Consider the low-fidelity model:

$$y^{LF} = f^{LF}(x); \quad x \in \mathbb{R}^n, y \in \mathbb{R}^m$$

Let $\mathbf{U}_x^{(r)} \in \mathbb{R}^{n \times r_x}$ and $\mathbf{U}_y^{(r)} \in \mathbb{R}^{m \times r_y}$ be matrices containing the orthonormal basis of the active parameter and response subspaces then define the low-fidelity error operator:

$$[E^{LF}]_{ij} = \left| \frac{f_i^{LF}\left(x_j\right) - \mathbf{U}_y^{(r)}(i,:)\mathbf{U}_y^{(r)T}(i,:)\, f_i^{LF}(\mathbf{U}_x^{(r)}\mathbf{U}_x^{(r)T} x_j)}{f_i^{LF}\left(x_j\right)} \right| \tag{5.1}$$

Then an upper bound can be established using:

$$\varepsilon = \eta \max_{i=1,2,\cdots s} \left\| \mathbf{E}^{LF} w^{(i)} \right\| \tag{5.2}$$

This upper bound is then tested using the high-fidelity model:

www.manaraa.com

$$y^{HF} = f^{HF}(x);\ x \in \mathbb{R}^n, y^{HF} \in \mathbb{R}^M$$

with M is the whole domain response dimensionality whereas m is the sub-domain response dimensionality, i.e. $m \ll M$.

Then if the upper bound is less than a user-defined tolerance i.e. $\varepsilon \leq \varepsilon_{user}$ the same active subspaces extracted from the low-fidelity model are tested against the high-fidelity model:

$$[\mathbf{E}^{HF}]_{ij} = \left| \frac{f_i^{HF}\left(x_j\right) - \mathbf{U}_y^{(r)}(i,:)\mathbf{U}_y^{(r)T}(i,:)\, f_i^{HF}(\mathbf{U}_x^{(r)}\mathbf{U}_x^{(r)T}x_j)}{f_i^{HF}\left(x_j\right)} \right| \tag{5.3}$$

Satisfies that:

$$\mathbb{P}\left\{ \left\| \mathbf{E}^{HF} \right\| \leq \varepsilon \right\} \geq 1 - \left(p_f(\eta, \mathcal{D}) \right)^s \tag{5.4}$$

Following the developments in chapter 4, it is safe to state that the subspaces extracted from the low-fidelity model are representative of the high-fidelity model once eq. (5.4) is satisfied.

5.3 Numerical Experiments and Results

In this section, few tests are conducted moving from a 2x2 mini assembly model to a row of 15 pin cells in a PWR assembly arriving at a full 7x7 BWR model. Each time the choice of the low-fidelity model is an attempt to learn more about the physics and infer which low-fidelity model can capture most of the important directions spanning the active parameter subspace to efficiently represent the active subspace of the original high-fidelity model. It is undeniable that familiarity with the problem helps taking an educated decision about picking the low-fidelity model and conditions, but even if the user has no clues, she can always try different low-fidelity

www.manaraa.com

models and use the binomial estimator discussed in the former chapter to decide which low-fidelity model outcomes in a more representative active subspace.

5.3.1 Case Study 1: Bounding Coarse Mesh Finite Difference Acceleration (CMFD) Method:

One widely used acceleration technique in reactor computations is the coarse mesh finite difference method, where the spatial domain is broken into a coarser mesh leading sometimes to a significant reduction in execution time. Surprisingly enough this was never done to extract active subspaces and if so, the extracted subspace is used on the same coarse mesh. The contrary is true here where the low-fidelity model is the accelerated coarse meshed one which is used to extract the active subspace, then this subspace is examined on the original fine-mesh high fidelity model.

It worth mentioning that in such a small model the (CMFD) will not buy a lot of reduction in running time but the same idea can be projected on a full assembly model where one cannot afford running the high fidelity model enough times to identify the active subspace. This case studies the 2x2 PWR mini assembly model consists of 2 UO2 pin cells and 2 MOX pin cells [109]. Each pin cell is divided into 9x9 fine mesh to represent the whole fidelity model, a coarser mesh is considered to help accelerating the convergence of the model and hence, each 3 cells are taken to be 1 coarse cell and hence the low-fidelity model is the mini assembly with each pin cell divided into 3x3 cells. Figure 5.1 draws a picture of both models showing different mixtures.

www.manaraa.com

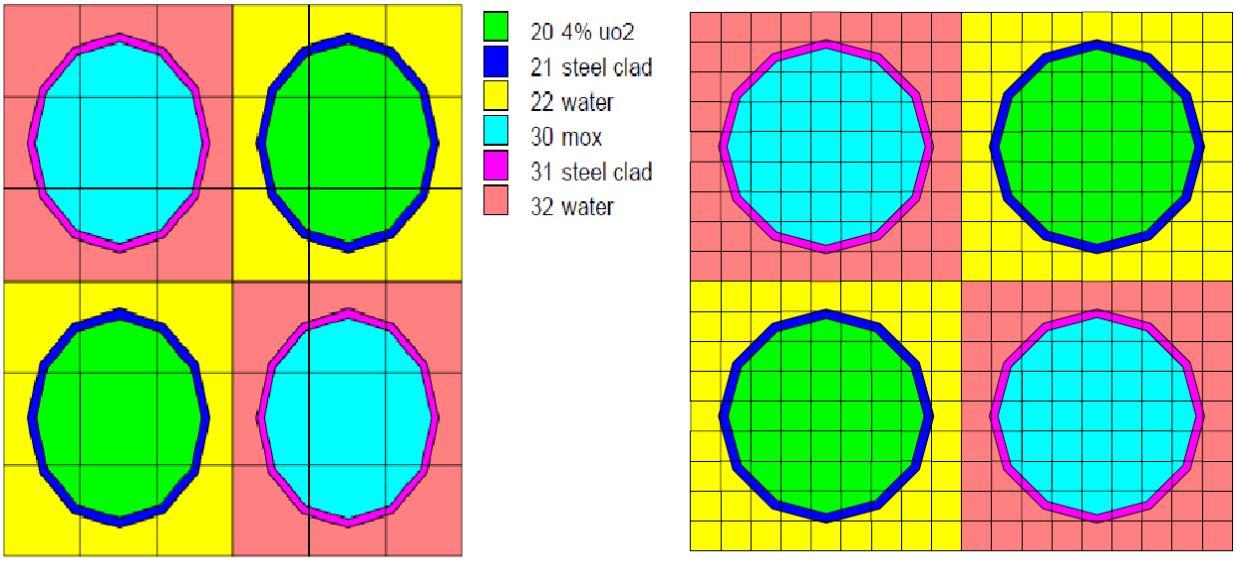

Fig. 5-1. 2x2 Mini PWR assembly. Left: Coarse Mesh (Low-fidelity model). Right: Fine Mesh (High-fidelity Model).

The original parameter space dimension is 176358 coming from 741 material-reaction pairs * 238 energy groups. For such high dimensionality, it is always a good idea to use reduced order modeling techniques which will require running the original model for at least a number of runs that is equal to the intrinsic dimensionality which from previous experience can be in the order of few hundreds. Meaning that one needs to run the high-fidelity model few hundred times to extract the active subspace, but instead, the low-fidelity model is employed for this goal. Once the active parameter subspace is identified the proposed binomial estimator is then used to build a prior error bound, then the containment of all important directions forming the basis for the active parameter subspace is assessed via the high-fidelity model to check whether it violate the error bound constructed previously by the binomial estimator.

www.manaraa.com

The low-fidelity model is depleted to different burnups and the one that gives the minimum error bounds declares the best active subspace. The responses of interest are taken to be the material flux at each of the 238 energy group. For the sake of illustration, the probability of failure is taken to be 15% (whereas in practice it is typically 0.001%). The reduced dimension is taken to be 800 dictating a cut off after the first 800 columns of the left singular vectors resulting from the singular value decomposition of the pseudo-response sensitivity profile as mentioned in chapter 3. The tests also reveal that the least error bounds and hence the best active subspace are captured when the reference case is depleted half way (30GWd/MTU) and at hot conditions.

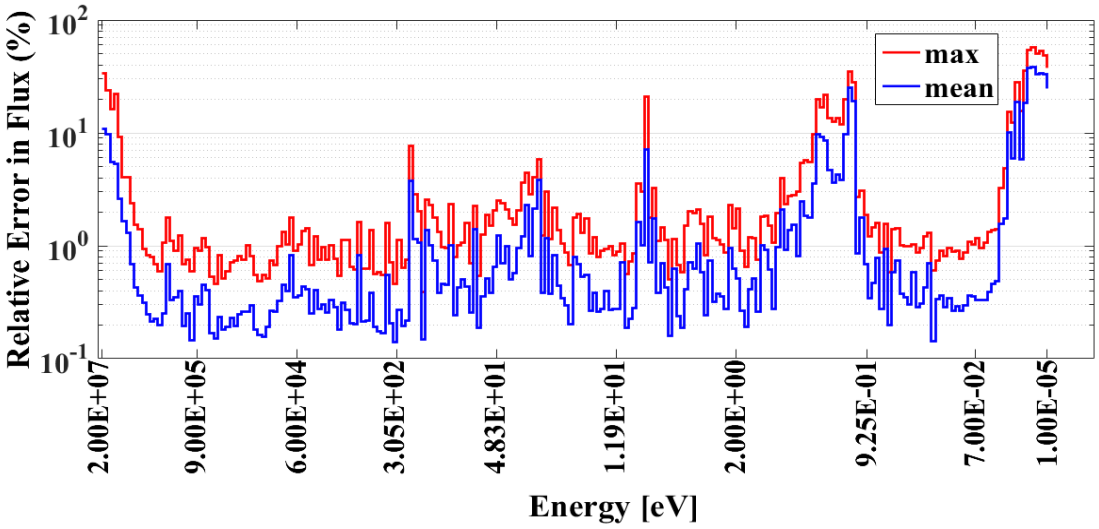

Fig. 5-2. Maximum and Mean Error Bounds for UO_2 flux.

Figures 5.2 and 5.3 give a list of 576 error bound (i.e., error bound for each material flux at each energy group). Assuming that these bounds are acceptable and that the energies of interest are those that gave errors that do not exceed 3% maximum error and 0.8% mean error.

www.manaraa.com

These should be tested on the high-fidelity model (fine mesh) to defend the claim that the active subspace gained from the low-fidelity model will not violate these bounds when the high-fidelity model is projected to this active subspace. (Note that it is known that the very first and last energy groups tend to give much higher errors and that's why in practice the responses of interest are typically taken to be reaction rates instead of flux). However, if the user did not accept the error bounds on the low-fidelity model, she either has to increase the size of the subspace or sample the basis in different condition, say more dominant conditions such as different burnups, temperatures, etc.

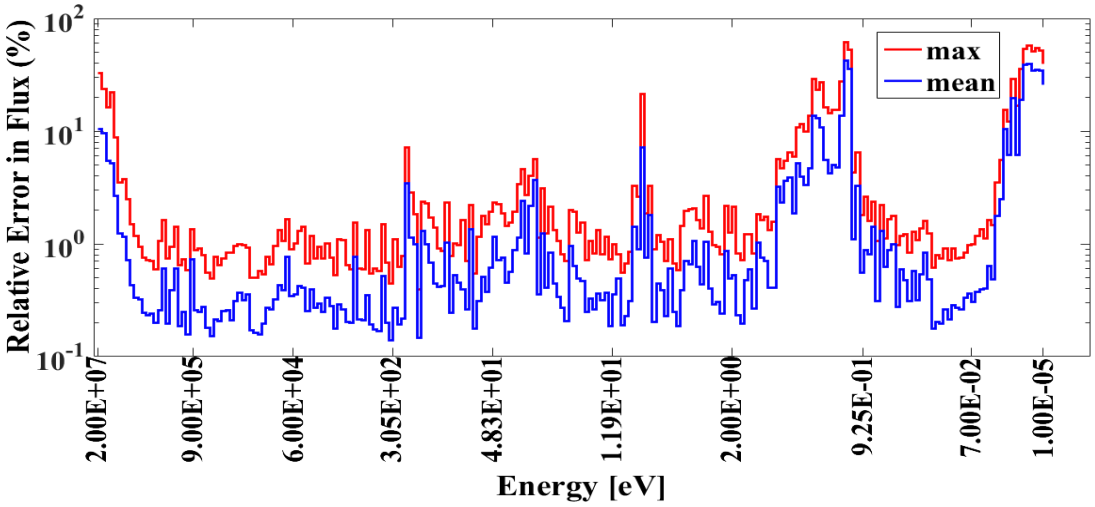

Fig. 5-3. Maximum and Mean Error bounds for MOX flux.

Next, the actual errors are plotted against the error bounds for both UO_2 and MOX mixtures at each energy group and if the bounds from 5.2 and 5.3 are violated, then the low-fidelity subspace could not represent the high-fidelity one. Luckily this is not the case here as can be inferred from figures 5.4 through 5.7. Even numbered figures show the relative errors vs. the

www.manaraa.com

error bounds at one of the fast region flux (1.85-2.35 MeV) while the odd numbered ones are typically showing relative errors and error bounds for a typical thermal region (0.975-1.0 eV). Figures 5.4 and 5.5 deal with errors in UO_2 flux, Whereas 5.6 and 5.7 are for MOX flux errors

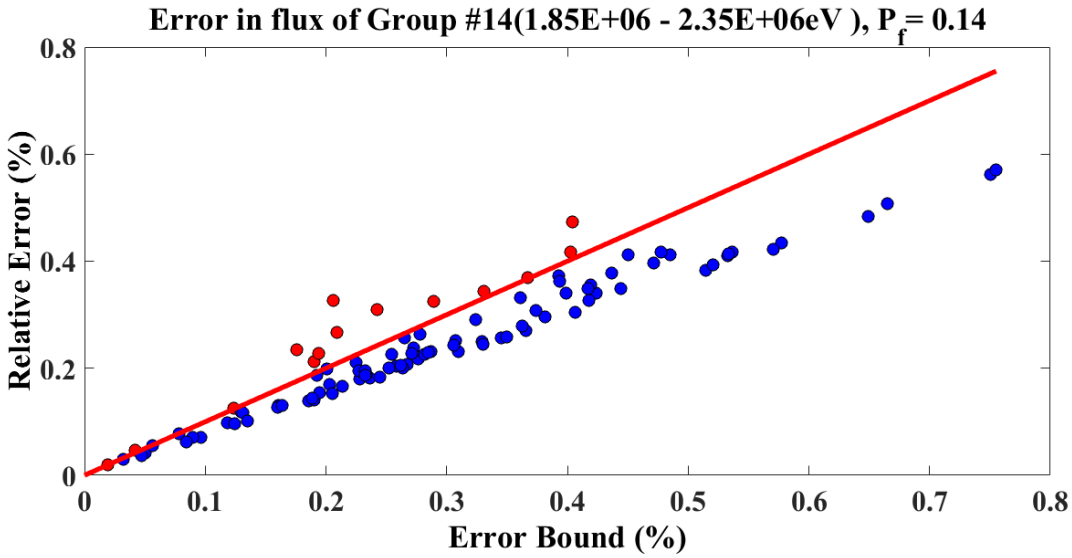

Fig. 5-4. Errors in UO_2 Fast Flux.

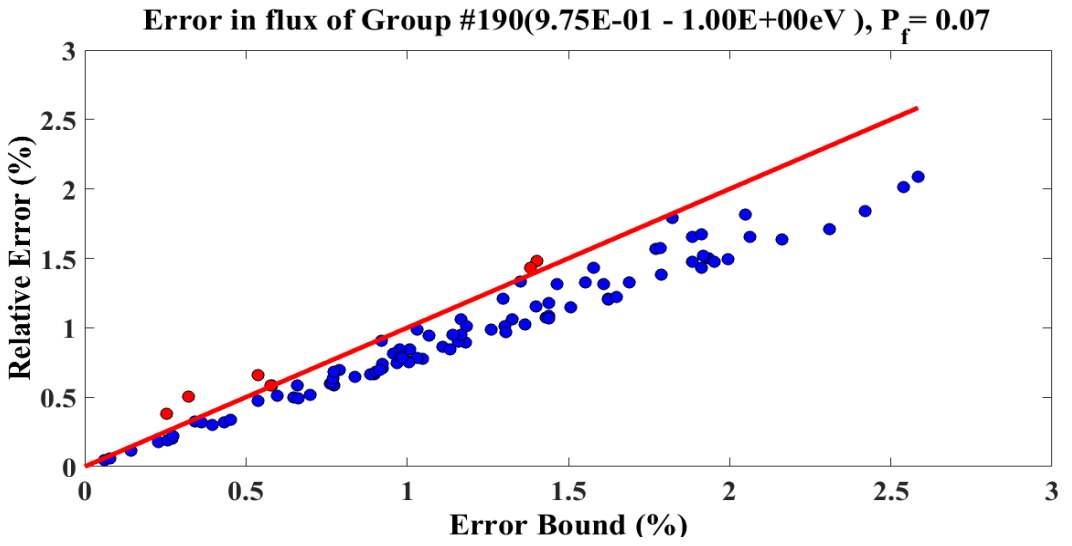

Fig. 5-5. Errors in UO_2 Thermal Flux.

Figure 5.4 assures that the fast flux in UO_2 does not violate the bounds of 3% maximum error and 0.8 % mean error. Similarly, figure 5.5 declares that neither the thermal flux in UO_2

www.manaraa.com

does. In other words, the coarse mesh acceleration did not corrupt the active subspace enough to render any physical behavior of UO_2 uncaptured and hence errors were not surprising and gave same predicted bounds.

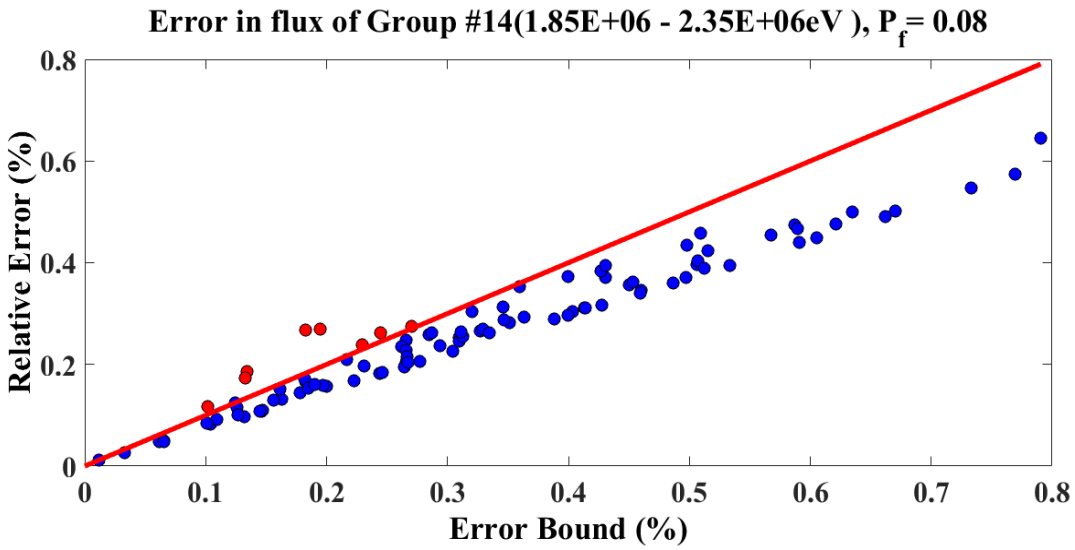

Fig. 5-6. Errors in MOX Fast Flux.

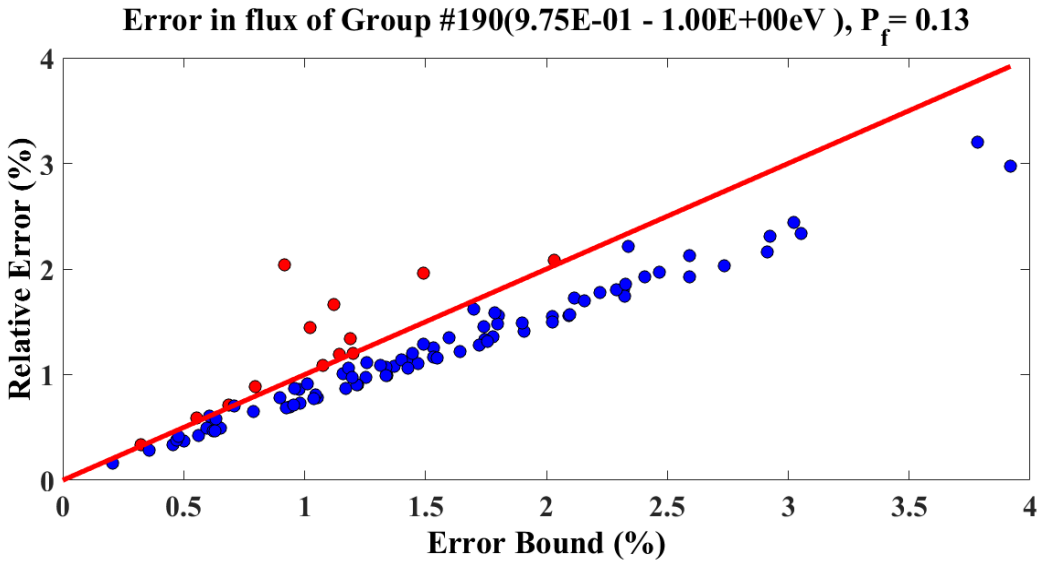

Fig. 5-7. Errors in MOX Thermal Flux.

www.manaraa.com

Both of figures 5.6 and 5.7 warrant the same fact; that the error bounds are not violated by either energy groups in the MOX fuel too. Which means that the low-fidelity based active subspace managed successfully to capture all physics behaviors exhibited by the MOX fuel.

Previous figures and discussion demonstrate that accelerating the construction of the ROM model by using a coarser mesh has not obscured the main characteristics of the active subspace in terms of its size and its associated error bounds on the responses of interest.

5.3.2 Case Study 2: Finding the dominant fuel (UO_2 or MOX) in the Active Parameter Subspace.

If multiple fuel pin types are present in the assembly, it is natural to inquire as to which pin is more representative in terms of capturing the active subspace. A brute force approach would evaluate all pins altogether. A physics-informed guess supported by the developed error bound would prove more valuable. For this goal, a PWR fuel assembly with a large water boundary and a vacuum boundary condition is considered. A single row consisting of 7 UO2 pin cells adjacent to 8 MOX pin cells followed by a reflector region is studied as the high-fidelity model. The reflecting boundaries on the top and bottom justify the treatment of the model as an infinite model in the y-direction. The large reflector region induces enormous potential for scattering which will delay the conversion of the iterations and make the high fidelity model relatively expensive to run [110]. Given how big the parameter space is (i.e., 741 material-reaction pairs * 238 energy groups=176358 cross sections), reduced order modeling techniques are to be used, this will require executing the adjoint version of the original model few hundred times which is the typical intrinsic dimension inferred from previous experience with similar

www.manaraa.com

models. For this assembly model, this can be overwhelmingly expensive and hence motivates the use of M_LROM. The low-fidelity model can be a single UO2 pin or a single MOX pin and maybe it is a good idea to try a pin cell adjacent to the same portion of the reflector. These suggested low-fidelity models are depleted to different points and each is passed to the error construction estimator discussed in chapter 4. Once the active subspace hosting all the possible variational directions sufficient to span the input space is extracted, then it is tested to see whether it can be promoted to represent the high-fidelity model as well without violating the error bound. Figure 5.8 layouts the high fidelity model showing both types of pin cells as well as the large reflector domain.

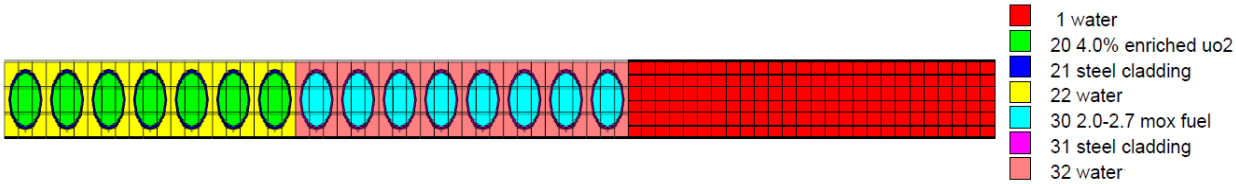

Fig. 5-8. 15 Pins row of a PWR assembly (High-fidelity model).

The numerical test extracted the parameter active subspaces with lowest error bounds when the pin cell containing UO_2 was depleted to 30 GWd/MTU adjacent to the same large reflector. This reveals that UO_2 is more informative than MOX fuel in the sense that the active subspace extracted from UO_2 better simulates the physical behaviors for the whole assembly than the MOX fuel. Figure 5.8 shows the low-fidelity model configuration. The responses are taken again to be the material flux at each energy group. The binomial estimator is used to construct a list of error bounds for each response which can be shown in figure 5-10.

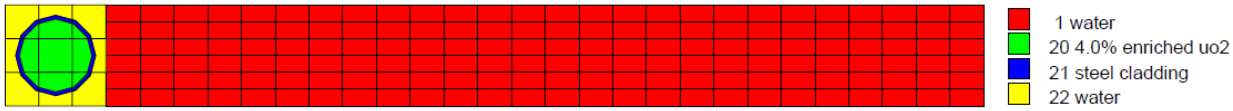

Fig. 5-9. UO_2 pin cell with large reflector region (Low-fidelity model).

www.manaraa.com

Figure 5.10 plots the bounds for relative errors in material flux at each energy group stating that the maximum and mean error bounds are less than 5% and 2% respectively for the fast region flux and the maximum and mean error bounds do not exceed 20% and 8% respectively in the thermal region. This active subspace is extracted from the low-fidelity model after depleting it half way (30 GWd/MTU) and the selected intrinsic coordinate is 800. Next, this active subspace is tested with the high-fidelity model to quantitatively judge how 'good/bad' the low-fidelity active subspace can represent the high-fidelity model.

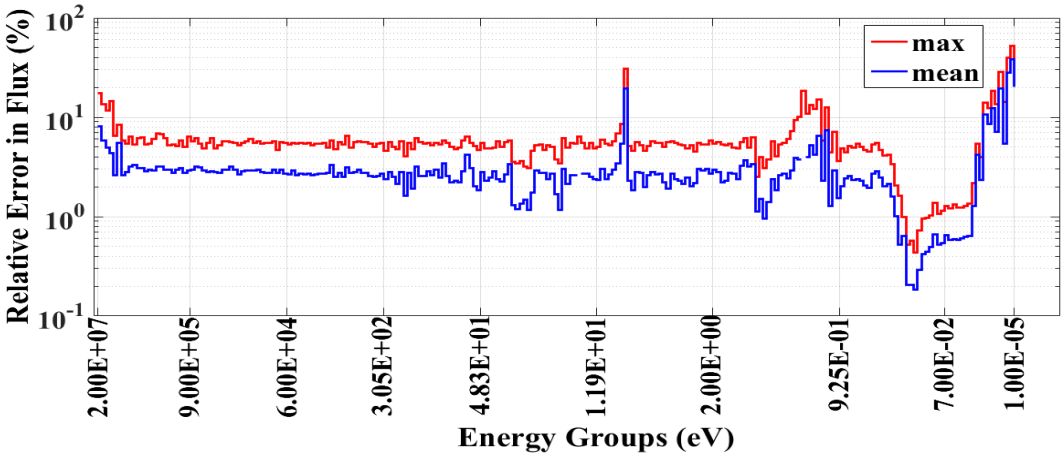

Fig. 5-10. Maximum and Mean Error Bounds in the material flux of UO2 from the (LF Model).

Figures 5.11 through 5.14, each depicts a comparison between the actual errors due to the projection of the high-fidelity model onto the active subspace extracted from the low-fidelity model. Odd numbered figures within that range concerns about the error in the material flux within one of the fast groups (1.85-2.35 MeV), whereas the even numbered ones show the error in the material flux within a thermal group (0.975-1.0 eV). Figures 5.11 and 5.12 pictures the error in the UO2 material flux due to running the high-fidelity model constraining the perturbed cross sections to the active subspace extracted from the low-fidelity model, wherein figures 5.13

www.manaraa.com

and 5.14 the error in the MOX material flux is inspected after the same projections onto the active subspace.

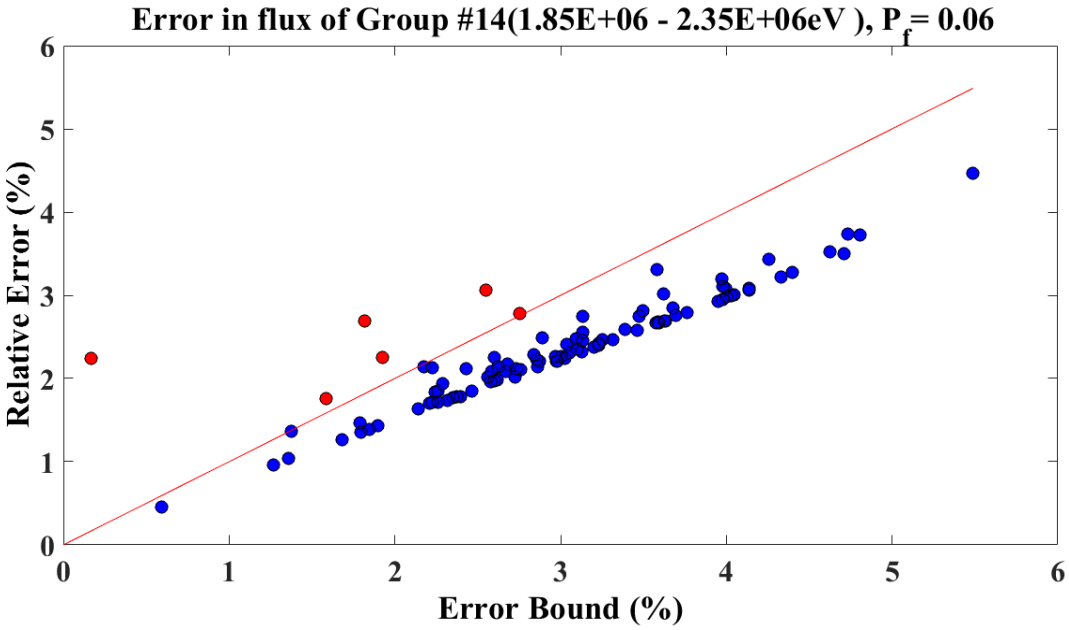

Fig. 5-11. Error in UO2 material flux in the fast region (1.85-2.35 MeV).

Figure 5.11 shows that the relative error has never exceeded the bound for the maximum errors in the fast groups (5%). The red dots represent the failed cases where the error bounds exceeded the actual relative errors and these are within a user-defined probability of 0.1. It is noticed that most of these failed cases are pretty close to the 45-degree solid line promising that the bounds for the failed cases are very close to the actual error. An important reminder to the reader is that the probability of failure was picked to be relatively large to allow the occurrence of some failed cases for the sake of illustration. In practice, the probability of failure is picked to be 0.00001 instead of 0.1, which adds a cost of sampling 5 random vectors instead of 1 and the cost of performing 5 matrix-vector product as shown in equation (4.30) with $s = 5$.

www.manaraa.com

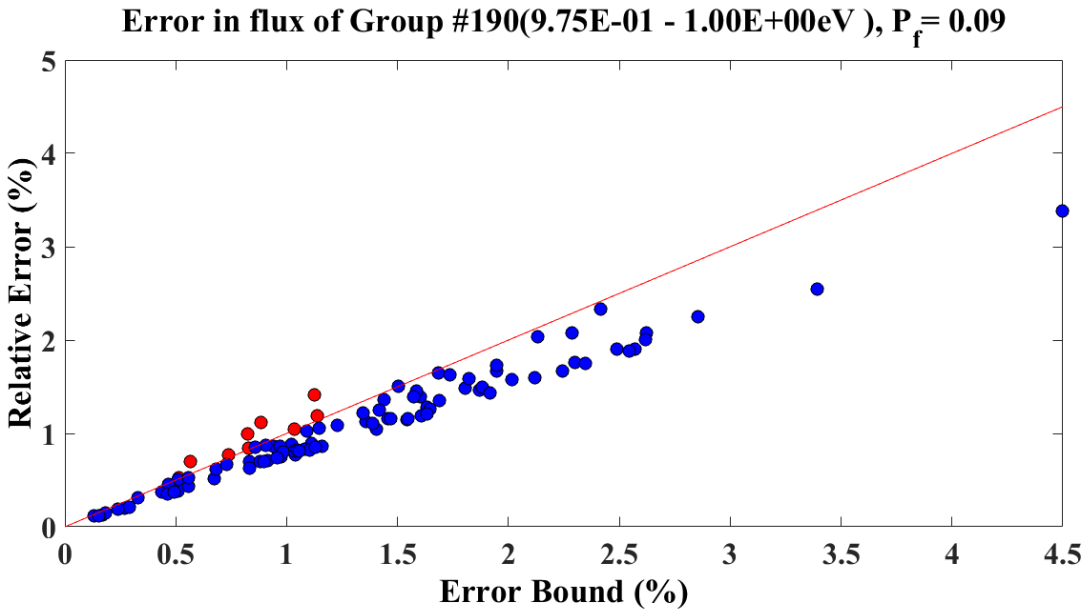

Fig. 5.12. Error in UO2 material flux in the thermal region (0.975-1.0 eV).

Figure 5.12 assures that UO2 material flux did not violate the error bounds at all (20% max. error and 8% mean error) in the thermal energy range (0.975-1.0 eV). It is not surprising that the errors here agree with the estimated bounds because the subspace was extracted from the low-fidelity model which consists of a UO2 pin and a reflector. But what about the error in the MOX material flux? The MOX was not present in the low-fidelity model, will the active subspace properly represent the physics induced by the MOX pin as well? These questions are to be addressed in the following figures and discussion.

www.manaraa.com

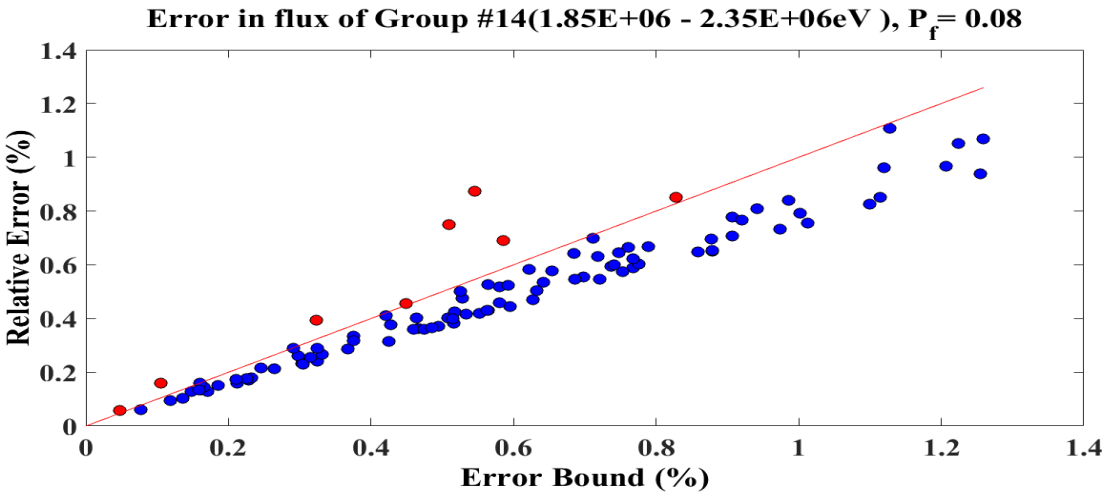

Fig. 5.13. Error in MOX material flux in the fast region (1.85-2.35 MeV).

It is easily inferred from figure 5.12 that the relative error in the MOX material flux did not violate the expected bounds. Furthermore, it is noticeable that the errors exhibited by the MOX material flux in the specified fast region were much lower than the ones in the UO2. This reads that the subspace extracted from the UO2 already covers all the important directions swept by the MOX parameter space.

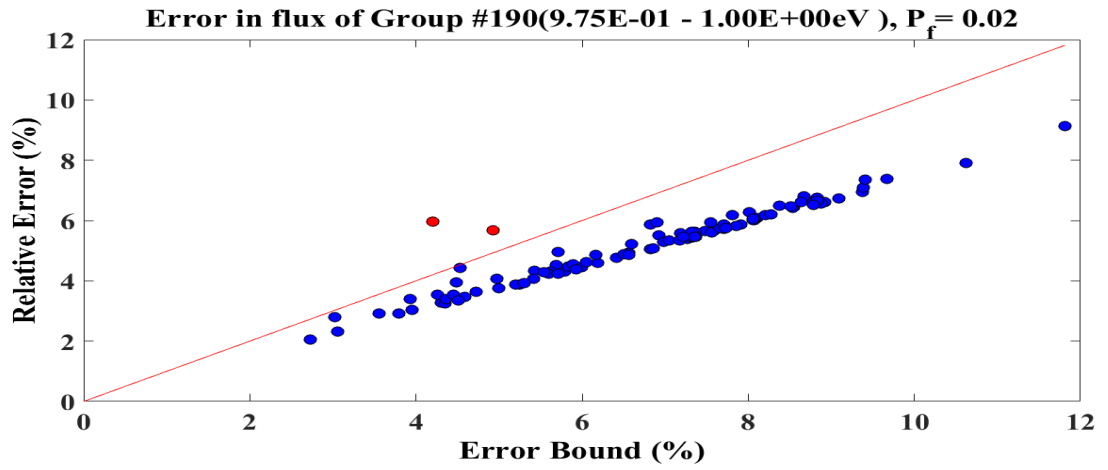

Fig. 5-14. Error in MOX material flux in the thermal region (0.975-1.0 eV).

www.manaraa.com

Figure 5-14 reassures that the thermal region error has not exceeded the bounds shown in figure 5-10 (8%) for most energy groups except for few energies such as the very first and last groups as well as few intermediate groups. In practice, the user can extract a table from Figure 5-10 corresponding to each group bound and decide which groups is she concerned about and hence accept or reject the proposed subspace accordingly. This being said one can state that the active subspace extracted from the low-fidelity model has succeeded to accurately (within the allowable accuracy) represent the high-fidelity variations. And the binomial estimator was robustly used as a quantitative metric to assess the quality of the extracted active subspace.

5.3.3 Case Study 3: Finding most Informative Pin Cell(s) in a Full Assembly.

This case study applies M_LROM to a benchmark lattice model for the Peach Bottom Atomic Power Station Unit 2 (PB-2), which is an 1112 MWe Boiling Water Reactor (BWR) manufactured by General Electric with the fuel rods arranged in a 7x7 grid as shown in figure 5-15. The main idea is to use one or more pin cell(s) to extract the active parameter subspace and then apply it to the whole assembly. This is intuitive since it is inspired by conventional nuclear reactor calculations, which are typically done at multiple levels. For example, in our demonstration, one is interested in computing an active subspace for the whole assembly over the entire range of depletion, but one can only afford to extract the active subspace using a lower level model representing a single fuel pin at a given composition. It is natural to think whether few fuel pin models at some prescribed compositions will be able to capture the interaction between the pins over the range of depletion.The main idea is to use one or more pin cell(s) to extract the active parameter subspace and then apply it to the whole assembly. This is intuitive since it is inspired by conventional nuclear reactor calculations, which are typically done at multiple levels. For example, in our demonstration, one is interested in computing an active

www.manaraa.com

subspace for the whole assembly over the entire range of depletion, but one can only afford to extract the active subspace using a lower level model representing a single fuel pin at a given composition. It is natural to think whether few fuel pin models at some prescribed compositions will be able to capture the interaction between the pins over the range of depletion.

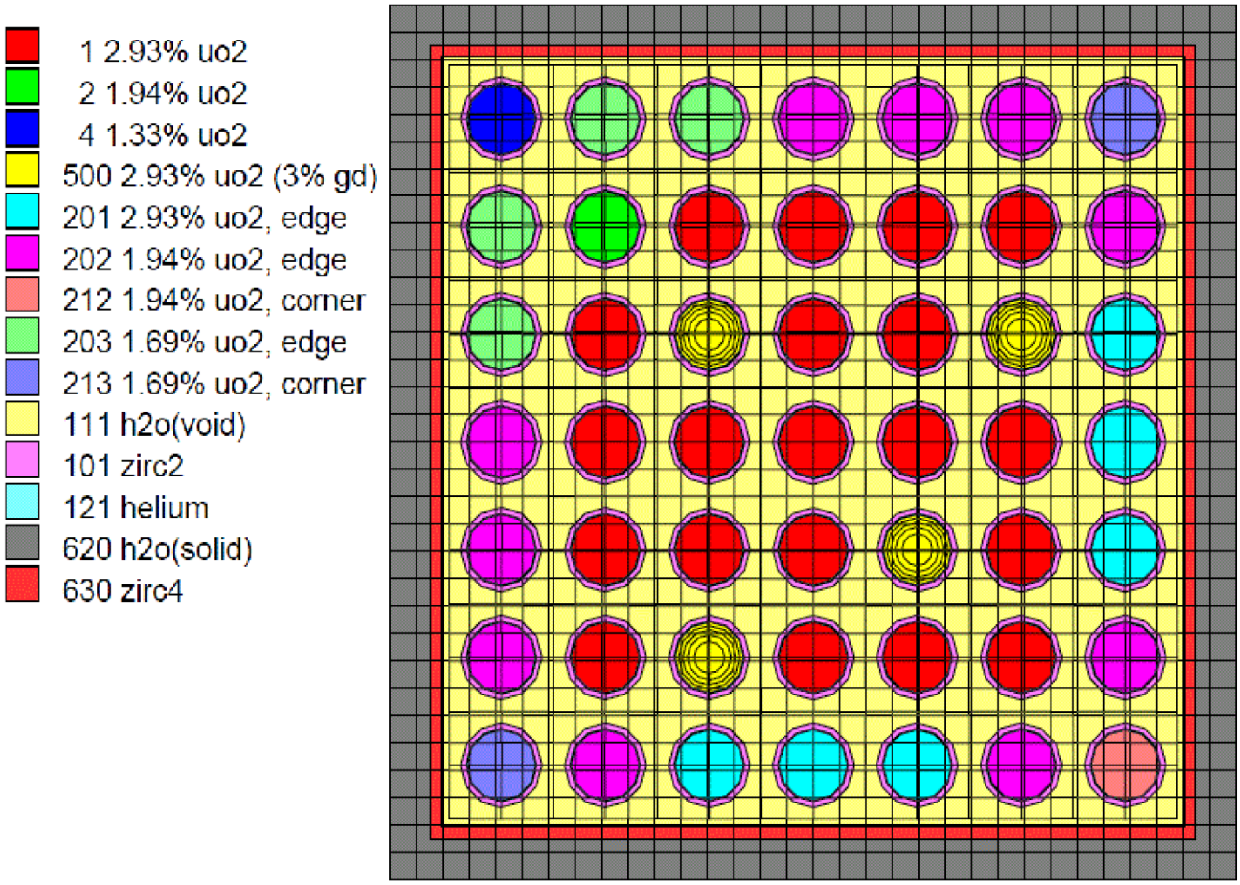

Fig. 5-15. 7x7 BWR Assembly Benchmark.

www.manaraa.com

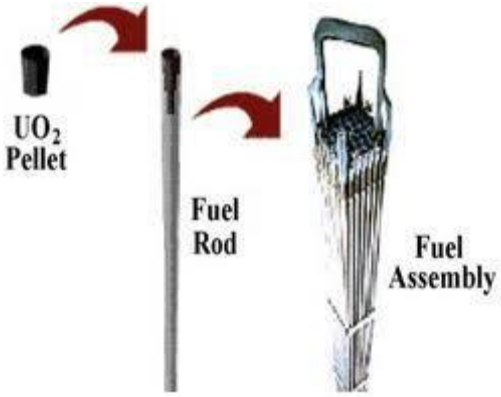

Fig. 5-16. Fuel Pellet, Fuel Rod, and Fuel Assembly.

(http://www.nrc.gov/about-nrc/emerg-preparedness/images/fuel-pellet-assembly.jpg)

The goal of this case study is to inspect which depletion point gives the best active subspace, in other words, if the model was depleted to different points, say 15, 30, 45 and 60 GWd/MTU, then the active subspace is extracted for each case, which of these active subspaces is representative of the entire range of depletion? Which of the pin cells is dominant in the sense that the active subspace associated with it is the closest to the active subspace of the whole assembly? To answer this questions, few justifications were performed for the sake of simplification. Originally the desired model is 56 energy groups, and the number of cross sections is (127 nuclide*7 reactions*56 energy groups = 49784 input parameters), in this test we will only use a 44 group library, 3 reactions, and 111 nuclides are perturbed, and thus the input parameter has a dimension of 14652. Each pin cell will be depleted to different burnups. After gathering the required experience, the original model will be used with higher dimension, and more than one pin cell will be employed to span the whole parameter space as shown in case study 4.

www.manaraa.com

In this test, the 2.93% enriched UO2 with 3% gadolinium pin cell is first depleted to 30 GWd/MTU. The resulting composition is used as the reference model for constructing the subspace. This pin is picked as it is believed based on the physics to be the most representative of all pins in the lattice. Note here that our goal is to identify the dominant cross-sections for all the pins. Hence, this step requires familiarity with the model. After the subspace is constructed, we employ it to model other fuel pins to establish whether our initial assumption of representativeness is adequate, and this is what we have done in this work. If the assumption is adequate, we move to the next level, and test its adequacy to represent the entire lattice; if not, other pins might be added to construct a more representative subspace [108].

The nominal dimension *n* of the parameter subspace for the reference pin cell is (93 fuel nuclides + 15 clad nuclides + 2 moderator nuclides + 1 gap nuclide) * 3 reactions * 44 energy groups that is 14,652 parameters. The effective dimensionality is selected to be 600. Note here that the error bounds are expected to vary from one response to the next because of two reasons. First, depending on the quality of the active subspace, different responses are expected to be captured to different degrees of accuracy. Second, because ROM attempts to identify the most influential components, non-influential responses such as the very fast and very thermal groups are expected to have higher relative errors than the rest of the groups.

Figures 5.17 through 5.24 illustrate how the subspace extracted from the low-fidelity model behaves when used with different pin cells. Odd-numbered figures display the errors in the flux range of (1.85 – 2.35 MeV), whereas the even-numbered figures are for the range (0.625 – 1.0 eV). Figures 5.17 through 5.20 show how the subspace behaves if used to identify the parameters of a 1.33% enriched UO2 pin cell, whereas figures 5.21 through 5.24 are for a 2.93% enriched UO2 pin cell. Figures 5.17, 5.18, 5.21 and 5.22 show the actual error vs. the error

www.manaraa.com

bound due to parameter reduction after depleting to 15 GWd/MTU. Whereas Figures 5.19, 5.20, 5.23 and 5.24 are for pin cells that were depleted to 45 GWd/MTU. In all figures, the red dots represent failed cases where the blue ones represent the success, i.e., when the error bound is exceeded by the actual error. All the cases showed a failure probability of less than 0.1 which is the user-specified value. The solid 45-degree line separates the failure and success regions. In this demonstration, the probability of failure is picked to be relatively large for the sake of illustration to give room to the occurrence of failed cases. In practice, however, the failure probability is set to at most 0.00001.

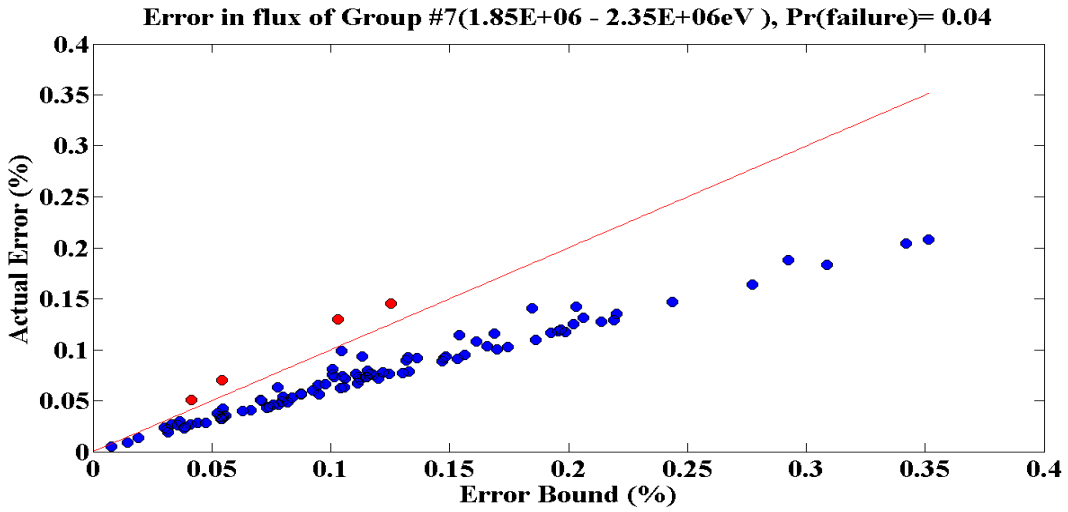

.

Fig. 5-17. Fast Flux Error (15 GWd/MTU).

www.manaraa.com

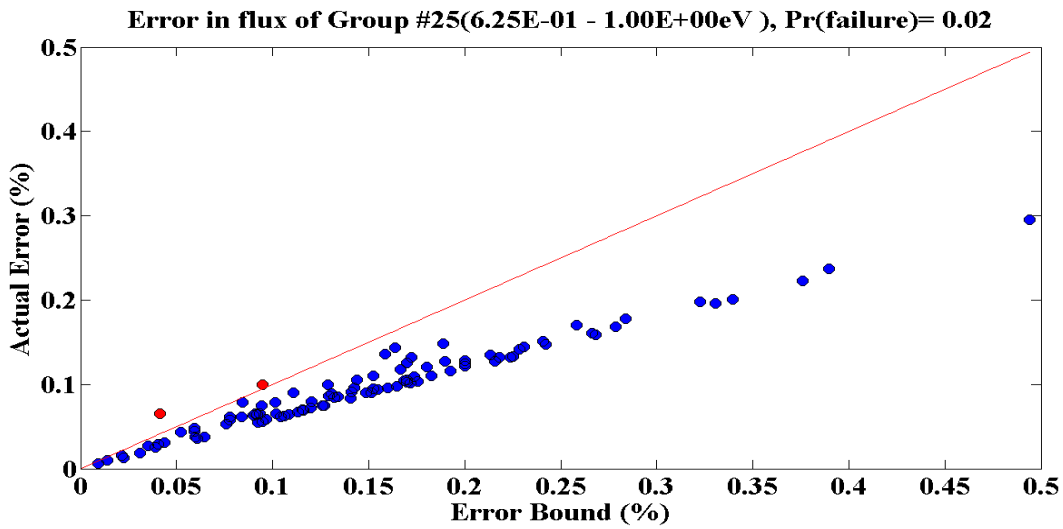

Fig. 5-18. Thermal Flux Error (15 GWd/MTU).

Figures 5-17 and 5-18 show that the maximum error bound in the specified fast flux range is 0.35% whereas the maximum error bound in the specified thermal region is 0.5%. Figures 5.19 and 5-20 examine the active subspace applied on the same pin cell if the initial composition resulted from a 45 GWd/MTU depletion.

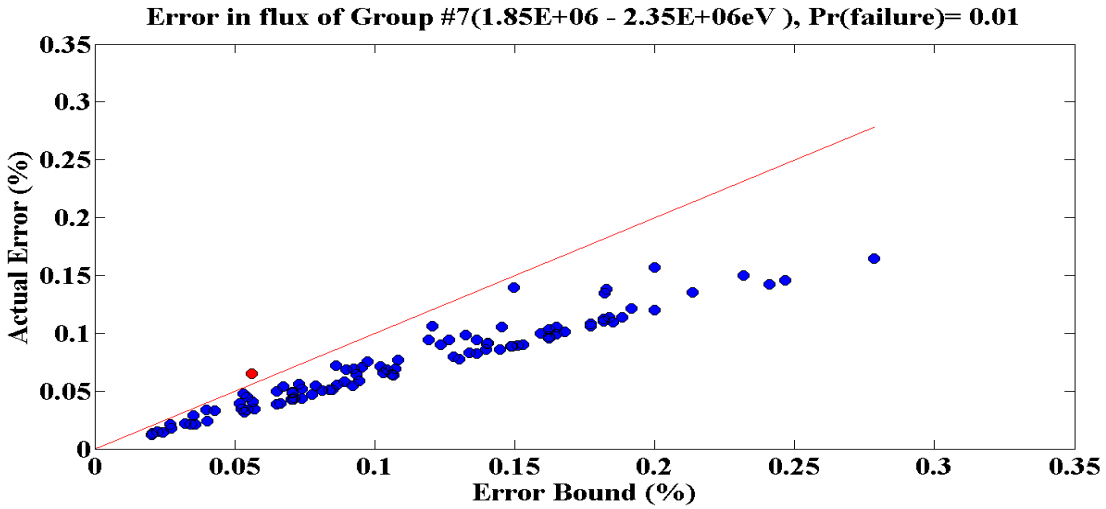

Fig. 5-19. Fast Flux Error (45 GWd/MTU).

www.manaraa.com

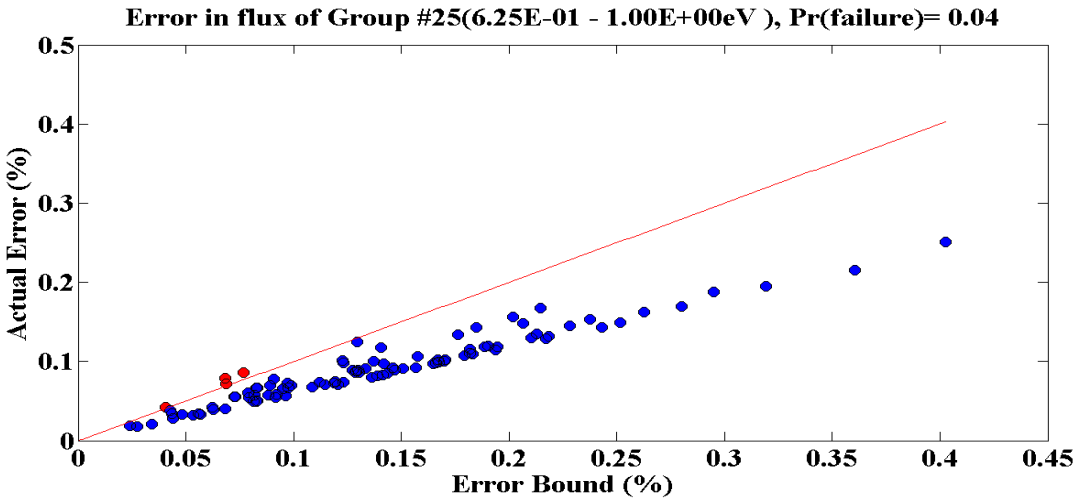

Fig. 5-20. Thermal Flux Error (45 GWd/MTU).

The previous two figures show that the maximum error in the all the fast and thermal ranges are 0.28% and 0.42%, respectively which is still within the range. Figures 5.21 and 5.22 show the fast and thermal flux errors for the 2.93% enriched UO2 pin cell after depleting to 15 GWd/MTU.

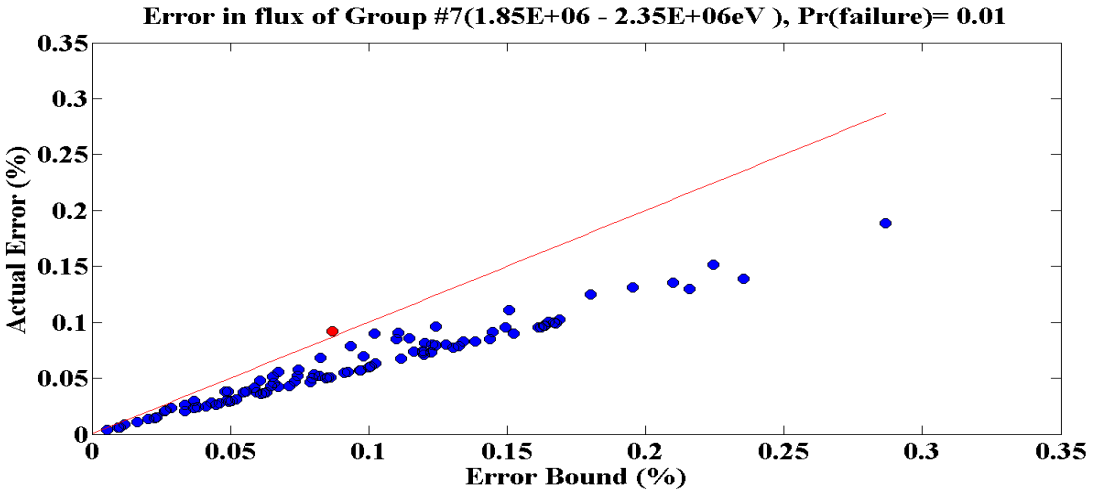

Fig. 5-21. Fast Flux Error (15 GWd/MTU).

www.manaraa.com

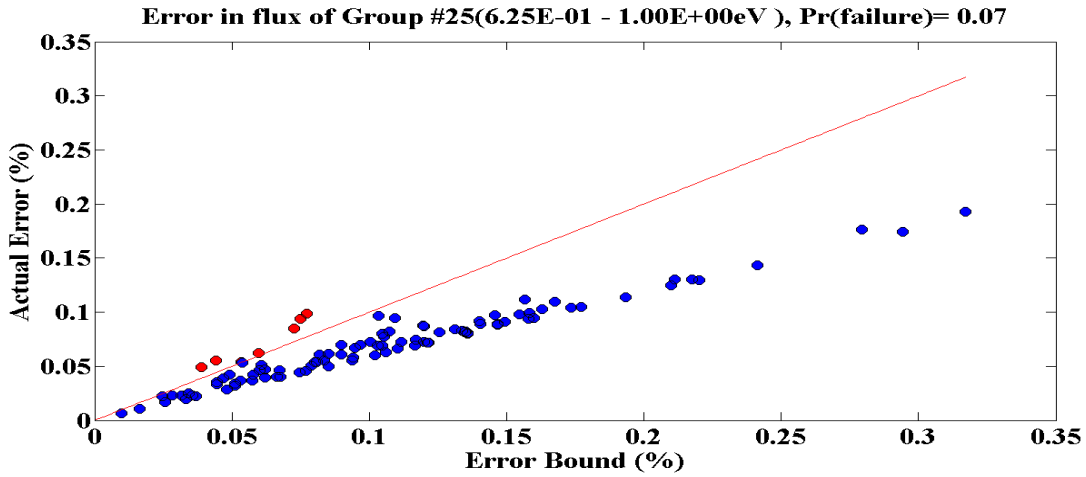

Fig. 5-22. Thermal Flux Error (15GWd/MTU)

Maximum error bound in fast and thermal flux are found to be 0.3% and 0.33 respectively. Finally, figures 5.23 and 5.24 plot the errors if the pin cell is initially depleted to 45 GWd/MTU.

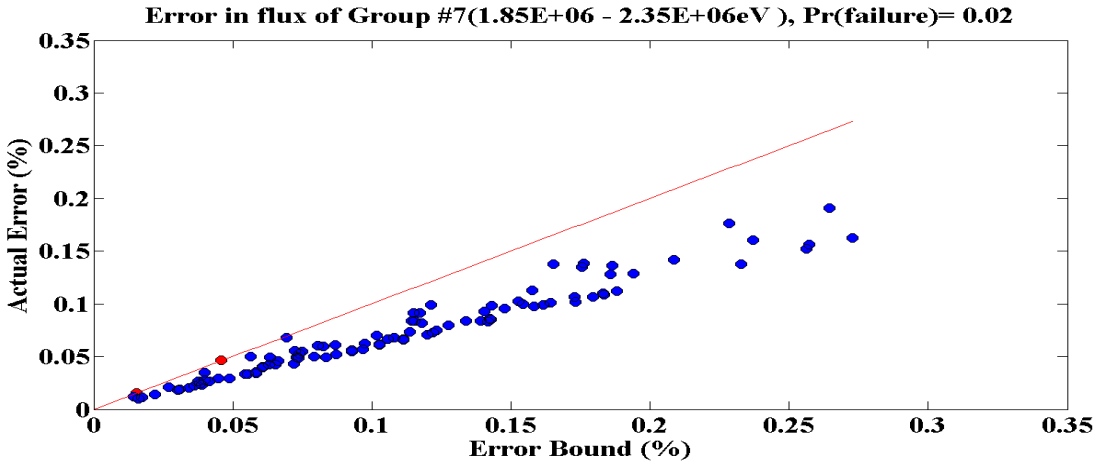

Fig. 5-23. Fast Flux Error (45GWd/MTU)

www.manaraa.com

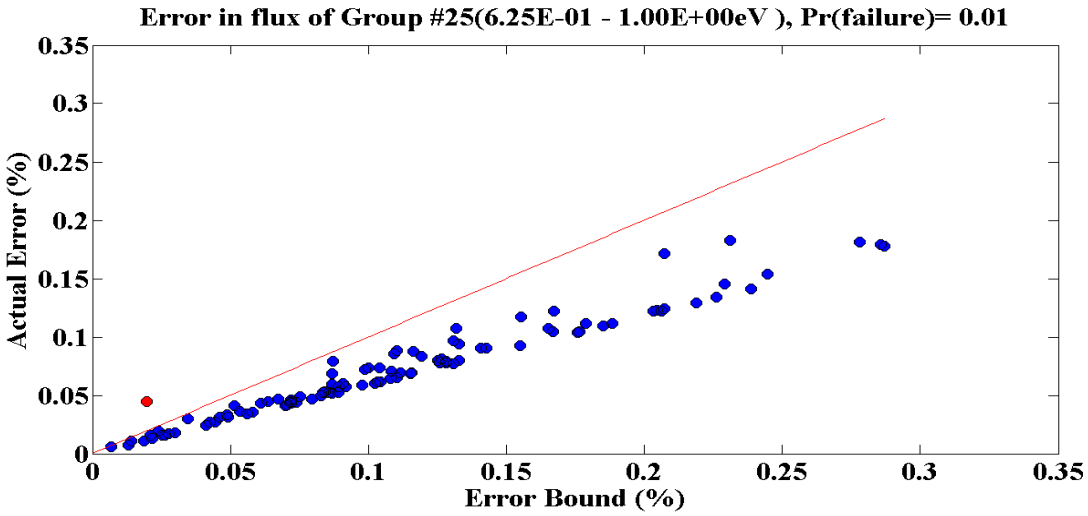

Fig. 5-24. Thermal Flux Error (45GWd/MTU)

Again figures 5-23 and 5-24 show that constraining the cross sections to the active space extracted from the reference pin cell model resulted in an error that does not exceed 0.3% for the specified fast range of (1.85 – 2.35 MeV) where the thermal range exhibited error bounds the follow the same pattern and recorded a maximum value of 0.3%.

The previous test showed that the highest depleted pin cell (2.93%) with (3% gd) has managed to represent other pin cells with a maximum relative error of about 0.35% yet when this same pin cell was tested with the whole assembly it gave a very high errors indication that one either needs to add other pin cells when constructing the subspace and /or more basis needs to be sampled to capture the different physics rising from running the whole assembly. This motivates the next case study where a larger parameter space is involved, and more cross sections and reactions are perturbed with a higher number of energy groups resulting in almost tripling the size of the original parameter space.

www.manaraa.com

5.3.4 Case Study 4: Construction of the Domain of Validity of Active Subspaces using M_LROM.

This case study employs the same assembly model showed in figure 5.14. The test is designed to accomplish the following:

- Finding which pins are representative of the whole assembly.
- Determining the domain of validity, which guarantees that constraining the cross sections to the proposed subspace will not exceed (with high probability) a user-specified error if the initial conditions, depletion, temperature and/or other conditions are perturbed.

The previous test indicates that the 30 GWd/MTU depleted pin cells will give the best subspaces and that the highest depletion pin cell (with 3% gd.) will certainly be one of the pin cells selected to form the low-fidelity model. To pick which is the other pin cell(s) that needs to be added when extracting the active subspace, the following 3-dimensional visualization attempt is considered. The visualization indicates that the subspaces extracted from all the pins are so close to each other which implies that the subspace extracted from one (or more) pin cell(s) can be representative of the whole assembly model.

It stands to reason that visualizing higher dimensional data can handicap the process, but it is also important to notice that we are not looking for the shape or topology of a higher dimensional subspace (or even hyperspace), rather we are looking for the relative differences between each pin's subspace, so as long as we pick a similar visualization concept for all of them, then we can detect which pin(s) has different important directions that are not captured by other pins.

www.manaraa.com

To visualize this, each basis vector is divided into three parts, and the norm of each part is taken as a single coordinate:

$$x_i = \left\| \mathbf{U}_x^{(r)}(1:N/3, i) \right\|$$
$$y_i = \left\| \mathbf{U}_x^{(r)}(N/3+1:2N/3, i) \right\|$$
$$z_i = \left\| \mathbf{U}_x^{(r)}(2N/3+1:N, i) \right\|$$

where $\mathbf{U}_x^{(r)}$ is a matrix whose orthonormal columns span the active subspace under inspection. The following figure shows this visualization attempt.

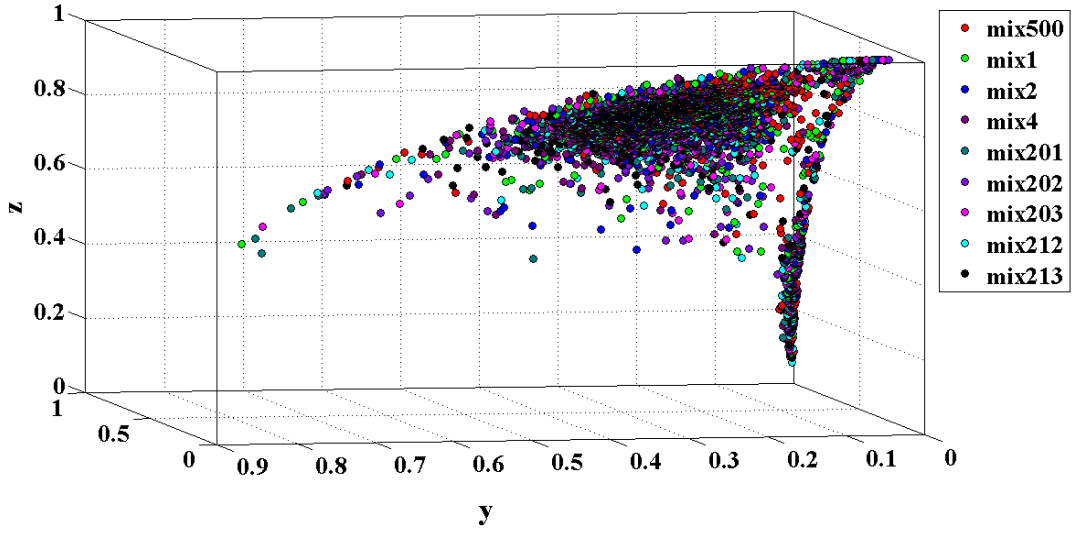

Fig. 5.25. Scatter Visualization for the 9 Pin Cells Active Spaces.

To analytically judge these subspaces and select the most representative one(s) the analyst can compute the angles between the active subspaces for each pin cell and the one for the whole assembly as follows:

$$\mathbb{P}\left\{ \sin\theta_{\mathcal{X}_{assembly}, \mathcal{X}_{pin_i}^{(r)}} = \left\| \mathbf{U}_{x,assembly} \mathbf{U}_{x,assembly}^T - \mathbf{U}_{x,pin_i}^{(r)} \mathbf{U}_{x,pin_i}^{(r)T} \right\| \leq \frac{4\lambda_1 \varepsilon}{\lambda_k - \lambda_{k+1}} \right\} \geq 1 - p_f \qquad (5.4)$$

www.manaraa.com

Another way to pick the pin cells that most represent the whole assembly is to compute the angles between the different pin cells and pick pins that give the largest angles because very small angles declare that the two pin cells give active subspaces that coincide or are very close, this tells the analyst that one of these pin cells is enough. A natural choice, in this case, is to start with the most dominant pin cell such as the pin with the maximum depletion and/or the most frequently repeated pin and then compute the angles as follows:

$$\theta_{\chi_i,\chi_j} = \cos^{-1}\left(\left|\mathbf{U}_{x,i}^{(r)T}\mathbf{U}_{x,\mathrm{j}}^{(r)}\right|\right) \tag{5.5}$$

From the previous discussion it follows that the 2.93% enriched UO_2 with 3% gadolinium pin cell, the 1.94% enriched UO_2 edge pin and the most frequently used 2.93% enriched UO_2 pin are first depleted to 30 GWd/MTU. The resulting composition is used as the reference case for constructing the parameter subspace. These pins are assumed to be the most representative of all pins in the lattice since one of them has the highest enrichment, the other is the most frequent and the third is an edge pin which might capture the location and boundary conditions effect. Note here that our goal is to identify the dominant cross-sections for all the pins. Hence, this step requires familiarity with the model. After the subspace is constructed, we employ it to model other fuel pins to establish whether our initial assumption of representativeness is adequate. If the assumption is adequate, we move to the next level, and test its adequacy to represent the entire lattice; if not, other pins are added to construct a more representative subspace [112].

The nominal dimension *n* of the parameter subspace for the reference pin cell is (127 nuclides * 7 reactions * 56 energy groups = 49784 parameters. The effective dimensionality is selected to be 1500. Figures 5-26 and 5-27 test the extracted subspace on the most dominant-

www.manaraa.com

From the author's perspective- pin cell, the one with the highest enrichment (2.93% UO_2, 3% gd). Figure 5-26 demonstrates the flux error in the energy range (1.85 – 3.0) MeV, whereas fig. 5-27 shows that error in the energy range (0.625 – 1.01) eV.

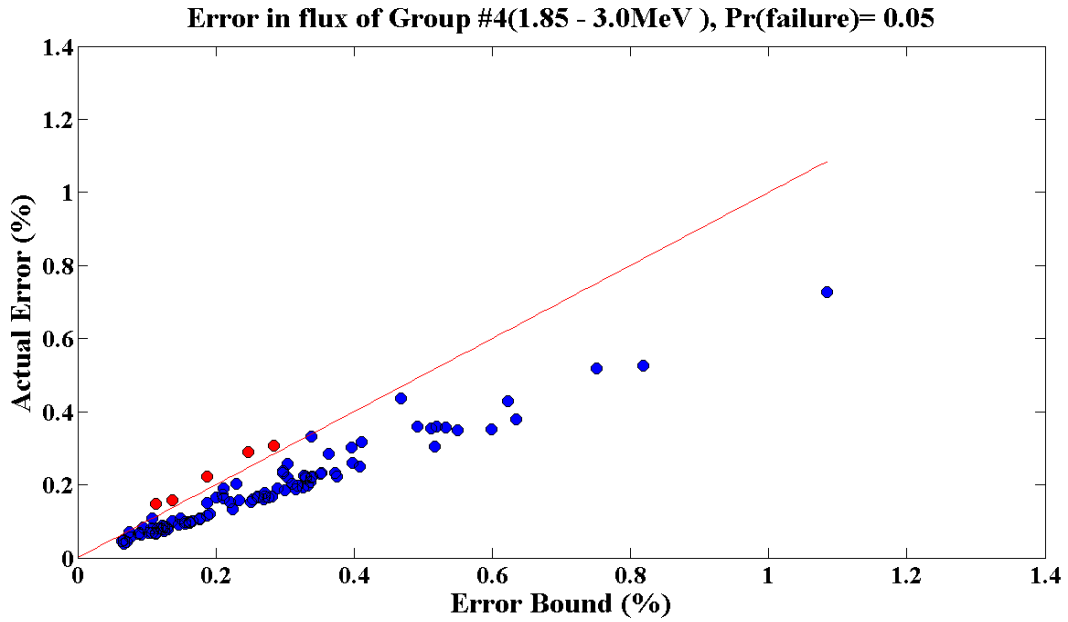

Fig. 5-26. Fast Flux Error (2.93% UO_2 Pin Cell, 3% gd.).

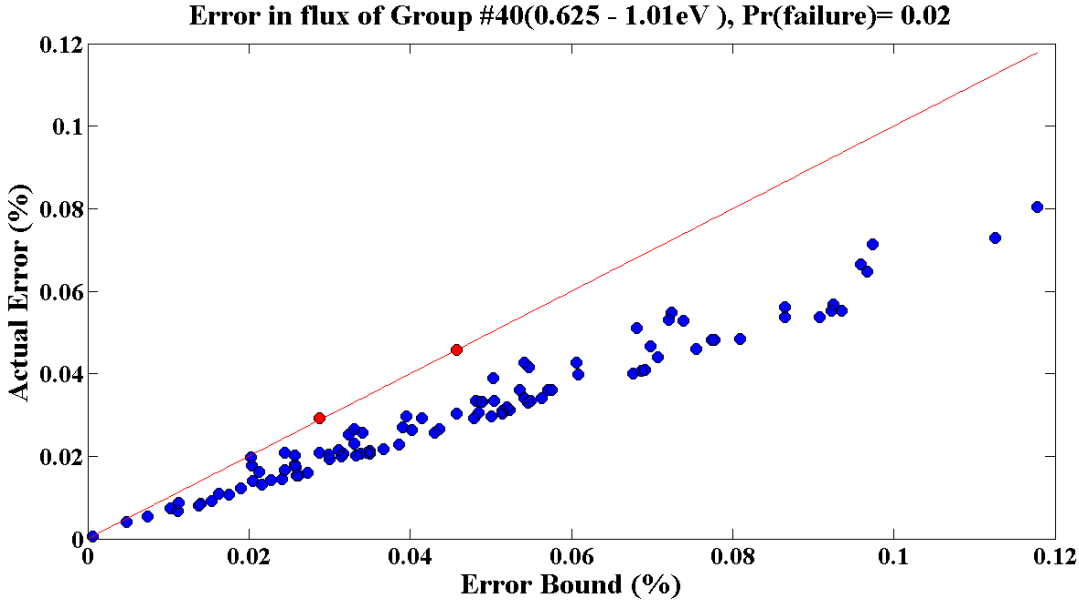

Fig. 5-27. Thermal Flux Error (2.93% UO_2 Pin Cell, 3% gd.).

www.manaraa.com

Figure 5-28 states that the maximum and mean errors over the whole energy range does not exceed 3% and 0.7 % respectively. Of course, this is after ignoring the first and the last energy groups where a slight number of reactions occur.

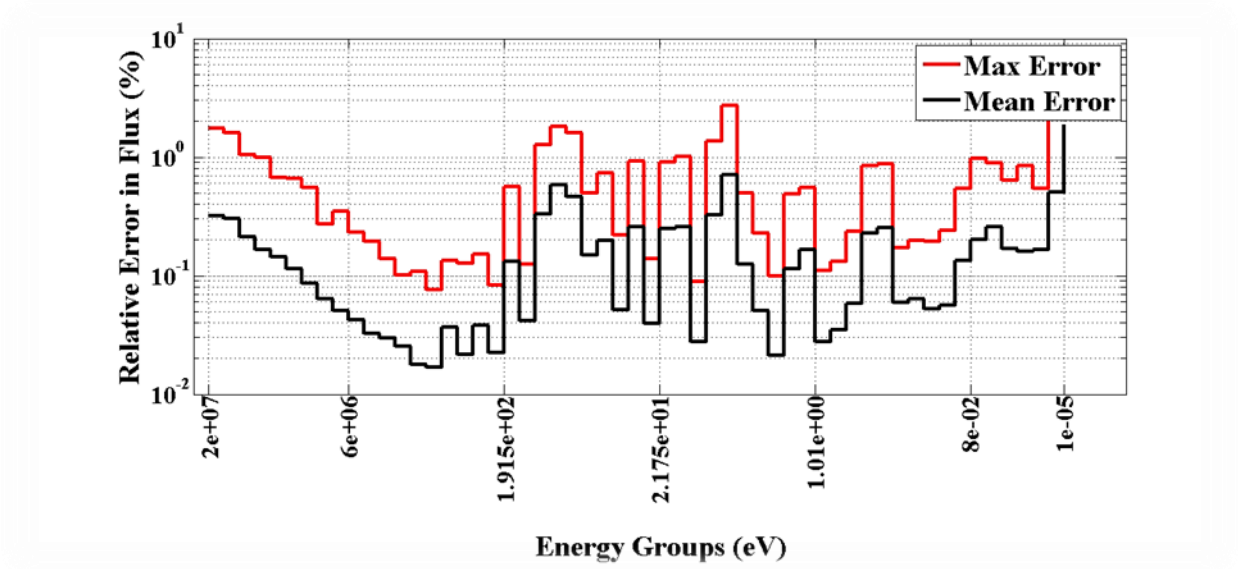

Fig. 5-28. Mixture 500, LF.

The next step is to test this subspace on another pin cell preferably different that the ones used to extract the subspace.Mixture 4 (1.33% UO_2 Pin Cell) is used for this purpose.

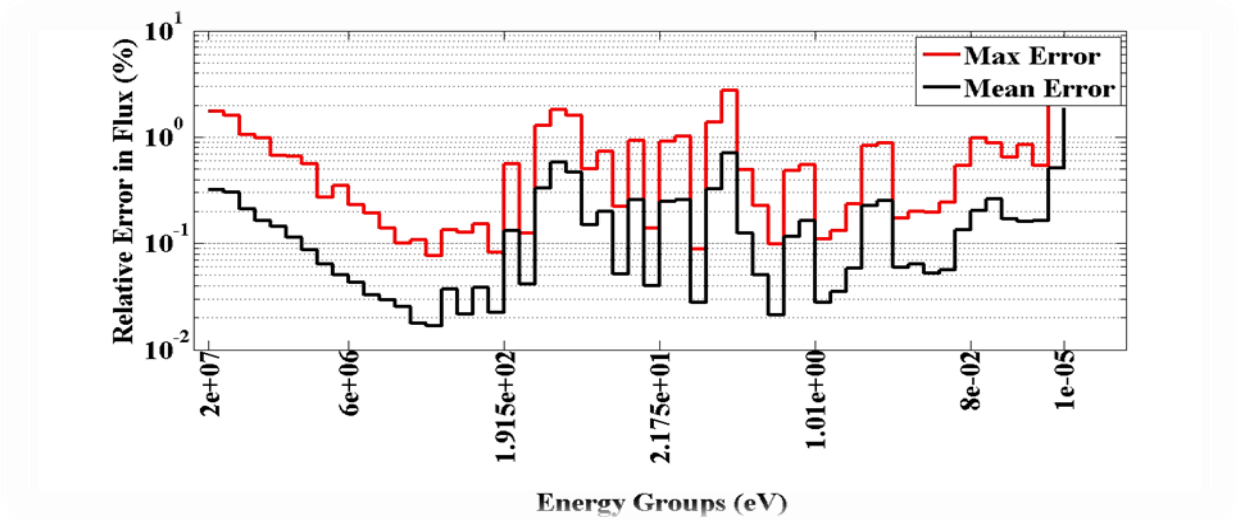

Fig. 5-29. Mixture 4, LF.

www.manaraa.com

Fortunately fig. 5-29 shows that the error resulting from this active subspace still gives a maximum error of 3% and a mean error of 0.7 %. This motivates one to have more confidence in the active subspace and use it with the full assembly. Figures 5-30 through 5-38 illustrate how the subspace extracted from the low-fidelity model behaves when used with the whole assembly. Each figure shows the maximum actual relative error in the flux of a certain fuel mixture due to projection on the extracted subspace.

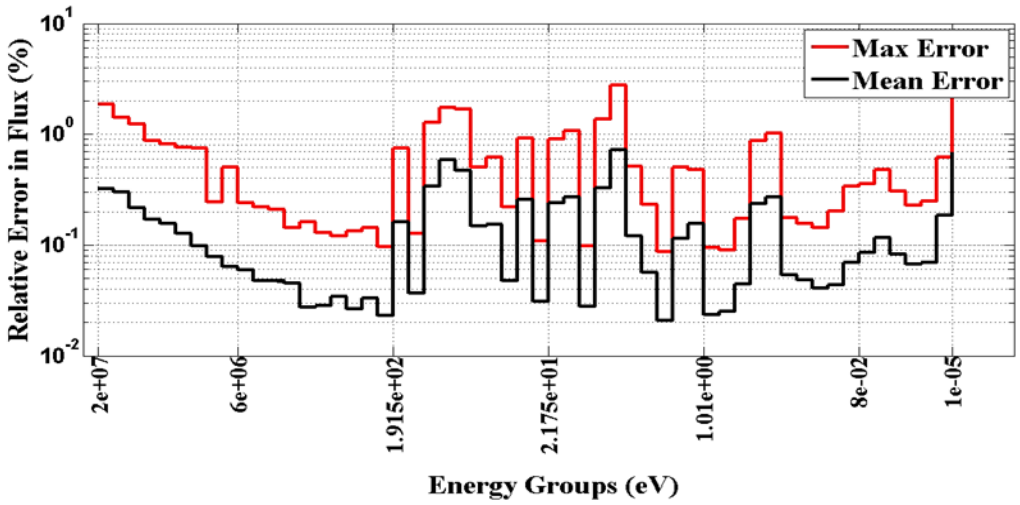

Fig. 5-30. Mixture 1 (30 GWd/MTU, Hot Conditions).

www.manaraa.com

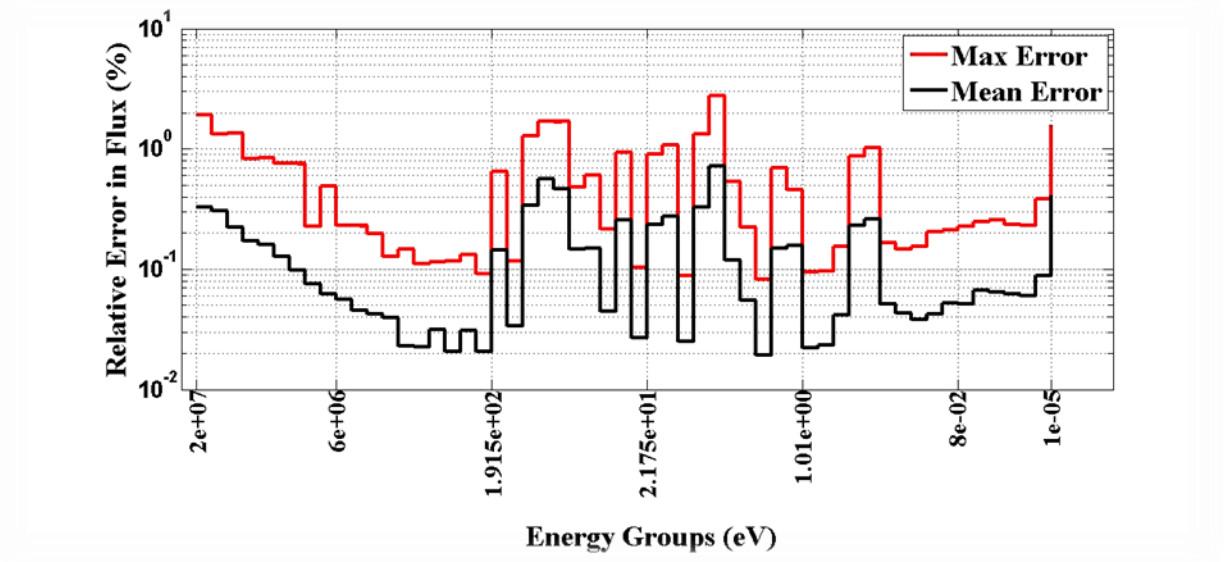

Fig. 5-31. Mixture 2 (30 GWd/MTU, Hot Conditions).

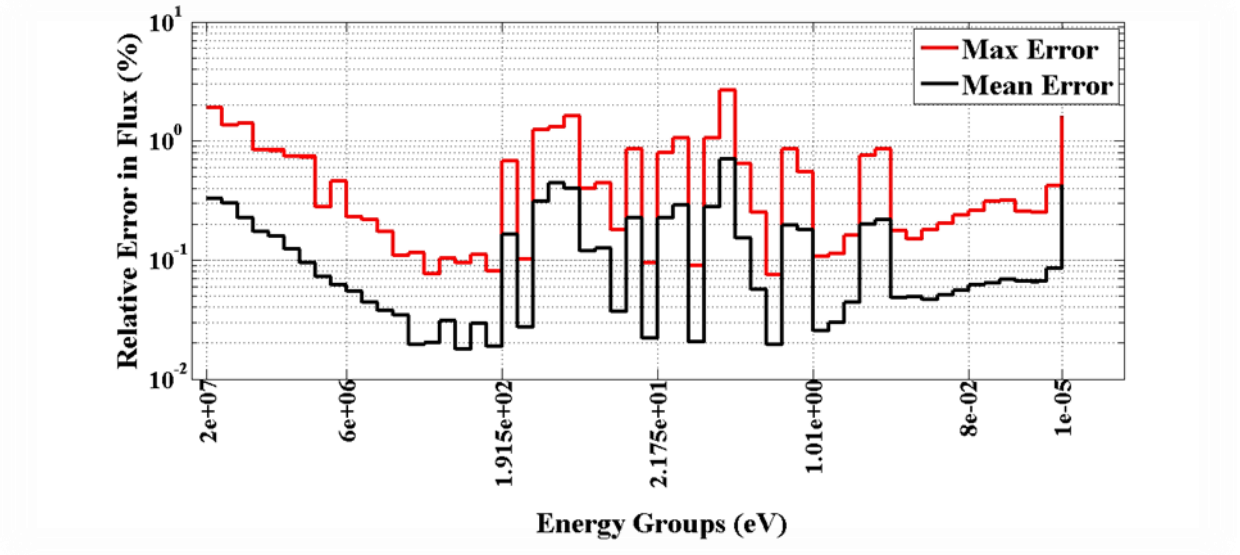

Fig. 5-32. Mixture 4 (30 GWd/MTU, Hot Conditions).

www.manaraa.com

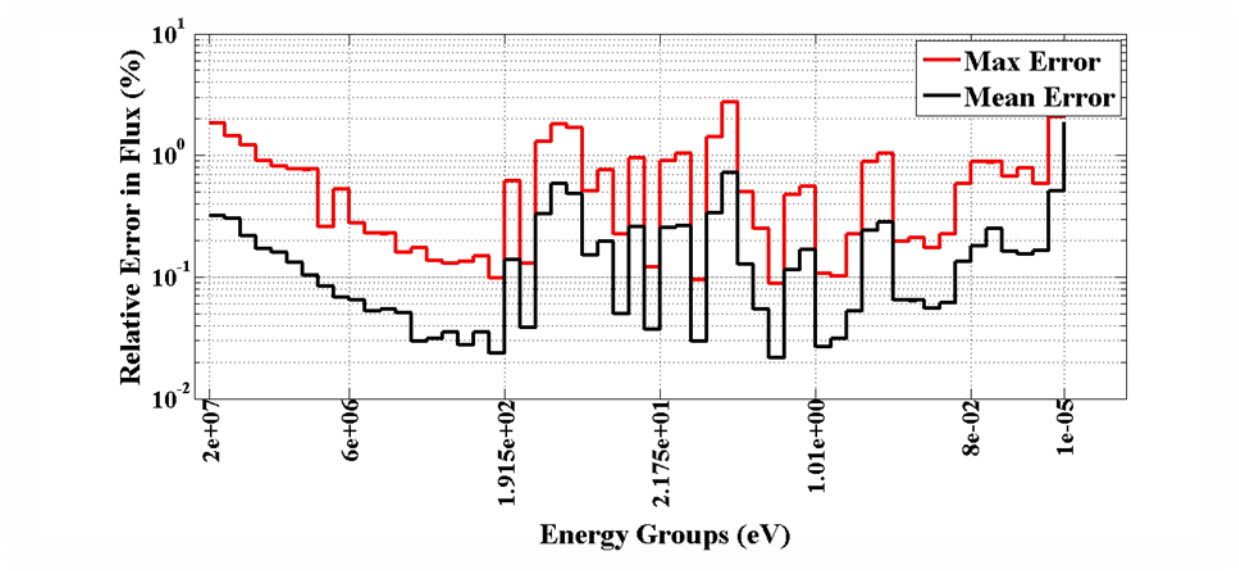

Fig. 5-33. Mixture 500 (60 GWd/MTU, Hot Conditions).

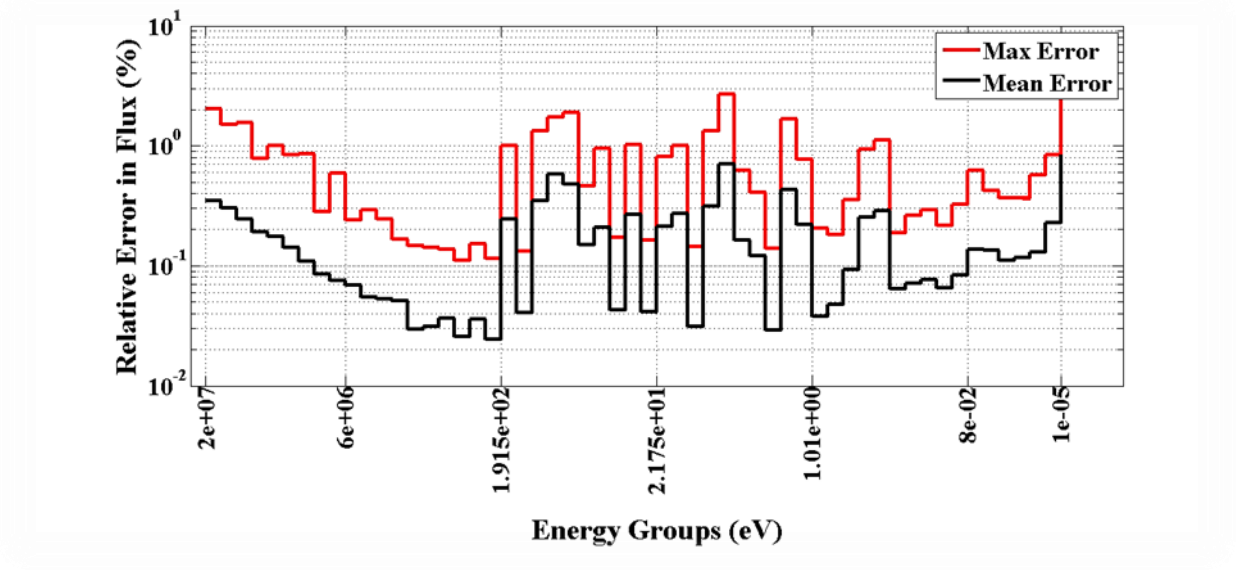

Fig. 5-34. Mixture 201 (60 GWd/MTU, Hot Conditions).

www.manaraa.com

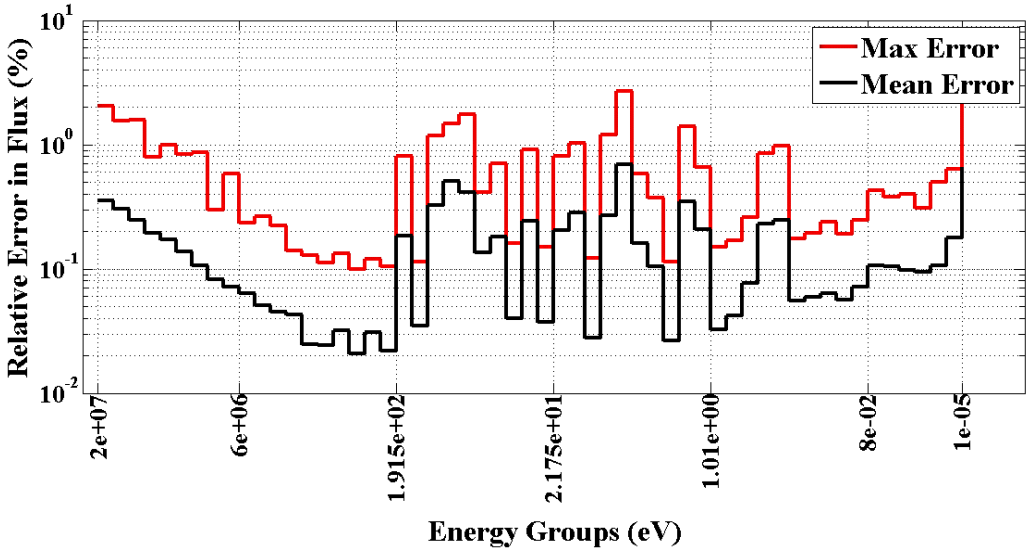

Fig. 5-35. Mixture 202 (30 GWd/MTU, Hot Conditions).

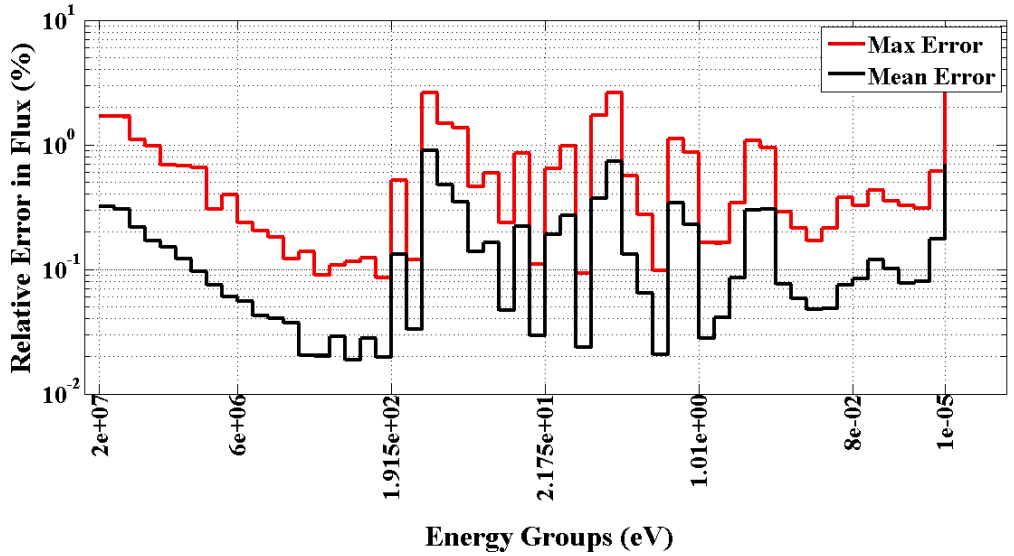

Fig. 5-36. Mixture 203 (20 GWd/MTU, Cold Conditions).

www.manaraa.com

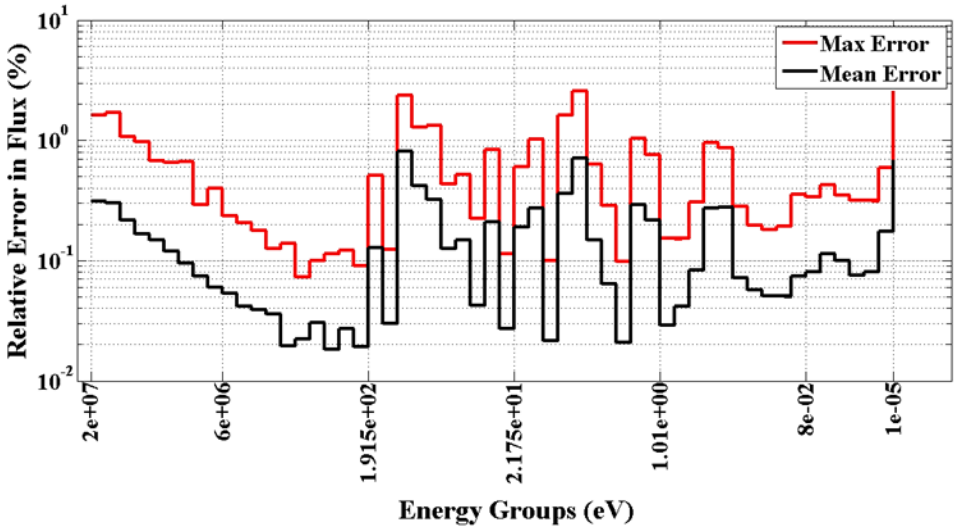

Fig. 5-37. Mixture 212 (20 GWd/MTU, Cold Conditions).

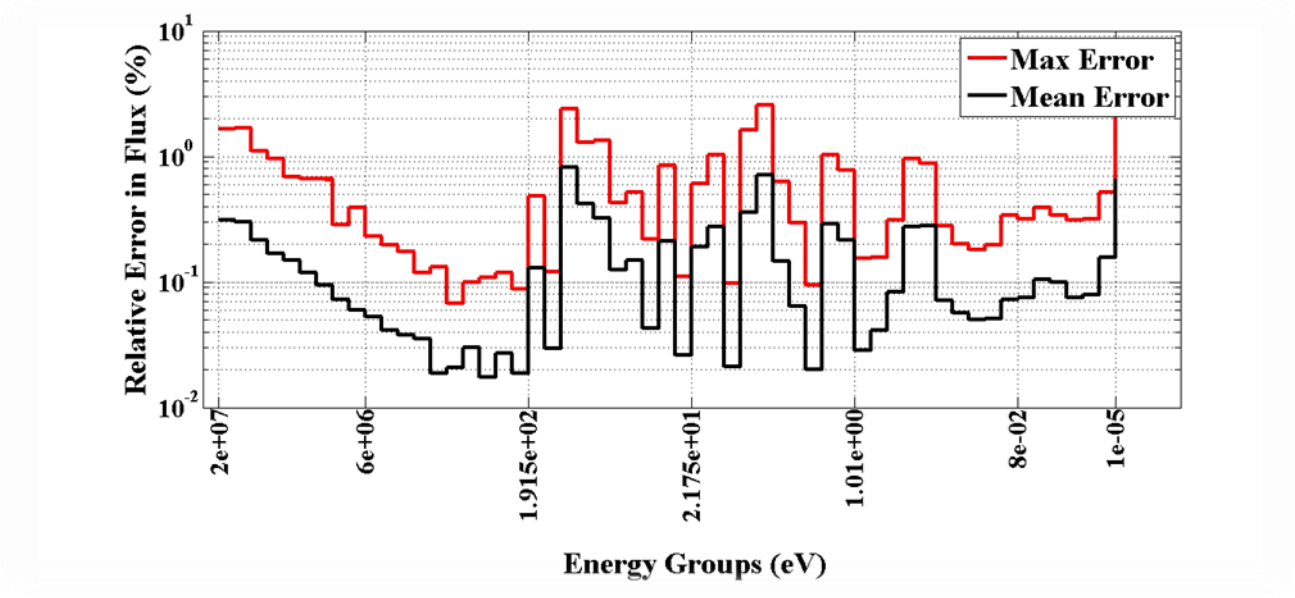

Fig. 5-38. Mixture 213 (20 GWd/MTU, Cold Conditions).

The previous figures show that the maximum error in flux again did not exceed 3% and that the mean error is still below 0.7% which reflects that the extracted subspace is a good representative for the full assembly.

www.manaraa.com

5.4 Conclusions

This work has equipped our previously developed ROM techniques with probabilistic error metrics that bound the maximum errors resulting from the reduction. This is a mandatory feature for any ROM to ensure the reliability of the reduced model for subsequent engineering analyses, such as uncertainty and sensitivity analysis and credibly defend the predictions of the reduced model. Picking the appropriate algorithm for each interface, e.g., parameters, state, and responses, one can effectively aggregate the associated errors to estimate an error bound on the response of interest. This functionality will prove essential in multi-physics frameworks where the active subspace generated by one physics model is used as the basis for reducing the input space for another physics model.

The estimation of error bounds requires sampling of the actual error using a user-defined PDF. Several oversamples are drawn from such PDF to calculate the corresponding errors of the ROM model with the maximum of these errors multiplied by a scalar to establish an upper-bound on the ROM error. Numerical investigations have shown that the scalar multiplier could lead to an unnecessarily conservative bound, and have identified the reason for that being the use of Gaussian PDF to select the oversamples. This work has numerically illustrated that the use of a binomial distribution results in a more realistic bound, i.e., one that is closer to the actual reduction errors.

More importantly, this work has shown a practical way by which the ROM errors can be evaluated for general reduction operators. This is invaluable when dealing with high fidelity codes that can only be executed few times, and it is difficult to extract their active subspaces.

www.manaraa.com

This work proposes a new idea to construct the active subspace for a computationally expensive model. The basic idea is to employ the physics in a sub-domain, akin to lattice physics calculations and let the reduction theory determine the error bounds resulting from this application to other pin cell models. Results indicate that the idea is sound for the lattice model employed representing a BWR reactor. It is important to point out that while the idea here is akin to standard homogenization theory (at least in spirit since no actual homogenization is applied), the capability to calculate error bounds on the active subspace is present, which is not possible with existing homogenization theory techniques. This approach could help realize the potential of employing high fidelity simulation codes in a practical manner that can benefit the end-users.

www.manaraa.com

REFERENCES

[1] Witten, Ian H., and Eibe Frank. *Data Mining: Practical machine learning tools and techniques*. Morgan Kaufmann, 2005.

[2] Antoulas, A.C., Sorensen, D.C. and Gugercin, S., "A survey of model reduction methods for large-scale systems", Structured Matrices in Operator Theory, Numerical Analysis, Control, Signal and Image Processing, Contemporary Mathematics, AMS publications, 280, (2001);pp. 193-219.

[3] Isukapalli, S. S., A. Roy, and P. G. Georgopoulos. "Stochastic response surface methods (SRSMs) for uncertainty propagation: application to environmental and biological systems." *Risk analysis* **18**.3 (1998): 351-363.

[4] Kennedy, Marc C., and Anthony O'Hagan. "Bayesian calibration of computer models." *Journal of the Royal Statistical Society: Series B (Statistical Methodology)* **63**.3 (2001): 425-464.

[5] Doebling, Scott W., et al. "A Metamodel-based Approach to Model Validation for Nonlinear Finite Element Simulations,# 72." *PROCEEDINGS-SPIE THE INTERNATIONAL SOCIETY FOR OPTICAL ENGINEERING*. Vol. **1**. International Society for Optical Engineering; 1999, 2002.

[6] Doebling, Scott W. "Structural dynamics model validation: pushing the envelope." *Proceedings of the International Conference on Structural Dynamics Modelling—Test, Analysis, Correlation, and Validation*. 2002.

www.manaraa.com

[7] Eldred, M. S., et al. "Second-order corrections for surrogate-based optimization with model hierarchies." *Proceedings of the 10th AIAA/ISSMO Multidisciplinary Analysis and Optimization Conference, Albany, NY, Aug.* 2004.

[8] Chen, Wei, Ruichen Jin, and Agus Sudjianto. "Analytical global sensitivity analysis and uncertainty propagation for robust design." *Journal of quality technology* **38**.4 (2006): 333-348.

[9] Liem, Rhea Patricia. *Surrogate modeling for large-scale black-box systems*. Diss. Massachusetts Institute of Technology, 2007.

[10] Bliznyuk, Nikolay. *Posterior approximation by interpolation for Bayesian inference in computationally expensive statistical models*. Diss. Cornell University, 2008.

[11] Roston, G., et al. "Studies on neutron noise diagnostics of control rod vibrations by neural networks." (1996).

[12] Tsoukalas, Lefteri H., and Robert E. Uhrig. *Fuzzy and neural approaches in engineering.* John Wiley & Sons, Inc., 1996.

[13] Hines, J. W., and Robert E. Uhrig. "Trends in computational intelligence in nuclear engineering." *Progress in nuclear energy* **46**.3 (2005): 167-175.

[14] Fouet, Fabrice, and Pierre Probst. "Sensitivity Analysis by the Use of a Surrogate Model During Large Break LOCA on ZION Nuclear Power Plant With CATHARE-2 V2. 5 Code." *17th International Conference on Nuclear Engineering. American Society of Mechanical Engineers*, 2009.

[15] Guo, Yun, Cheng Gong, and He-Yi Zeng. "The application of Artificial Neural Network in nuclear energy." *Proceedings of the Ninth International Conference on Machine Learning and Cybernetics (ICMLC).* Vol. **3**. IEEE, 2010.

www.manaraa.com

[16] Khalafi, Farshad Faghihi H., and S. M. Mirvakili. "A Literature Survey of Neutronics and Thermal-Hydraulics Codes for Investigating Reactor Core Parameters; Artificial Neural Networks as the VVER-1000 Core Predictor." *NUCLEAR POWER-SYSTEM SIMULATIONS AND OPERATION* (2011): 103.

[17] Uhrig, Robert E., and J. Hines. "Computational intelligence in nuclear engineering." *Nuclear Engineering and Technology* **37**.2 (2005): 127-138.

[18] Lockwood, Brian, and Mihai Anitescu. "Gradient-enhanced universal kriging for uncertainty propagation in nuclear engineering." *Transactions of the American Nuclear Society* **104** (2011): 347.

[19] Yankov, Artem. *Analysis of Reactor Simulations Using Surrogate Models*. Diss. University of Michigan, 2015.

[20] Williams, M. M. R. "Polynomial chaos functions and neutron diffusion." *Nuclear science and engineering* **155**.1 (2007): 109-118.

[21] Fichtl, Erin D., and Anil K. Prinja. "The stochastic collocation method for radiation transport in random media." *Journal of Quantitative Spectroscopy and Radiative Transfer* **112**.4 (2011): 646-659.

[22] Ayres, D., M. M. R. Williams, and M. D. Eaton. "Time and static eigenvalues of the stochastic transport equation by the methods of polynomial chaos." *Progress in Nuclear Energy* **67** (2013): 33-55.

[23] Wang, Congjian, Hany S. Abdel-Khalik, "Exact-To-Precision Generalized Perturbation Theory For Eigen Value Problems," *Nuclear Engineering and Design*, **256**, pp. 130-140, (2013).

www.manaraa.com

[24] Mickus, Ignas, et al. "An approach to physics based surrogate model development for application with IDPSA." Probabilistic Safety Assessment and Management PSAM 12, June 2014, Honolulu, Hawaii. 2014.

[25] Van Der Maaten, Laurens, Eric Postma, and Jaap Van den Herik. "Dimensionality reduction: a comparative." *J Mach Learn Res* **10** (2009): 66-71.

[26] Fodor, Imola K. "A survey of dimension reduction techniques." (2002).

[27] Blum, Michael GB, et al. "A comparative review of dimension reduction methods in approximate Bayesian computation." *Statistical Science* **28**.2 (2013): 189-208.

[28] Bartenhagen, Christoph, et al. "Comparative study of unsupervised dimension reduction techniques for the visualization of microarray gene expression data." *BMC bioinformatics* **11**.1 (2010): 567.

[29] Pearson, Karl. "Principal components analysis." *The London, Edinburgh, and Dublin Philosophical Magazine and Journal of Science* **6**.2 (1901): 559.

[30] Hotelling, Harold. "Analysis of a complex of statistical variables into principal components." *Journal of educational psychology* **24**.6 (1933): 417.

[31] Fisher, Ronald A. "The use of multiple measurements in taxonomic problems." *Annals of eugenics* **7**.2 (1936): 179-188.

[32] Roweis, Sam T., and Lawrence K. Saul. "Nonlinear dimensionality reduction by locally linear embedding." *Science* **290**.5500 (2000): 2323-2326.

[33] Belkin, Mikhail, and Partha Niyogi. "Laplacian Eigenmaps and Spectral Techniques for Embedding and Clustering." *NIPS*. Vol. **14**. 2001.

www.manaraa.com

[34] Donoho, David L., and Carrie Grimes. "Hessian Eigenmaps: Locally linear embedding techniques for high-dimensional data." *Proceedings of the National Academy of Sciences* **100**.10 (2003): 5591-5596.

[35] Kruskal, Joseph B., and Myron Wish. *Multidimensional scaling.* Vol. **11**. Sage, 1978.

[36] Tenenbaum, Joshua B., Vin De Silva, and John C. Langford. "A global geometric framework for nonlinear dimensionality reduction." *science* **290**.5500 (2000): 2319-2323.

[37] Schölkopf, Bernhard, Alexander Smola, and Klaus-Robert Müller. "Kernel principal component analysis." *Artificial Neural Networks—ICANN'97*. Springer Berlin Heidelberg, 1997. 583-588.

[38] Coifman, Ronald R., and Stéphane Lafon. "Diffusion maps." *Applied and computational harmonic analysis* **21**.1 (2006): 5-30.

[39] Hand, David J., and D. J. Hand. *Kernel discriminant analysis*. New York: Research studies press, 1982.

[40] Baudat, Gaston, and Fatiha Anouar. "Generalized discriminant analysis using a kernel approach." *Neural computation* **12**.10 (2000): 2385-2404.

[41] Raymer, Michael L., et al. "Dimensionality reduction using genetic algorithms." *Evolutionary Computation, IEEE Transactions on* **4**.2 (2000): 164-171.

[42] Hinton, Geoffrey E., and Sam T. Roweis. "Stochastic neighbor embedding." *Advances in neural information processing systems.* 2002.

[43] Teh, Yee W., and Sam T. Roweis. "Automatic alignment of local representations." *Advances in neural information processing systems*. 2002.

[44] Harmeling, Stefan. "Exploring model selection techniques for nonlinear dimensionality reduction." *University of Edinburgh, Tech. Rep. EDI-INF-RR*-0960 (2007).

www.manaraa.com

[45] Kruger, Uwe, Junping Zhang, and Lei Xie. "Developments and applications of nonlinear principal component analysis–a review." *Principal manifolds for data visualization and dimension reduction*. Springer Berlin Heidelberg, 2008. 1-43.

[46] Yin, Hujun. "Learning nonlinear principal manifolds by self-organising maps." *Principal manifolds for data visualization and dimension reduction*. Springer Berlin Heidelberg, 2008. 68-95.

[47] Lawrence, Neil. "Probabilistic non-linear principal component analysis with Gaussian process latent variable models." *The Journal of Machine Learning Research* **6** (2005): 1783-1816.

[48] Wittman, Todd. "MANIfold learning Matlab demo." URL: http://www. math. umn. edu/~ wittman/mani/index. html (2005).

[49] SCALE: A Comprehensive Modeling and Simulation Suit for Safety Analysis and Design, ORNL/TM- 2005/39, Versions 6.1and 6.2, Oak Ridge National Laboratory, Oak Ridge, Tennessee, 2011.

[50] POSEIDON: Package for Orthonormal Subspace Extraction and Identification of Nuclear Engineering, Youngsuk Bang and Hany S. Abdel-Khalik, Version 1.1, North Carolina State University, 2013.

[51] Wang, Congjian, Hany S. Abdel-Khalik, and Uger Mertyurek,. "CRANE: A New Scale Super-Sequence for Neutron Transport Calculations." *Proceeding of MC 2015, Nashville, TN, April 19–23*. 2015.

[52] Abdel-Khalik, H. S., *Adaptive core simulation*, Ph.D. dissertation, North Carolina State University, 2004.

www.manaraa.com

[53] Le Maître, Olivier P., and Omar M. Knio. *Introduction: Uncertainty Quantification and Propagation*. Springer Netherlands, 2010.

[54] Russi, T. M., Uncertainty quantification with experimental data and complex system models." Ph.D. dissertation, UC Berkeley, 2010.

[55] Smith, Ralph C. *Uncertainty quantification: theory, implementation, and applications*. Vol. 12. SIAM, 2013.

[56] Constantine, Paul G., and Qiqi Wang. "Input subspace detection for dimension reduction in high-dimensional approximation." *arXiv preprint arXiv*:**1202**.3508 (2012).

[57] Stoyanov, Miroslav, and Clayton G. Webster. "A gradient-based sampling approach for dimension reduction of partial differential equations with stochastic coefficients." *International Journal for Uncertainty Quantification* **5**.1 (2015).

[58] Abdel-Khalik, Hany S., Ralph A. Nelson, and Brian M. Adams. "Hybrid uncertainty and sensitivity algorithms for high dimensional nonlinear models, part I: Introduction to the theory." Transactions of the American Nuclear Society 103 (2010): 375-377.

[59] Saltelli, Andrea, Karen Chan, and E. Marian Scott, eds. *Sensitivity analysis*. Vol. **1**. New York: Wiley, 2000.

[60] Cacuci, Dan G., Mihaela Ionescu-Bujor, and Ionel Michael Navon. *Sensitivity and uncertainty analysis, volume II: applications to large-scale systems*. Vol. **2**. CRC press, 2005.

[61] Saltelli, Andrea, et al. *Global sensitivity analysis: the primer*. John Wiley & Sons, 2008.

[62] Homma, Toshimitsu, and Andrea Saltelli. "Importance measures in global sensitivity analysis of nonlinear models." *Reliability Engineering & System Safety* **52**.1 (1996): 1-17.

www.manaraa.com

[63] Doubilet, Peter, et al. "Probabilistic sensitivity analysis using Monte Carlo simulation. A practical approach." *Medical decision making: an international journal of the Society for Medical Decision Making* **5**.2 (1984): 157-177.

[64] Hamby, D. M. "A review of techniques for parameter sensitivity analysis of environmental models." *Environmental monitoring and assessment* **32**.2 (1994): 135-154.

[65] Dorigo, W. A., et al. "A review on reflective remote sensing and data assimilation techniques for enhanced agroecosystem modeling." *International journal of applied earth observation and geoinformation* **9**.2 (2007): 165-193.

[66] Grell, Georg A., and Dezső Dévényi. "A generalized approach to parameterizing convection combining ensemble and data assimilation techniques." *Geophysical Research Letters* **29**.14 (2002).

[67] Houtekamer, Peter L., and Herschel L. Mitchell. "Data assimilation using an ensemble Kalman filter technique." *Monthly Weather Review* **126**.3 (1998): 796-811.

[68] Miller, Robert N., Michael Ghil, and Francois Gauthiez. "Advanced data assimilation in strongly nonlinear dynamical systems." *Journal of the atmospheric sciences* **51**.8 (1994): 1037-1056.

[69] Eleveld, Harry, Yvo S. Kok, and Chris JW Twenhofel. "Data assimilation, sensitivity and uncertainty analyses in the Dutch nuclear emergency management system: a pilot study." *International Journal of Emergency Management* **4**.3 (2007): 551-563.

[70] Athe, Paridhi, Ugur Mertyurek, and Hany S. Abdel-Khalik. "Determination of bias, bias uncertainty, and coverage using data assimilation." *American Nuclear Society*. 2014.

[71] Huang, Dongli, Hany S. Abdel-Khalik. "Reducibility of the INL's MAMMOTH coupled code system for Reactor Analysis. " *Submitted to PHYSOR, Sun Valley, Idaho 2016.*

www.manaraa.com

[72] Oja, Erkki. *Subspace methods of pattern recognition*. Vol. 6. Research Studies Press, 1983.

[73] Bang, Youngsuk, Jason Hite, And Hany S. Abdel-Khalik, "Hybrid reduced order modeling applied to nonlinear models," *IJNME*; **91**(2012): pp.929–949.

[74] Wikipedia Contributers. "Intrinsic Dimension." *Wikipedia, The Free Encyclopedia*, 28 Mar,2016.Web:<https://en.wikipedia.org/w/index.php?title=Intrinsic_dimension&oldid=712399481>.

[75] Dixon, John D. "Estimating extremal eigenvalues and condition numbers of matrices." *SIAM Journal on Numerical Analysis* **20**.4 (1983): 812-814.

[76] Wilks, S. "Mathematical statistics. A Wiley Publication in Mathematical Statistics." *John Wiley & Sons Inc., New York* **1**.2 (1962): 1971.

[77] Braconnier, T., et al. "Towards an adaptive POD/SVD surrogate model for aeronautic design." *Computers & Fluids* **40**.1 (2011): 195-209.

[78] Du, Juan, et al. "POD reduced-order unstructured mesh modeling applied to 2D and 3D fluid flow." *Computers & Mathematics with Applications* **65**.3 (2013): 362-379.

[79] Luchtenburg, D. M., B. R. Noack, and M. Schlegel. "An introduction to the POD Galerkin method for fluid flows with analytical examples and MATLAB source codes." Berlin Institute of Technology MB1, Muller-Breslau-Strabe **11** (2009).

[80] Volkwein, Stefan. "Model reduction using proper orthogonal decomposition." Lecture Notes, Institute of Mathematics and Scientific Computing, University of Graz. see http://www. uni-graz. at/imawww/volkwein/POD. pdf (2011).

www.manaraa.com

[81] Georgiou, Ioannis T., and Ira B. Schwartz. "Dynamics of large-scale coupled structural/mechanical systems: A singular perturbation/proper orthogonal decomposition approach." *SIAM Journal on Applied Mathematics* **59**.4 (1999): 1178-1207.

[82] Liang, Y. C., et al. "Proper orthogonal decomposition and its applications–part II: Model reduction for MEMS dynamical analysis." *Journal of Sound and Vibration* **256**.3 (2002): 515-532.

[83] Rapún, María-Luisa, and José M. Vega. "Reduced order models based on local POD plus Galerkin projection." *Journal of Computational Physics* **229**.8 (2010): 3046-3063.

[84] Rathinam, Muruhan, and Linda R. Petzold. "A new look at proper orthogonal decomposition." *SIAM Journal on Numerical Analysis* **41**.5 (2003): 1893-1925.

[85] Volkwein, Stefan. "Proper orthogonal decomposition: Theory and reduced-order modelling." Lecture Notes, University of Konstanz 4 (2013): 4.

[86] Chapelle, Dominique, Asven Gariah, and Jacques Sainte-Marie. "Galerkin approximation with proper orthogonal decomposition: new error estimates and illustrative examples." *ESAIM: Mathematical Modelling and Numerical Analysis* **46**.04 (2012): 731-757.

[87] Bechtold, T., E. B. Rudnyi, and J. G. Korvink. "Error estimation for Arnoldi-based model order reduction of MEMS." *System* **10** (2004): 15.

[88] Amsallem, David, and Ulrich Hetmaniuk. "A posteriori error estimators for linear reduced-order models using Krylov-based integrators." *International Journal for Numerical Methods in Engineering* **102**.5 (2015): 1238-1261.

[89] Kuczynski, Jacek, and Henryk Wozniakowski. "Estimating the largest eigenvalue by the power and Lanczos algorithms with a random start." *SIAM journal on matrix analysis and applications* **13**.4 (1992): 1094-1122.

www.manaraa.com

[90] Kuczynski, J., and H. Wozniakowski. "Probabilistic bounds on the extremal eigenvalues and condition number by the Lanczos algorithm." *SIAM Journal on Matrix Analysis and Applications* **15**.2 (1994): 672-691.

[91] Gittens, Alex, and Joel A. Tropp. "Error bounds for random matrix approximation schemes." *arXiv preprint arXiv*:**0911**.4108 (2009).

[92] Halko, Nathan, et al. "An algorithm for the principal component analysis of large data sets." *SIAM Journal on Scientific computing* **33**.5 (2011): 2580-2594.

[93] Halko, Nathan, Per-Gunnar Martinsson, and Joel A. Tropp. "Finding structure with randomness: Probabilistic algorithms for constructing approximate matrix decompositions." *SIAM review* **53**.2 (2011): 217-288.

[94] Strang, Gilbert. *Introduction to linear algebra*. Vol. **3**. Wellesley, MA: Wellesley-Cambridge Press, 1993.

[95] Saad, Youcef. *Numerical methods for large eigenvalue problems*. Vol. 158. Manchester: Manchester University Press, 1992.

[96] Golub, Gene H., and Charles F. Van Loan. *Matrix computations.* Johns Hopkins studies in the mathematical sciences. (1996).

[97] Higham, Nicholas J. *Accuracy and stability of numerical algorithms*. Siam, 2002.

[98] Meyer, Carl D. *Matrix analysis and applied linear algebra*. Vol. **2**. Siam, 2000.

[99] Ipsen, Ilse CF. *Numerical matrix analysis: Linear systems and least squares*. Siam, 2009.

[100] KelleyC, T. "Iterative MethodsforLinearand Nonlinear Equations." *RaleighN. C.: NorthCarolinaStateUniversity* (1995).

[101] Sastry, Shankar, and Pravin Varaiya. "Coherency for interconnected power systems." *IEEE Transactions on Automatic Control* **26**.1 (1981): 218-226.

www.manaraa.com

[102] Holodnak, John T., Ilse C. F. Ipsen, and Ralph C. Smith. "Accuracy Of Response Surfaces Over Active Subspaces Computed With Random Sampling."

[103] Kenney, Charles S., and Alan J. Laub. "Small-sample statistical condition estimates for general matrix functions." *SIAM Journal on Scientific Computing* 15.1 (1994): 36-61.

[104] Gudmundsson, Thorkell, Charles S. Kenney, and Alan J. Laub. "Small-sample statistical estimates for matrix norms." *SIAM journal on matrix analysis and applications* 16.3 (1995): 776-792.

[105] Abdo, Mohammad G., Congjian Wang and Hany S. Abdel-Khalik, "Probabilistic Error Bounds for Reduced Order Modeling," *Proceedings of Int. Conf. of Math and Comp. ANS MC2015*, Nashville, TN April 19-23, 2015.

[106] Abdo, Mohammad G., Congjian Wang and Hany S. Abdel-Khalik, "Further Investigation of Error Bounds for Reduced Order Modeling," *Proceedings of Int. Conf. of Math and Comp. ANS MC2015*, Nashville, TN April 19-23, 2015.

[107] Abdo, Mohammad G., and Hany S. Abdel-Khalik. "Propagation of Error Bounds due to Active Subspace Reduction." *Transactions of American Nuclear Society, Summer* (2014).

[108] Abdo, Mohammad G., Hany S. Abdel-Khalik, "Development of Multi-Level Reduced Order Modeling Methodology," *ANS Annual Meeting*, **256**, pp. 130-140, San Antonio, TX, June 7-11, 2015.

[109] Abdo, Mohammad G., Hany S. Abdel-Khalik, "Further Investigation of Employing Binomial Small-Sample Estimator in M_LROM," *Submitted to ANS Annual Meeting*, New Orleans, LA, June 12-16, 2016.

[110] Abdo, Mohammad G., Hany S. Abdel-Khalik, "Efficient Active Subspace Identification via M_LROM," *Submitted to PHYSOR*, Sun Valley, Idaho, May 1-5, 2016.

www.manaraa.com

[111] Bedirhan Akdeniz, Kostadin N. Ivanov, "Boiling Water Reactor Turbine Trip (TT) Benchmark; Volume III: Summary Results of Exercise 2," NEA/NSC/DOC(2006)23.

[112] Abdo, Mohammad G., Hany S. Abdel-Khalik, "Assessment of the Validation Domain of Reduced Order Modeling," *ANS Winter meeting*, **113**, pp. 1212-1216, Washington, DC, November 8-12, 2015.

www.manaraa.com